In situ investigations of chemical reactions on ZnO-Pt model nanocatalysts for environmentally friendly energy generation sources

Hang Liu

Sorbonne Université

L'ECOLE DOCTORALE DE CHIMIE PHYSIQUE ET DE

CHIMIE ANALYTIQUE DE PARIS CENTRE (ED 388)

In Situ Investigations of Chemical Reactions on ZnO-Pt Model Nanocatalysts for Environmentally Friendly Energy Generation Sources

Par

HANG LIU

Thèse de doctorat

Présentée et soutenue publiquement le 29/06/2019

Devant un jury composé de :

M. Philippe Jonnard	Directreur de recherche	Sorbonne Université	(Président du jury)
M. Yanfeng Chen	Professeur	Nanjing University	(Rapporteur)
M. Xiaohua Ma	Professeur	Xidian University	(Rapporteur)
Mme. Lingyan Xu	Maître de conférences	Northwestern Polytechnical University	(Examinatrice)
M. François Rochet	Professeur	Sorbonne Université	(Directeur de thèse)
M. Wanqi Jie	Professeur	Northwestern Polytechnical University	(Co-directeur de thèse)
M. Ahmed Naitabdi	Maître de conférences	Sorbonne Université	(Co-encadrant, Examinateur)

Acknowledgements

First, I would like to thank Prof. Alain Dubois and my supervisor Prof. Wanqi Jie for providing me the opportunity to work in between the two laboratories, i.e. Laboratoire de Chimie Physique-Matière et Rayonnement in Sorbonne Université and the state key laboratory of solidification processing in Northwestern Polytechnical University.

Besides, I would like to thank my supervisor Prof. François Rochet for his insightful views, which incented me to widen my research during the three years. With his careful guidance, I overcame many difficulties of this project and learned a lot from him.

Also, I would like to thank my supervisor Prof. Ahmed Naitabdi for initiating and directing this project. I also appreciate his assistance, patient guidance and insightful views throughout this project. With his earnest instructions, I got over a lot of difficulties and made great progress in the process of the experiments.

Then I would like to thank all my colleagues in the lab (Alter Zakhtser, Anthony Boucly, Rabah Benbalagh, Régis Vacheresse and the others) for their help throughout these three years. Particularly, I give many thanks to Alter Zakhtser for his valuable contribution to this project and for sharing the happiness and sadness with me in these three years.

Finally, I would like to give many thanks to my parents, my father Tao Liu and my mother Yali Liu, who have been always supporting and understanding me unconditionally.

Special thanks to my girlfriend, Yuantao Liao, for standing by me during the ups and downs in these three years.

Paris, April 2019

Hang Liu

Abstract

The inverse ZnO/Pt(111) catalyst has been shown to exhibit remarkable catalytic performances in the low temperature CO oxidation and represent a promising stable catalytic system. The identification of the active sites in CO oxidation is important for a mechanistic understanding of the structure-reactivity relationship. To reveal their nature, the catalytic role of the ZnO thin films on Pt(111) in the low-temperature CO oxidation was studied by UHV scanning tunneling microscopy (STM), low-energy electron diffraction (LEED) and near ambient pressure X-ray photoemission (NAP-XPS) in operando conditions. We have first established a reproducible recipe to fabricate well-ordered ZnO thin films on Pt(111) using e-beam evaporation process, followed by the structural characterizations of the thin films as a function of film thickness by STM and LEED. The film grows in layer-by-layer mode along the (0001) orientation, starting from a graphene-like monolayer to reaching the ZnO(0001)-Zn terminated bulk surface. From the structural evolution of ZnO thin films after exposure to 1 mbar of the O_2: CO mixture (4:1), the special role of the ZnO/Pt boundaries was revealed. To shed more light on the role of the boundaries, a systematic comparative study of the ZnO/Pt(111) inverse catalyst with the plain Pt(111) surface was undertaken. The combined "embedded" mass spectroscopy and gas phase NAP-XPS analysis were relevant, first, to determine the regimes where mass transfer limitation starts to occur, allowing a sound discussion on the relation between steady-state molar fractions of reactants/product and surface reactivity, and, second, to calibrate the surface density of the adsorbates. Solid phase NAP-XPS spectra gave us access to the dynamics of the ZnO monolayer film covering only partially the Pt(111) single crystal surface. The pivotal, albeit unexpected role of ZnO-bound hydroxyls was clearly highlighted by the observation of the chemical signature of the CO+OH associative reaction products by XPS. The carboxyl formed at the low temperature (410 K) can be the intermediate species that leads to the evolution of CO_2, the OHs at the Pt/ZnO boundary being the co-catalyst, which explains the synergistic effect of ZnO and Pt, we and others have observed. However, the species formed at the higher temperature (from 445 K) is a formate, that would essentially be a spectator.

Abbreviations

HOR: hydrogen oxidation reaction

ORR: oxygen reduction reaction

NC-AFM: Noncontact atomic force microscopy

SXRD: surface x-ray diffraction

PLD: pulsed laser deposition

ML: monolayer

DFT: density functional theory

TMO: transition metal oxide

CUS: coordinatively unsaturated

MLE: monolayer equivalent

STM: scanning tunneling microscopy

UHV: ultrahigh vacuum

LEED: low energy electron diffraction

STS: scanning tunneling spectroscopy

XPS: X-ray photoelectron spectroscopy

NAP-XPS: near-ambient pressure X-ray photoelectron spectroscopy

LDOS: local density of states

HOMO: highest occupied molecular orbital

LUMO: lowest unoccupied molecular orbital

BE: binding energy

KE: kinetic energy

QMS: quadrupole mass spectrometer

Fcc: face-centered cubic

MTL: mass transfer limitation

IRAS: infrared reflective absorption spectroscopy

h-BN: hexagonal boron nitride

XRD: X-ray diffraction

FT-IR: fourier transform infrared spectrometer

UV-Vis: ultraviolet-visible spectrophotometer

THz: terahertz

THz-TDS: terahertz time-domain spectroscopy

Contents

Chapter 1: Introduction

1.1 Concerns of the environmental issues

The rapid development of the economy has brought about the increasing pace of the energy consumption throughout the world. For more than 30 years, the petroleum and coal have dominated most of the world energy consumption (Figure 1.1), which are satisfying the population's need. However, the resulting emission from the combustion of the fossil fuel has become the main cause of the air pollution, which leads to a negative impact on the environment and people [1].

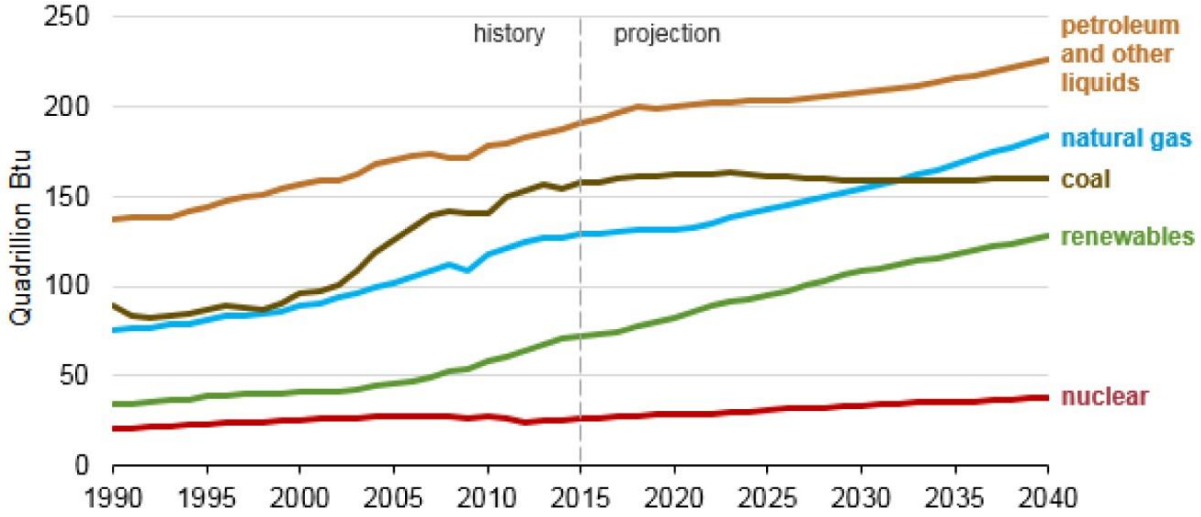

Figure 1.1: World energy consumption by energy source (1990-2040). Source: U.S. Energy Information Administration, International Energy Outlook 2017.

There are several key air pollutants arising from the combustion of the fossil fuels, such as sulfur oxides (SO_x), nitrogen oxides (NO_x), particulate matter (PM) and carbon monoxide (CO). These pollutants are mainly related to the human activity particularly due to transportations and household (Figure 1.2). These emissions are eventually causing the premature death of humans (e.g. heart disease and lung cancer), climate changes (warming and cooling effect) and acidification of water, etc. Nowadays due to the growing attention to air pollution, governments from all over the world are devoted to tackle this serious problem. Several regions in the world, such as Europe, and other major countries especially China are taking strong and leading actions not only in environmental remediation measures but also and most importantly in innovative solutions to provide energy with low environment impact. Based on more and more efforts and international collaborations, to 2040, the total global emission of

air pollutants will be controlled on a declining trend with applications of air-pollution control technologies and the transition to the cleaner energy [1].

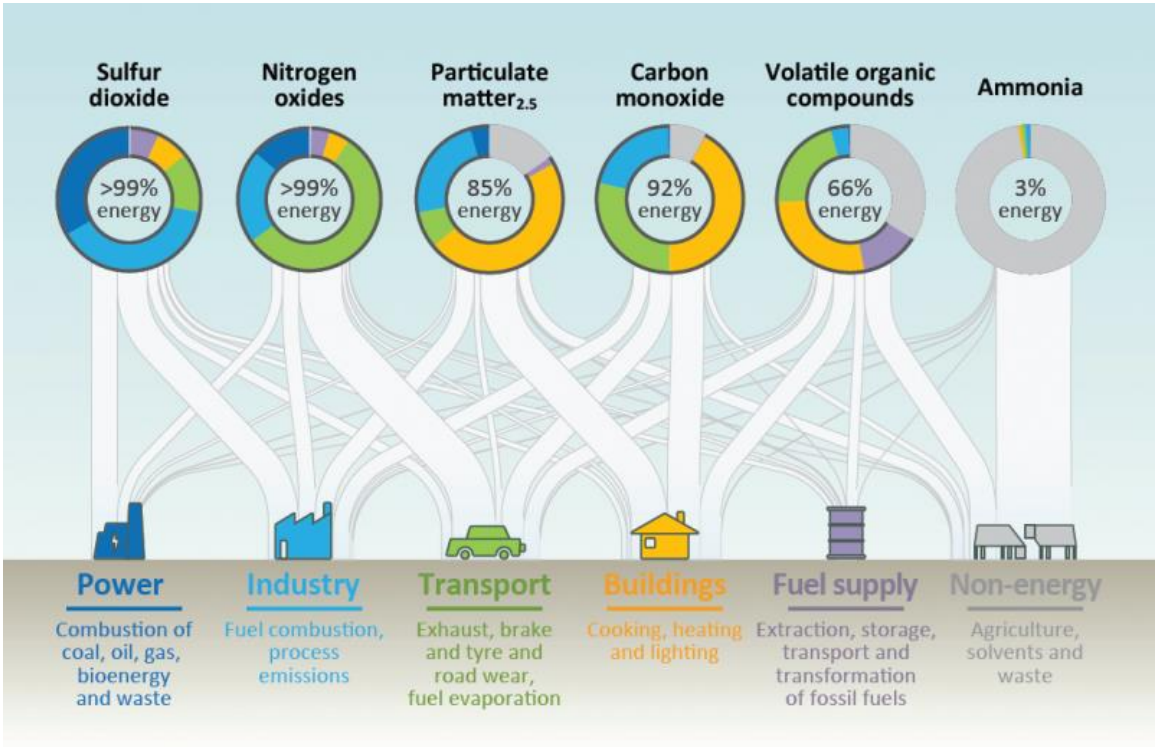

Figure 1.2: Primary air pollutants and their sources [1].

1.2 Hydrogen fuel cells

Hydrogen is an attractive synthetic fuel which can be used in fuel cells that are potential alternatives to the combustion and fossil fuel based energy generators They can be used especially for transportation and electricity generation [2] which are considered major energy sectors. Hydrogen fuel cell is a very promising technology which can convert hydrogen and oxygen efficiently into electricity at a relatively low operating temperature. There are a variety of different types of fuel cells which are classified either by the electrolyte employed or by the operating temperature [3]. Figure 1.3 gives an example of a fuel cell, which is the polymer electrolyte membrane fuel cell (PEMFC). PEMFC is a low-temperature fuel cell (the operating temperature 60-120 °C), in which the two electrodes are separated by a proton exchange membrane (an electrolyte) [3, 4]. The basic working principle can be described as three steps:

In the first step, hydrogen is introduced to the anode of the fuel cell and then hydrogen molecules split into hydrogen atoms;

In the second step, the hydrogen oxidation reaction (HOR) takes place with a catalyst lining the anode. Then the protons (H^+) can go through the polymer electrolyte membrane,

reaching the cathode. Meanwhile, the electrons travel through an external circuit to arrive at the cathode, creating a current. The HOR equation is expressed as:

$$H_2 \rightarrow 2H^+ + 2e^- \quad (1)$$

In the third step, oxygen at the cathode reacts with the protons and electrons from the anode, forming water as the only side product. This reaction is the oxygen reduction reaction (ORR), which is described as:

$$\frac{1}{2}O_2 + 2H^+ + 2e^- \rightarrow H_2O \quad (2)$$

Hence, the overall reaction of PEMFC can be written as:

$$H_2 + \frac{1}{2}O_2 \rightarrow H_2O\ (l);\ \Delta H = -286\ kJ/mol \quad (3)$$

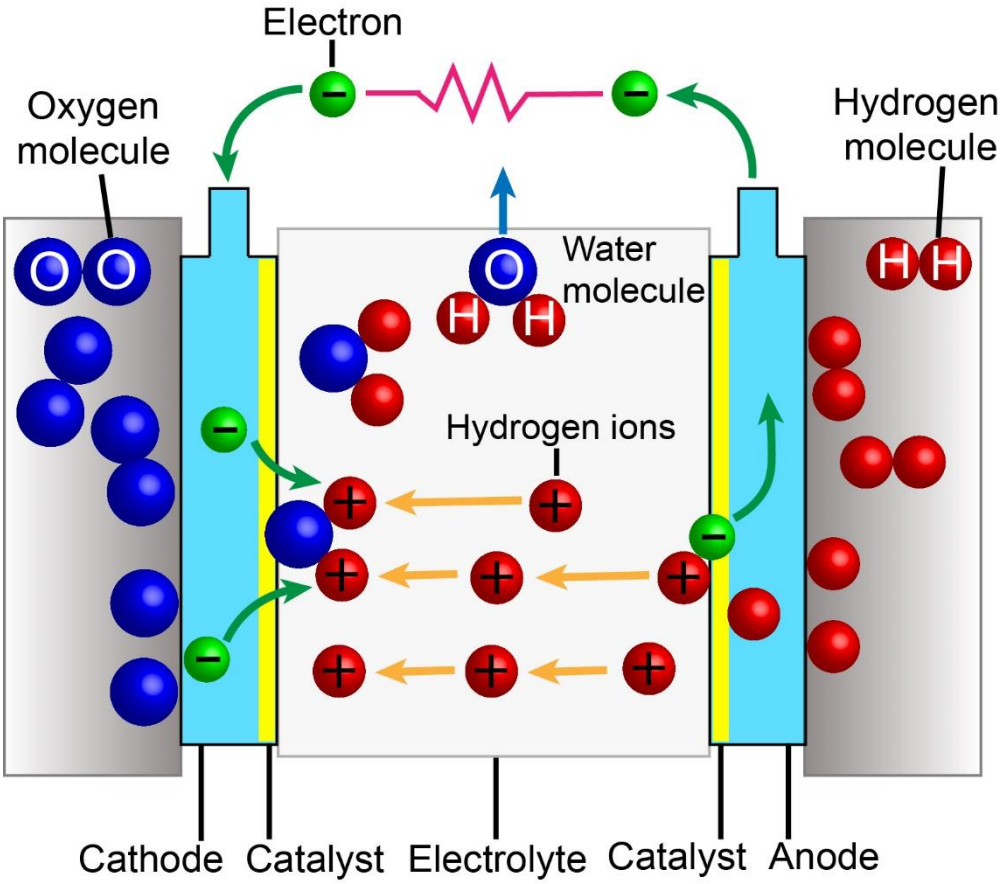

Figure 1.3: Schematic of a hydrogen fuel cell.

1.3 Inverse oxide/metal catalysts

The fundamental science and industrial technologies such as the energy conversion and the pollution control emphasize the crucial role of Pt-based materials as one of the prominent catalysts [3, 5, 6]. In fact, platinum, one of the most important transition metals, is widely used

in heterogeneous catalysis due to its high activity and selectivity for many chemical reactions [7-9], such as CO oxidation [10] and CO_2 hydrogenation [11]. Nevertheless, Pt mainly suffers from two severe issues, which are CO poisoning resulting in a rapid deactivation and material dissolution, respectively [12, 13]. CO strongly adsorbs on the Pt surface, which blocks the active sites and deactivates the catalytic reaction on the surface. For instance, in a hydrogen fuel cell, CO, which is the contamination in H_2 gas, adsorbs on Pt catalysts and tremendously decreases the kinetics of the HOR and ORR at anode and cathode [3]. Figure 1.4(a) shows that CO molecules were observed as the dark protrusions on the Pt(111) surface at room temperature in a base pressure of 10^{-10} mbar. The strong adsorption of CO on the Pt surface is generally described by the Bolyholder model (Figure1.4(b)) [14], in which electrons are donated from CO via a σ bond to the d-band of Pt and meanwhile electron back-donation process takes place via transferring electrons from Pt to the $2\pi^*$ orbital of CO.

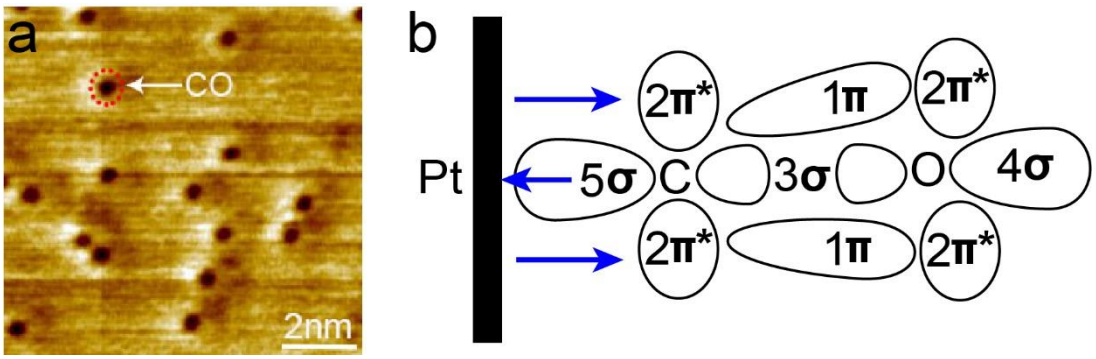

Figure 1.4: (a) Our STM image of Pt(111) surface (tunneling condition: 0.2 V, 500 pA); (b) Schematic of the Bolyholder model.

On the other hand, Pt is a scarce and expensive metal as shown in Figure 1.5, which limits the widespread practical applications in industry. Recently, new research efforts have been emerging in order to address the limitations (CO poisoning, material dissolution and high price of Pt) and produce catalysts with enhanced stability [15, 16]. In particular, the transition metal-oxide nanocatalysts are of paramount interest in the development of efficient catalytic materials, which provides a suitable method to partially replace Pt by a more abundant transition metal [16-18]. Thus the decrease of Pt-load in the catalysts is currently attracting large attention as a suitable method to decrease the high cost of catalysts. Indeed, recently, Zn has emerged as one of the most promising elements in bimetallic catalysts owing in part to the stability of its oxide (ZnO) under reducing conditions [16, 18-20] and its greater affinity with oxygen compared with that of Pt. Elligham diagrams show Zn is thermodynamically able to reduce PtO_2 to Pt, forming ZnO. Hence, Zn, an affordable metallic material (see Figure 1.5), could

offer a good opportunity to form an efficient catalyst when it combines with Pt. Indeed, ZnO/Pt is active for CO oxidation [19] and promotes catalytic reactions related to fuel cells [20, 21].

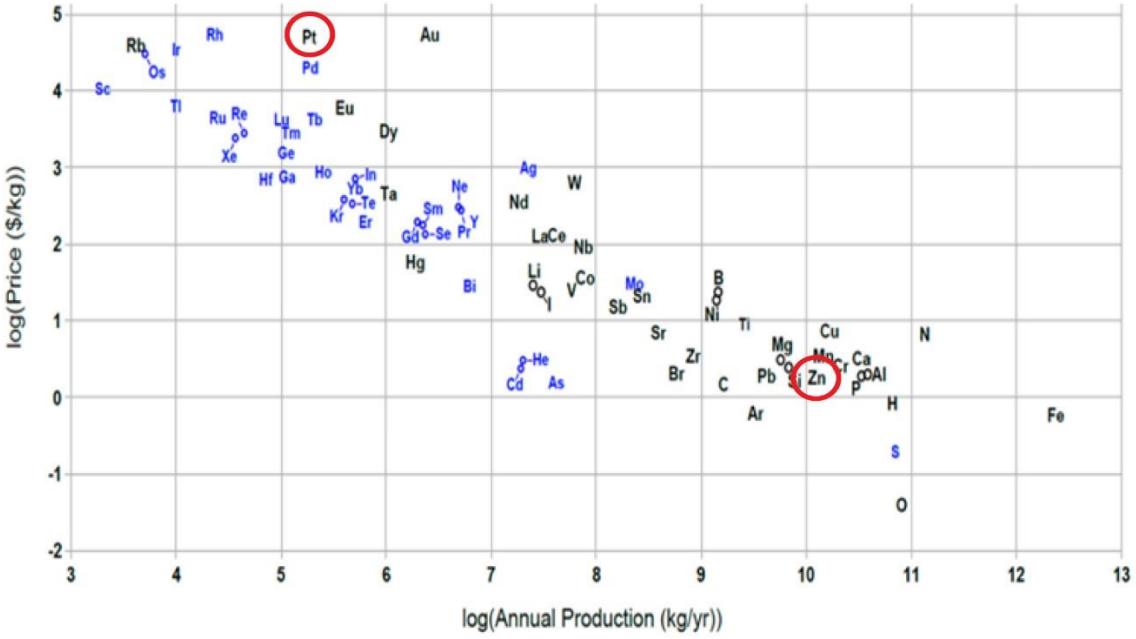

Figure1.5: Price of the elements ($/kg) versus their annual production (kg/yr) [22].

The classic heterogenous catalysts consist of metal particles dispersed over an oxide support, which is called conventional metal/oxide catalysts (Figure 1.6) [23]. In this system, metal nanoparticles suffer premature deactivation and decomposition, due several effects: (i) the encapsulation of the metallic catalysts by the support, (ii) the decomposition and corrosion of the support under operating conditions [24]. Besides, the oxide support is either considered as a simple template for the metal dispersion or it can directly participate in the catalytic process [17]. However, in recent years there is a motivation to improve the configuration of the conventional catalyst by taking advantage of the intrinsic properties of metal oxide. Indeed, oxide nanoparticles has presented special physical and chemical properties due to their size, a high density of defects and corner or edge sites on their surface [25]. The concept of the inverse oxide/metal catalyst was defined by Rodriguez and his coworkers [17, 26], which means nanoparticles of a metal-oxide are deposited on a metal surface (Figure 1.6). Another advantage of this system consists of the stability of metallic surfaces and the strong thermodynamic stability of thin film of metal-oxides. The study of inverse oxide/metal nanocatalysts offers great promises in the understanding of the role of oxide and oxide-metal interface in a catalytic process. Furthermore, the strong metal-oxide interaction of the inverse oxide-metal catalyst can have an effect on the electronic states of oxide nanoparticles, which produces new chemical properties [17]. In our work, the inverse ZnO/Pt(111) catalyst is studied to understand the

relationship between the chemical structure and the reactivity of ZnO nanostructures supported on Pt(111) single crystal relevant for CO oxidation reaction.

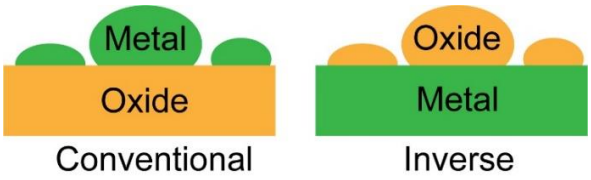

Figure1.6: Schematics of a conventional metal/oxide and an inverse oxide/metal catalyst.

1.4 Zinc oxide structures

Zinc oxide (ZnO) is an n-type semiconductor with a direct bandgap of ~3.3 eV at 300 K [27]. At the ambient pressure and room temperature, the thermodynamically stable structure of ZnO is wurtzite, (as shown in Figure 1.7 (a)), where each cation is surrounded by four anions at the corners of a tetrahedron, and vice versa [28]. The tetrahedral coordination typically represents sp^3 covalent bonding, however ZnO shows a relative strong ionic character. Therefore, ZnO, as a II-VI compound, shows the ionicity between an ionic behavior and a covalent behavior. ZnO has a hexagonal unit cell with two lattice parameters, $a = 3.2495$ Å and $c = 5.2069$ Å. In this type of structure, there are four common low-index surfaces: the non-polar $(10\bar{1}0)$ and $(11\bar{2}0)$ surfaces, and the polar (0001)-Zn and $(000\bar{1})$-O surfaces [29]. The polar surfaces are formed either by Zn or O ions, while the non-polar surfaces exhibit an equal number of Zn and O ions [30]. Apart from the wurtzite structure of ZnO, the zinc-blende structure can also be obtained by growth on the cubic substrate (as seen in Figure 1.7 (b)) [28], and the rocksalt structure is possibly stable at a relative high pressure (~10 GPa) (Figure 1.7 (c)) [31].

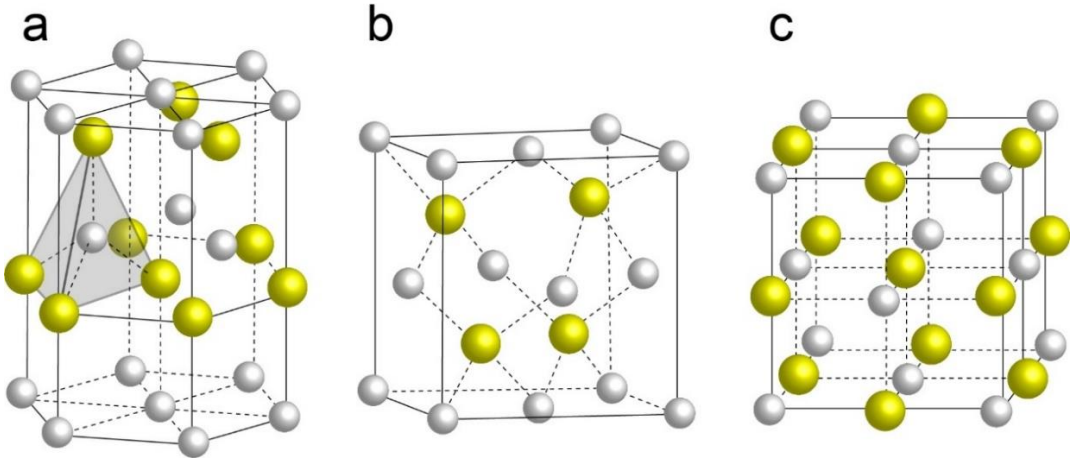

Figure1.7: Unit cells of ZnO crystals: (a) Wurtzite structure; (b) Zinc blende structure; (c) Rock salt structure. Zinc and oxygen atoms are yellow and white, respectively.

1.4.1 **Polar surface structures of the ZnO crystal**

Compared with the non-polar surfaces ($(10\bar{1}0)$ and $(11\bar{2}0)$), the polar surfaces of ZnO ((0001)-Zn and $(000\bar{1})$-O surfaces) are more interesting from the scientific and technological points of view [32]. The hexagonal wurtzite structure of ZnO is represented as alternating planes made up of fourfold-coordinated Zn^{2+} and O^{2-} ions along the c axis with alternating distances 1.99 Å and 0.69 Å, respectively [33]. Therefore, a (0001)-Zn terminated surface or a $(000\bar{1})$-O terminated surface is created by cutting the ZnO crystal perpendicular to the c axis. If these two ZnO polar surfaces are not compensated, the electrostatic potential increases due to the divergence of the net diploe moment when increasing the thickness of ZnO crystal [32-34], as shown in Figure 1.8. In order to reduce the electrostatic energy, three surface stabilization mechanisms are generally put forward [33]: (1) reduction of the charges of the Zn (O) surface by adsorption foreign molecules; (2) surface reconstruction by removal of surface atoms; (3) transfer of negative charge from the O plane to the Zn plane and creation of new surface states.

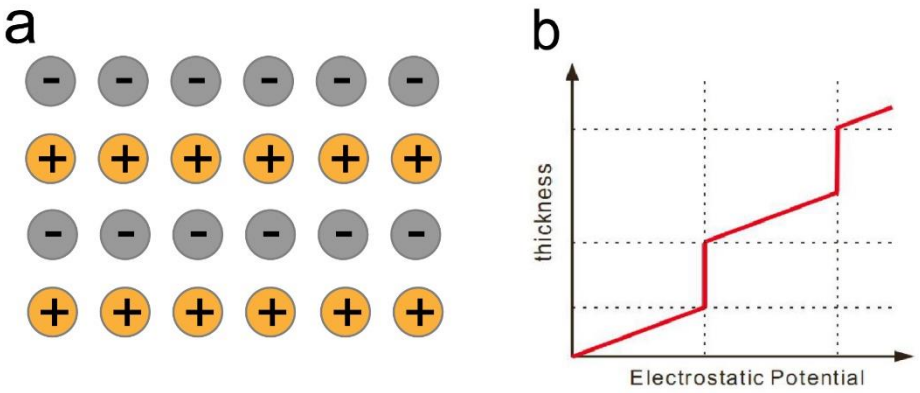

Figure1.8: Schematics of (a) the charged planes with the dipole moment normal to the surface and (b) the thickness versus the electrostatic potential [35].

The current work on (0001)-Zn terminated surface of the ZnO crystal by Dulub and coworkers [33, 36] shows that this polar surface is stabilized by the formation of triangular islands and pits, as shown in Figure 1.9 (a). Many triangular islands and pits are observed on the surface with a step height of ~ 2.7 Å, which corresponds to a single layer (half of the unit cell). Besides, the inner holes of the triangular islands are also found, whose orientation and shape depends on the size of the islands. Density functional theory (DFT) calculations (Figure 1.9 (b)-(d)) implies a 0.25 occupancy of Zn ions is deficient on the surface, and step edges of islands and holes are terminated by under-coordinated O atoms, which agrees with the

stabilization mechanism (2). In addition, this mechanism is suggested to be stable over a wide range of oxygen and chemical potentials [36].

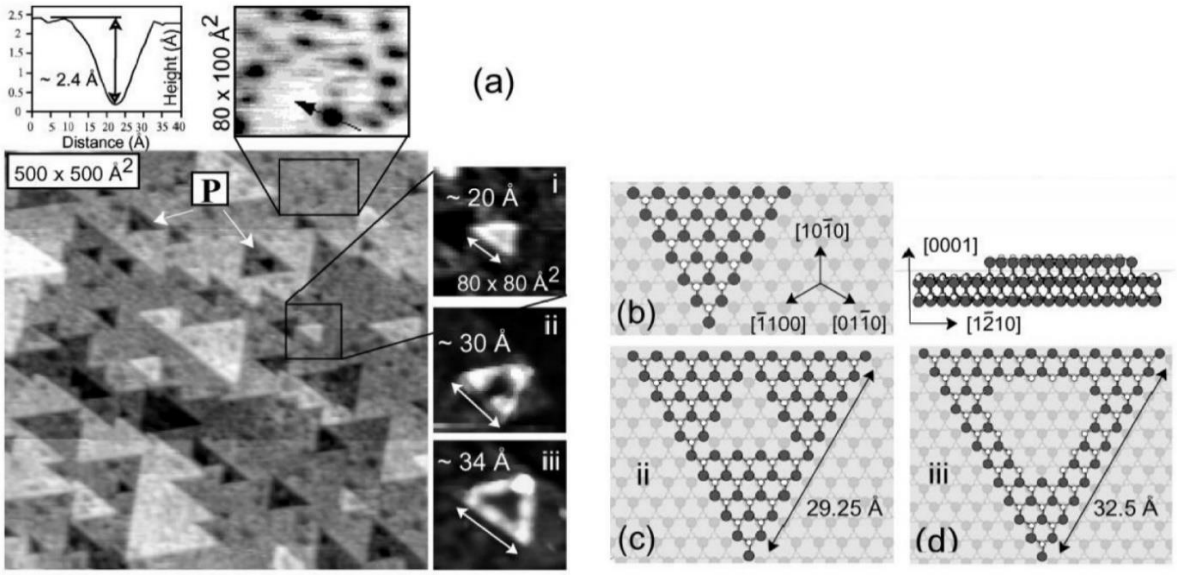

Figure1.9: (a) STM images of the (0001)-Zn terminated surface; (b)-(d) DFT calculated ZnO islands with different sizes [33].

The morphology of the $(000\bar{1})$-O terminated surface is different compared to that of the (0001)-Zn terminated surface, as shown in Figure 1.10 (a). The hexagonal terraces are observed with mainly a double step height of ~ 5.4 Å, which are typically terminated by step edges including an angle of 120˚ [30]. DFT calculations illustrate that the double-height step edges are stoichiometric, which consist of O-terminated $(\bar{1}010)$ and Zn-terminated $(00\bar{1}0)$ edges [30].

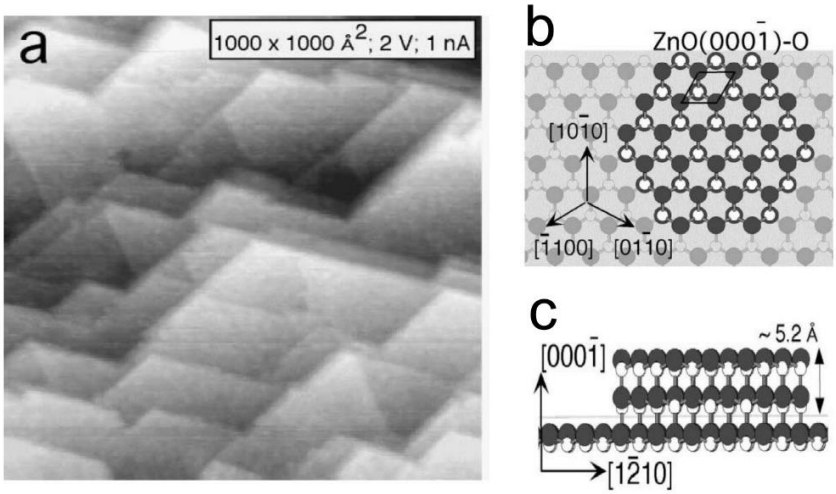

Figure1.10: (a) STM image of the $(000\bar{1})$-O terminated surface; (b) and (c) are the top-view and side-view models of hexagonal terraces, respectively [30].

Unlike the (0001)-Zn terminated surface which is stabilized by triangular islands and holes, the $(000\bar{1})$-O terminated surface is found to be stabilized by adding a half-monolayer hydrogen (H) which leads to the formation of terminal hydroxyls (OH) on the unreconstructed (1×1) ZnO surface at room temperature (shown in the noncontact atomic force microscopy (NC-AFM) image in Figure 1.11 (a)). This provides the stabilization mechanism of the surface (1) [37]. Moreover, the XPS measurement of the O 1s photoemission spectra confirms OH species on the surface, which has a shifted binding energy peak (at 532.3 eV) compared to the main peak (530.4 eV) which corresponds to the O 1s of the lattice, as shown in Figure 1.11 (b) [37]. In fact, the hydroxyls would disappear from the surface when heating the ZnO sample to 450 ℃ [37]. The H source of OH groups formed on the $(000\bar{1})$-O surface might come from the ambient environment (such as H_2O and H_2) and bulk H (interstitial H atoms present in bulk of the crystal) [29, 38], which cannot be ignored even under excellent UHV conditions. Residual water molecules are ubiquitous in the UHV. Moreover, DFT calculations corroborate that the hydrogenated surface is the most stable one over a wide range of pressures and temperatures [39].

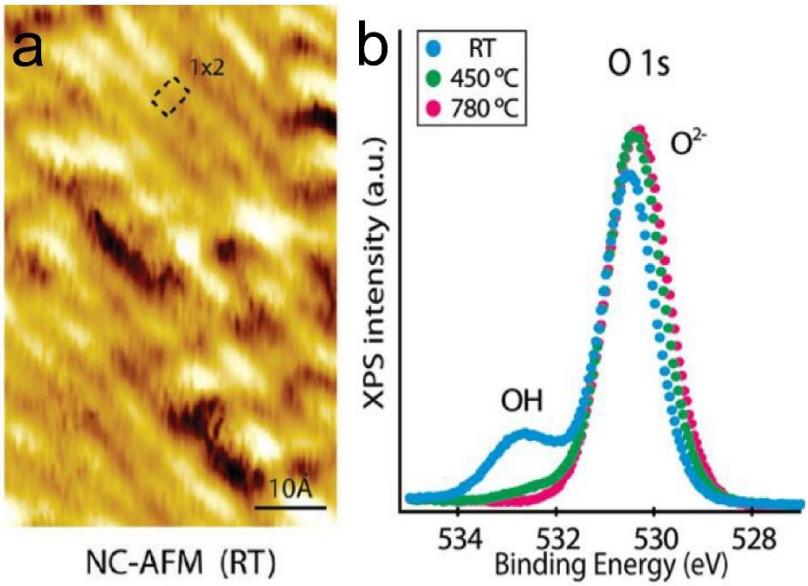

Figure1.11: (a) High-resolution, constant height NC-AFM image (50 × 80 Å, V_{CP} = 4.3 V, Δf_{set} = -111 Hz) of the H-covered surface ZnO $(000\bar{1})$ in the (1×2) H-covered state at room temperature; (b) O1s XPS spectra of the ZnO$(000\bar{1})$ surface. [37]

1.4.2 **Structures of ultrathin ZnO films**

For the ultrathin ZnO film with a thickness of only a few atomic layers, a new stabilization mechanism becomes effective, which is due to the stabilizing role of the support

and/or due to the ability of finite systems sustaining a nonzero polarization along the polar axis [34].

The first DFT calculations on the new phase of the ZnO film were reported by Claeyssens and coworkers [40, 41], who were investigating the deposition of thin ZnO films as templates for aligned growth of ZnO nanorods. When considering ZnO thin films (less than 18 layers) terminating with the polar (0001) and $(000\bar{1})$ surfaces, the energy of the flattened ZnO structure is much lower than that of the wurtzite ZnO structure. In this configuration, each Zn atom is bonded with three O atoms instead of four O atoms in the bulk, and vice versa, resulting in a co-planar structure composed of flat Zn_3O_3 hexagonal rings. In fact, this new ZnO structure is the same as the graphene or the hexagonal boron nitride (h-BN) structure. The transition between the wurtzite structure and graphene-like structure is shown in Figure 1.12.

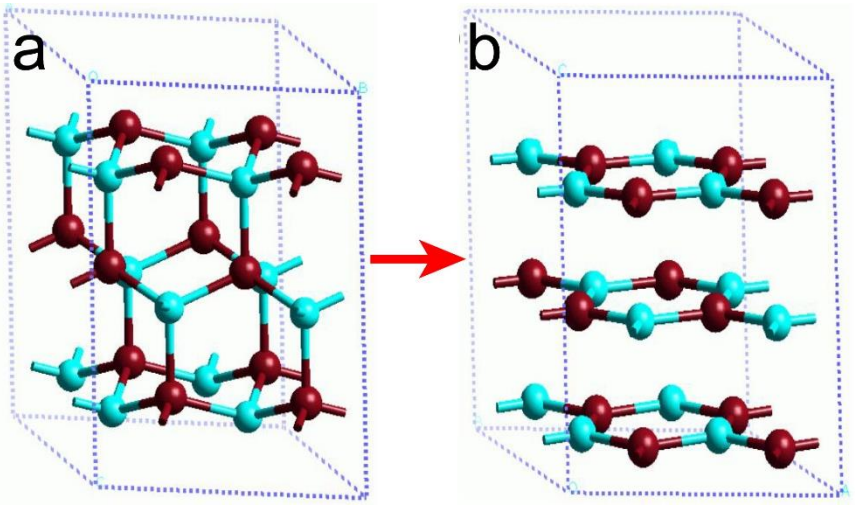

Figure1.12: (a) Model of the polar wurtzite structure of a ZnO film; (b) Model of a graphitic structure of a ZnO film. Zn atoms are in light blue and O atoms are in red. [40, 41]

Afterwards, the experimental existence of the h-BN ZnO structure was observed by Tusche and colleagues [42], who were studying ZnO films grown on Ag(111) using scanning tunneling microscopy (STM) and surface X-ray diffraction (SXRD). ZnO was fabricated by pulsed laser deposition (PLD) at 300K using a stoichiometric ZnO target in a 5×10^{-7} mbar of O_2, followed by annealing up to 680K. The coverage of the ZnO film was examined from 2.2 to 4.5 monolayers (ML) by STM measurements. Figure 1.13 (a) shows a STM image of a 2.2 ML ZnO film, which is characterized by an atomically flat ZnO double-layer decorated with some triangular islands on the third layer. Besides, the high resolution STM image of the 2.2 ML film, in Figure 1.13 (b), shows a distinct Moiré pattern corresponding to the coincidence lattice of 7 ZnO to 8 Ag(111) atoms, which is an indicator of the successful synthesis of the h-BN ZnO films on Ag(111). Back to Figure 1.13 (a), the inset shows the STM image of a 3.2

ML ZnO film on the same lateral scale as Figure 1.13 (a). Compared to the 2.2 ML ZnO film, the surface of the 3.2 ML ZnO film is rougher with incomplete layers forming small islands. The further SXRD illustrates the transition from the h-BN to the bulk wurtzite structure occurs around 3-4 ML coverage, which is connected to the surface roughness of the ZnO film, as shown in Figure 1.13 (c) and (d). Surprisingly, this transitional thickness to the bulk wurtzite is much smaller than the thickness calculated by Claeyssens and coworkers [40, 41], as mentioned above.

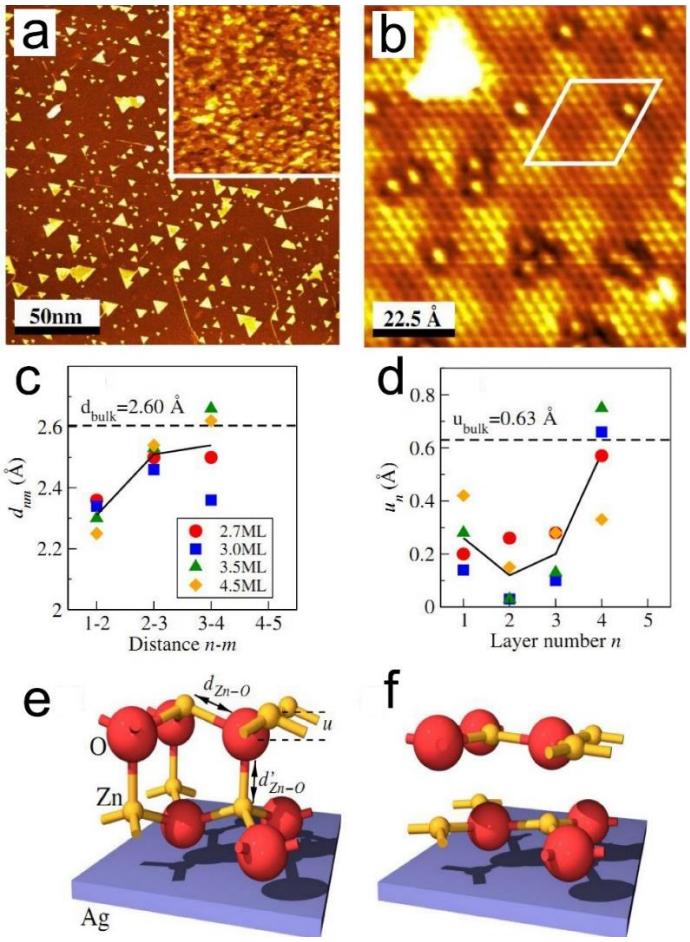

Figure1.13: (a) STM image of 2.2 ML ZnO on Ag(111). The inset is 3.2 ML on the same sale; (b) High resolution STM image of 2.2 ML film; (c) Distance (d_{nm}) between layer number n and m; (d) Oxygen coordinate (u_n) in layer number n; (e) Schematic of the bulk ZnO (wurtzite) structure; (f) Schematic of h-BN ZnO structure. [42]

An important study was reported by Deng and coworkers [43], who were using the reactive deposition of e-beam evaporated pure Zn under NO_2 at a pressure of 3×10^{-8} mbar at room temperature. The use of NO_2 instead of O_2 was mentioned because they discovered Zn was unable to fully oxidized with O_2 up to 2×10^{-6} mbar. The ZnO film on Au(111) presents two types of nanostructure, both of which display a Moiré pattern with a periodicity of ~ 23 Å

forming a ZnO(0001)-(7 ×7)/ Au(111)-(8 × 8) supercell. The two types of structures are defined by different heights, ~ 3.5 Å indicating single-layer ZnO and ~ 5.5 Å referring to bilayer ZnO, as seen in Figure 1.14 (e) and (f) (the STM height is not comparable to the physical height due to the electronic contributions involved in the STM measurements). Both the single and bilayer ZnO adopt a planar, graphene-like structure. When increasing the temperature from room temperature to 550K, the bilayer ZnO gradually becomes the dominant species on Au(111) instead of single-layer ZnO, as shown in Figure 1.14 (a-d). DFT calculations explain the interaction between ZnO layers are twice stronger than adhesion of ZnO with Au substrate, and therefore the bilayer is energetically favored with increasing the temperature.

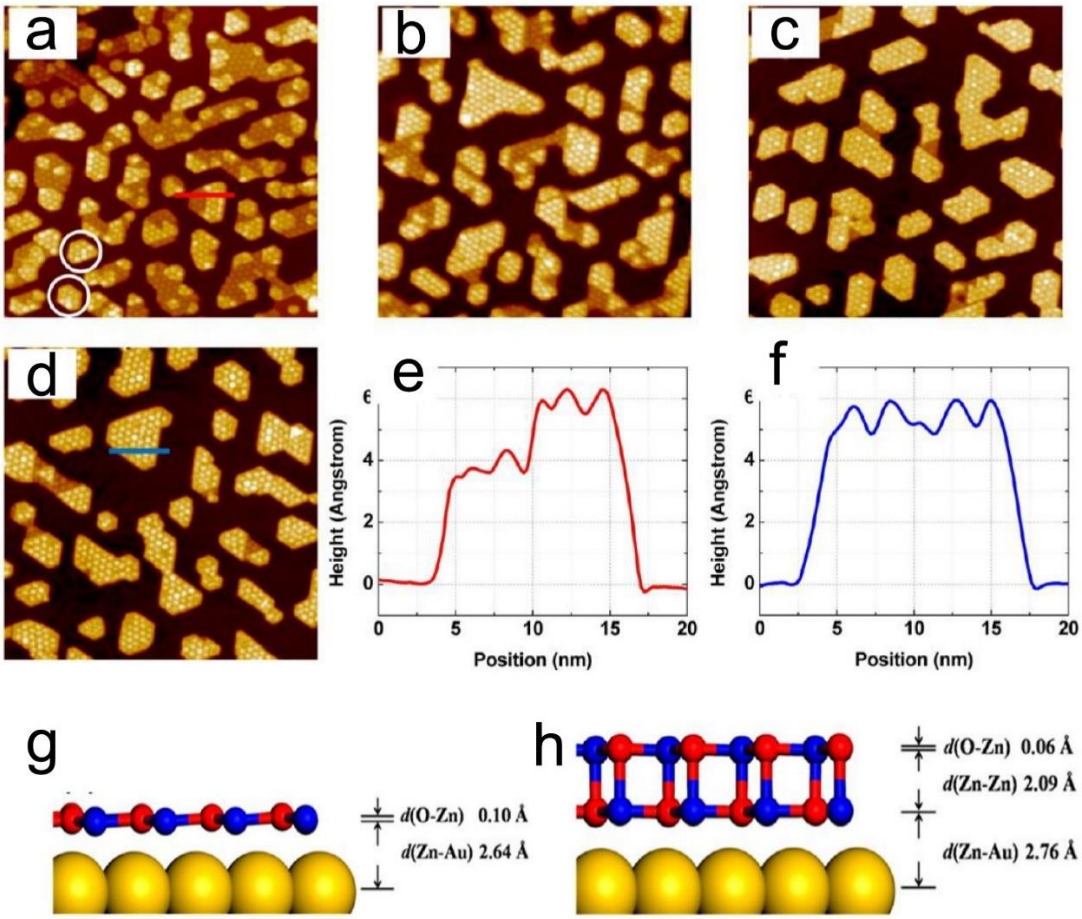

Figure 1.14: STM images (100 nm× 100 nm) of 0.9 ML ZnO on Au(111) using the reactive deposition followed by annealing at 550 K for (a) 5; (b) 30; (c) 60; and (d) 120 min; (e) and (f) are the Line scans specified in (a) and (d); (g) and (h) are the side views of the optimized structures of the single and bilayer ZnO(0001) on Au(111), respectively. [43]

Another study of ZnO on Au(111) focused on the transition from the graphene-like structure to the bulk wurtzite structure, as shown in Figure 1.15. Using STM and DFT calculations, the transition is found to occur around four layers of ZnO [44], which is in agreement with the aforementioned ZnO/Ag(111) system.

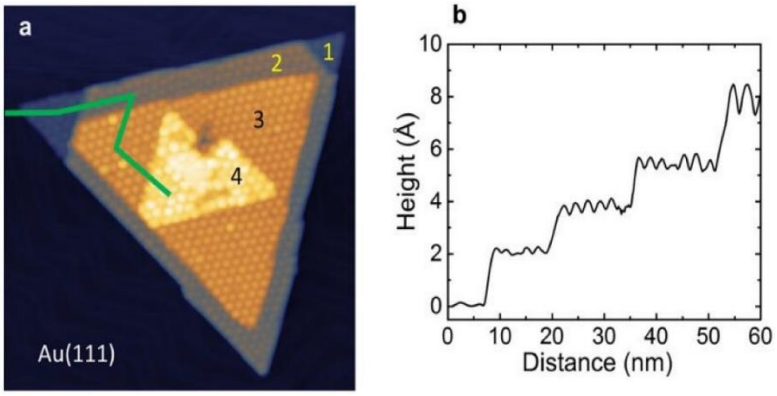

Figure 1.15: (a) STM image of a ZnO structure on Au(111) using reactive deposition method at 465 K; (b) Height profile along the solid green line in (a). [44]

As for ZnO deposited on Pd(111), a significant study was reported by Weirum and coworkers [34], who deposited Zn under 5×10^{-7} mbar O_2 at room temperature, followed by annealing in O_2 at 550 K. In the sub-monolayer range, two competing structures were observed, one is a honeycomb-like (4 × 4) phase, the other is a compact, graphene-like (6 × 6) phase, as shown in the STM images in Figure 1.16 (a) and (d), respectively. The (4 × 4) phase exhibits a honeycomb-like hexagonal unit cell (indicated in Figure 1.16 (a)) with a length of 11 Å, which corresponds to 4 times the lattice constant of the Pd(111) surface, in agreement with the p(4 × 4) LEED pattern in Figure 1.16 (b). The further DFT analysis confirms this structure has a Zn_6OH_5 stoichiometry, as shown in Figure 1.16 (c). The (6 × 6) phase shows a hexagonal structure with a lattice constant of 3.2 Å (indicated with a small rhomb in Figure 1.16 (d)), which is aligned with the in-plane lattice parameter (3.25 Å) of the ZnO(0001) surface. Moreover, a Moiré pattern with a periodicity of 16.5 Å is visible in Figure 1.16 (d), which corresponds to 6 times the Pd lattice constant or 5 time the ZnO lattice constant. This coincident lattice is reflected in the corresponding LEED pattern in Figure (e), which shows the Pd diffraction spots are surrounded by satellite spots. The subsequent DFT calculation suggests this compact phase has a Zn_6O_6 stoichiometry, as shown in Figure 1.16 (f).

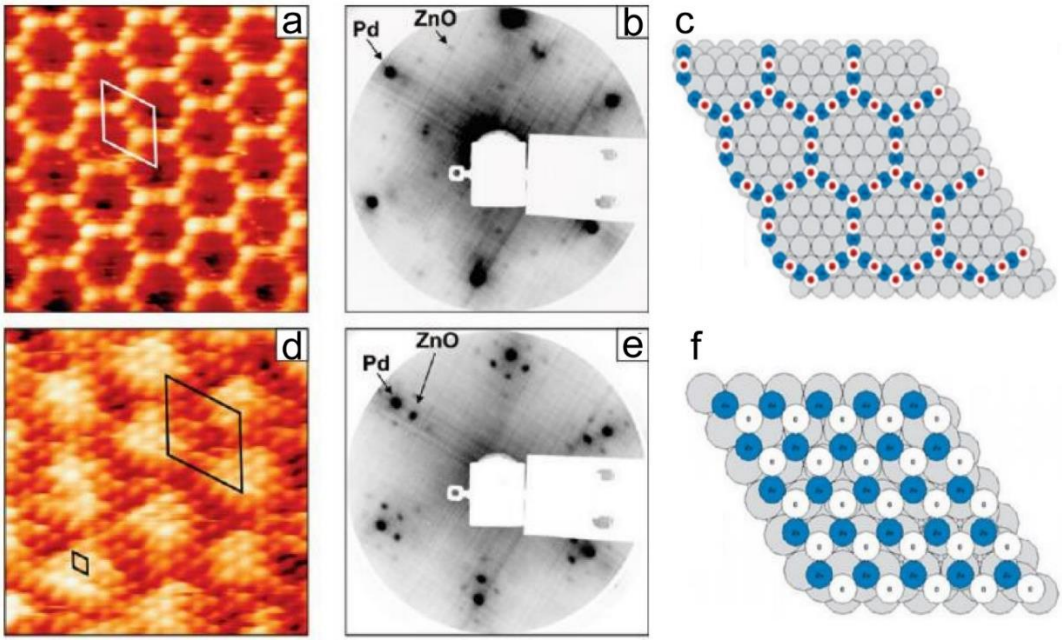

Figure 1.16: (a) High-resolution STM image of the (4 × 4) phase (65 Å × 65 Å); (b) Corresponding (4 × 4) LEED pattern; (c) Structural model of (4 × 4) phase. Pd, O, Zn and H atoms are in gray, white, blue and red, respectively; (d) High-resolution STM image of the (6 × 6) phase (50 Å × 50 Å); (e) Corresponding (6 × 6) LEED pattern; (f) Structural model of (6 × 6) phase. Pd, O and Zn atoms are in gray, white and blue, respectively. [34]

Since Pd and Pt are the siblings in the nickel family, a further study of ZnO on Pt(111) was provided by Liu and colleagues [45], who prepared ZnO films by Zn deposition in 10^{-7} mbar of O_2 at room temperature, followed by oxidation at 600 K in 10^{-6} mbar of O_2 for 5 min in order to achieve better ordered films. In the sub-monolayer ZnO regime (as shown in Figure 1.17), the (6 × 6) ZnO phase could spontaneously transform into the (4 × 4) in UHV at room temperature after several hours, which would re-transform into the (6 × 6) phase after heating at 600 K under 10^{-6} mbar of O_2. In fact, the (4 × 4) ZnO phase observed on Pt(111) and Pd(111), must be attributed to a much higher affinity of these substrates towards hydrogen than Ag(111) and Au(111), since the (4 × 4) structure has not been obtained on Ag(111) and Au(111). In addition, the residual hydrogen (possibly from water) in UHV also may play a crucial role in the formation of hydroxyls on ZnO surfaces.

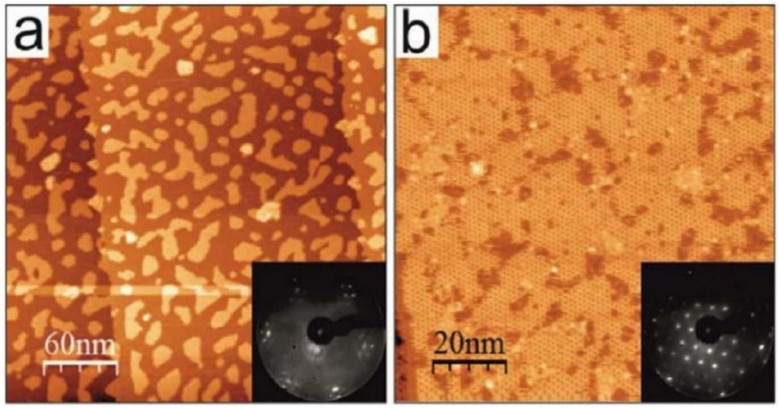

Figure 1.17: STM images and LEED patterns of the ZnO/Pt(111) surfaces at the sub-monolayer coverage: (a) as-prepared and (b) after a few hours at room temperature in UHV chamber. [45]

1.5 CO oxidation on the inverse ZnO/Pt(111) catalyst

Low temperature CO oxidation is considered as a prototype reaction on inverse oxide/Pt(111) catalysts, where 3d transition metal oxide (TMO) islands partly cover a platinum surface [46-48]. The attention of the researchers focused on the synergetic effect that could be observed at the platinum/TMO boundary [46, 48]. Indeed, the removal of pre-adsorbed CO by a steady-state flux of O_2 (under a pressure in the 10^{-8} mbar range) was observed at room temperature, both for the FeO/Pt(111) system [46] and the NiO/Pt(111) system [47], which is naturally impossible on the pure Pt(111). It was shown that the reactivity of CO oxidation increases with the FeO_{1-x}/Pt boundary length per surface unit [46], which supports the idea that the reaction takes place at the phase boundary. Further theoretical calculations addressing a series of 3d TMOs showed that the key reaction site is a coordinatively unsaturated (CUS) metal cation combined to nearby platinum atoms [48], as shown in Figure 1.18. Besides the TMO oxides (FeO and NiO) that were known experimentally to be efficient when combined with Pt(111), the theoretical calculations by Sun and coworkers [48], also explored the reactivity of a filled 3d band transition metal oxide ZnO. When compared to the pure Pt(111), the Pt-CUS Zn^{2+} ensemble favors the breaking of the O-O bond and lowers the barrier for CO oxidation by about 0.4 eV, according to calculations. Although the Pt-CUS Fe^{2+} ensemble presents a lower CO oxidation barrier than the Pt-CUS Zn^{2+} one, the single oxidation state of Zn (2+) is a tremendous advantage with respect to the former case, because the ferrous oxide can become ferric oxide under O_2 rich conditions, which is highly detrimental to its efficiency [46]. Therefore, theoretical predictions make the ZnO/Pt(111) system worthy of interest, especially in oxygen-rich CO/O_2 mixtures.

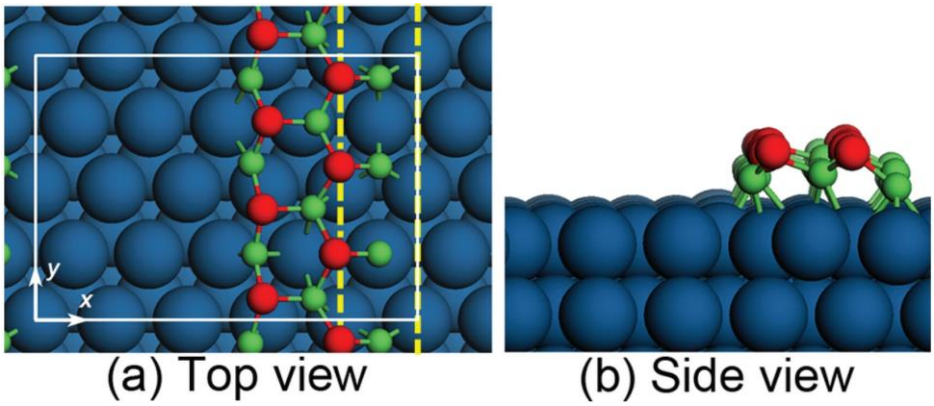

Figure 1.18: Schematic structure of the inverse TMO/Pt(111) system in top view (a) and side view (b). The supercell used is indicated by a white rectangle with in-plane x and y axes. The blue, red, and green spheres represent Pt, O, and 3d TMs atoms, respectively. [48]

The first announcement of synergetic effect for a discontinuous sub-monolayer ZnO film supported by Pt(111) was made by Martynova and coworkers in 2013 [19]. Apparently, no experiment was carried out by the Berlin group at room temperature, where synergistic effects were already observed for the "benchmark" FeO/Pt(111) system [46]. However, at a temperature of 450 K and under an oxygen-rich O_2: CO mixture (50 mbar: 10 mbar, He balance to 1 bar), the CO_2 production rate measured at the outlet of the reaction chamber was found to be circa one order of magnitude higher on the films of the partial ZnO coverage than on the bare Pt(111), as shown in Figure 1.19. Indeed, at this temperature the pure Pt(111) surface may still be CO poisoned, as a technique like near-ambient pressure photoemission spectroscopy (NAP-XPS) indicates that in oxygen-rich mixtures the transition between CO-Pt(111) to O-Pt(111) occurs in 515-535 K range, which was reported by Knudsen and coworkers [49]. Therefore, the activation of Pt-CUS Zn^{2+} sites can be effective at 450 K for CO oxidation.

Given the promises of the ZnO/Pt(111) system in low temperature CO oxidation, further studies need to be performed, focusing on several issues that were not addressed in the pioneering work of Martynova and coworkers [19]. First, instead of a single temperature (450 K), CO oxidation should be examined in a wide range of temperatures, from room temperature, where the added value of "inverse" catalysis is prominent due to the poisoning of Pt by CO, to the high temperature regime above ~ 520 K, where Pt itself is the most reactive [50] (the active phase is the O-covered metallic Pt(111) surface by Ertl and coworkers [51] when CO has desorbed from Pt areas). Second, information on the chemical species presented at the ZnO/Pt(111) surface should be collected when it is exposed to the O_2: CO mixture, as the preceding work [19] was based on the gas composition measurements (at the chamber outlet) and the "post-mortem" STM observation of the surfaces. Another major aspect that has not

been addressed in previous studies concerns the identification of intermediate species in the CO oxidation reaction. Our study provides a better investigation in this regard and hence offers a clear understanding of the mechanism of the CO oxidation reaction.

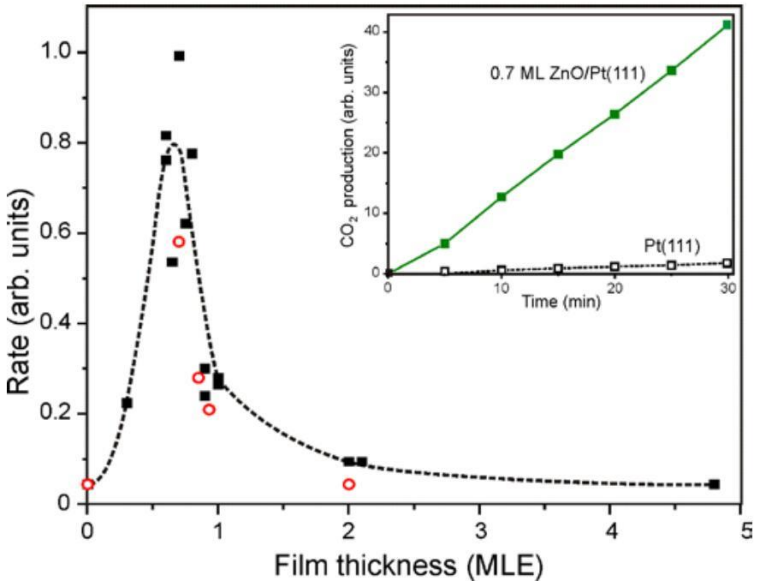

Figure 1.19: CO_2 production rate measured over ZnO films on Pt(111) as a function of the nominal film thickness (in MLE). The solid and open symbols show data for the films prepared using reactive Zn deposition at 85 and 300 K, respectively. The inset shows kinetic curves for CO_2 production on the pure Pt(111) and 0.7 ML ZnO(0001) film. [19]

Chapter 2: Experimental setup

The experiments reported in the thesis were conducted in two independent ultrahigh vacuum (UHV) chambers, one related to the scanning tunneling microscopy (STM) measurements, and the other dedicated to the synchrotron near-ambient pressure X-ray photoelectron spectroscopy (NAP-XPS) measurements. Both UHV systems for STM and NAP-XPS measurements comprise two chambers, one is the preparation chamber equipped with the electron beam evaporator (e-beam evaporator), low-energy electron diffraction (LEED), and the facilities for crystal cleaning, and the other is the analysis chamber containing a STM microscope (a variable temperature XA microscope from Omicron NanoTechnology) or an NAP-XPS analysis setup.

2.1 Electron beam evaporation (e-beam evaporation)

Zinc evaporation is performed using e-beam evaporation in UHV conditions method. Figure 2.1 shows the e-beam evaporator and the schematic of e-beam evaporation process, respectively. Zn wires (diameter = 2 mm, purity = 99.5%) are contained in a Mo crucible in the evaporator. When the evaporator works, the crucible is bombarded with electron beams from a tungsten filament controlled by a power supply. Consequently, Zn wires are heated in the crucible above the melting temperature (692.68 K). Zn atoms in the vapor phase precipitate and then form a thin film onto the Pt(111) single crystal.

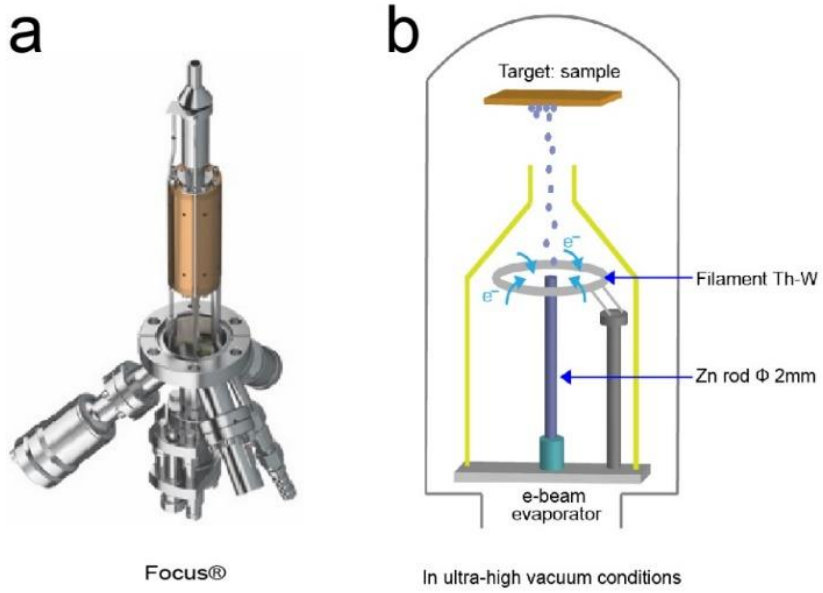

Figure 2.1: (a) E-beam evaporator; (b) Schematic of e-beam evaporation process.

2.2 Scanning tunneling microscopy (STM)

Scanning tunneling microscopy was invented by Gerd Binnig and Heinrich Rohrer [52-54] in 1982, who were awarded the 1986 Nobel physics prize in physics. STM has proven to be a powerful technique in surface nanoscience and nanotechnology over the past three decades, which provides access to investigate the surface topography with atomic resolution, the local density of states in samples ranging from metal, semiconductors to superconductors, and manipulate individual atoms and molecules on the sample surface.

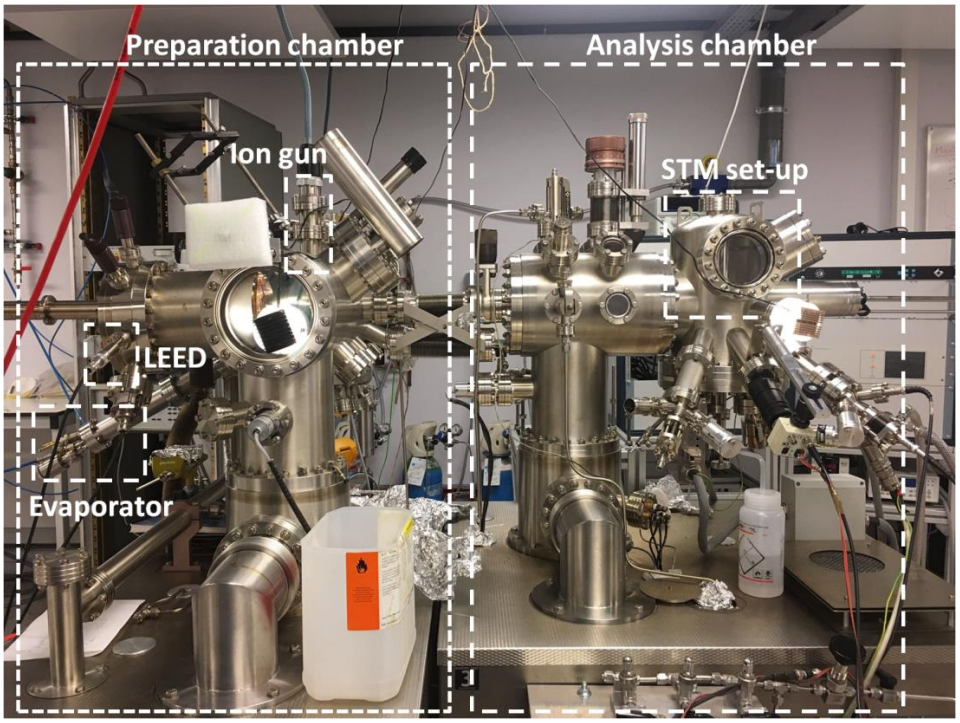

Figure 2.2: The STM setup of Laboratoire de Chimie Physique - Matière et Rayonnement of Sorbonne Université in France.

2.2.1 Theory of scanning tunneling microscopy

The concept of quantum tunneling effect plays an important role in the design and development of STM, as shown in Figure 2.3(a). In classical physics, an electron cannot penetrate or cross a barrier if its energy is smaller than the energy of the barrier. However, in quantum mechanics, an electron can tunnel through a barrier with some probability. Figure 2.3(b) shows the process of an electron crossing a potential barrier. For a rectangular barrier, the wave function of an electron in the direction z is described by the Schrodinger's wave equation as:

$$\left(-\frac{\hbar^2}{2m^*}\nabla^2 + V(z)\right)\Psi(z) = E\psi(z) \tag{4}$$

where $\hbar$ is the reduced Planck constant, Ψ is the wave function of the electron, m^* is the effective mass of the electron, ∇^2 is the Laplacian, E is the energy of the electron and $V(z)$ is the potential energy. Particularly, the potential energy $V(z)$ varies with the position z, which causes the Schrodinger wave equation becomes a non-constant coefficient differential equation. Therefore, to solve this problem, the Schrodinger wave equation is separated in three regions where $V(z)$ is constant in each region, which are

$$\text{Region (I)}: z < 0, V = 0 \tag{5}$$

$$\text{Region (II)}: 0 \le z \le a, V = V_0 \tag{6}$$

$$\text{Region (III)}: z > a, V = 0 \tag{7}$$

Consequently, the corresponding solution of the Schrodinger wave equation in each region is

$$\text{Region (I)}: \psi(z)_{\text{I}} = A_1 e^{ikz} + A_1' e^{-ikz} \tag{8}$$

$$\text{Region (II)}: \psi(z)_{\text{II}} = A_2 e^{Kz} + A_2' e^{-Kz} \tag{9}$$

$$\text{Region (III)}: \psi(z)_{\text{III}} = A_3 e^{ikz} + A_3' e^{-ikz} \tag{10}$$

where A_1, A_1', A_2, A_2' and A_3 are constants, $k = \sqrt{\frac{2m_e E}{\hbar^2}}$ and $K = \sqrt{\frac{2m_e(V_0 - E)}{\hbar^2}}$. Since there is no potential disturbance to reflect the wave in Region (III), $A_3' = 0$.

By following the boundary conditions at $z = 0$ and $z = a$, which are

$$\psi(0)_{\text{I}} = \psi(0)_{\text{II}} \tag{11}$$

$$\psi^{\prime}(0)_{\text{I}} = \psi^{\prime}(0)_{\text{II}} \tag{12}$$

$$\psi(a)_{\text{II}} = \psi(a)_{\text{III}} \tag{13}$$

$$\psi^{\prime}(a)_{\text{II}} = \psi^{\prime}(a)_{\text{III}} \tag{14}$$

The tunneling probability can be obtained as

$$T = \left|\frac{A_3}{A_1}\right|^2 = \frac{4(V_0 - E)E}{4(V_0 - E) + V_0^2 sin^2(Ka)} \tag{15}$$

which is the squared modulus of the ratio between the probability density of the transmitted electrons and the probability density of the incident electrons. If $Ka \gg 1$, T can be simplified as

$$T \approx \frac{16(V_0 - E)E}{V_0^2} e^{-2Ka} \tag{16}$$

which means the tunneling probability decreases exponentially with the width of the potential barrier.

The electron tunneling can also be described by the Bardeen's model [55], which uses time dependent perturbation theory. Using Fermi's golden rule, the tunneling current between the tip and sample is expressed as:

$$I = \frac{4\pi e}{\hbar} \int_{-\infty}^{+\infty} [f(E_F - eV + E) - f(E_F + E)] \rho_T(E_F - eV + E) \rho_S(E_F + E) |M_{TS}|^2 dE \tag{17}$$

where $f(E)$ is the Fermi-Dirac distribution, $\rho_T(E)$ is the local density of state of the tip, $\rho_T(E)$ is the local density of state of the sample, eV is the energy shift caused by the applied bias on the sample and M_{TS} is the tunneling matrix element. In principle, it is possible to calculate the tunneling current using the Bardeen's model. However, the structure of the tip is not straightforward to be obtained experimentally which complicates the simulation of the STM tip. Based on the Bardeen's model, Tersoff and Hamann formulated a model of the STM tunneling junction with a spherical tip (the s-wave tip model), which is widely used nowadays [56, 57]. Due to the approximation of the s-wave tip wave function, the tunneling current can be simplified in the following way:

$$I(V) \propto V \rho_T(E_F) e^{2kR} \sum_v |\psi_v(r_0)|^2 \delta(E_v - E_F) \tag{18}$$

where R is the radius of curvature, r_0 is the tip position, $\rho_T(E_F)$ is the tip density of states, $k = \sqrt{2m\Phi_{eff}}/\hbar$ is the inverse decay length inside a vacuum barrier with the local work function Φ_{eff}, and $\sum_v |\psi_v(r_0)|^2 \delta(E_v - E_F)$ is related to the surface local density of states $\rho(\overrightarrow{r_0}, E)$. Therefore, the tunneling current is proportional to the density of states (DOS) of the sample surface at the tip position $\overrightarrow{r_0}$:

$$I(V) \propto \rho(\overrightarrow{r_0}, E) \tag{19}$$

The Tersoff and Hamann model is of paramount importance in interpretation of STM images. However, this model only represents an approximation with the s-wave function of the tip electronic states. To overcome the problem from the Tersoff and Hamann model, a generalized model is put forward. In this case, a finite bias window between the tip and the sample surface and a transmission coefficient are considered. The tunneling current is thus integrated as:

$$I(V) \propto \int_{E_F}^{E_F+eV} \rho_T(E-eV)\rho_S(E)T(z,E,eV)dE \tag{20}$$

where ρ_T and ρ_S are density of states of the tip and the sample surface, respectively. $T(z,E,eV)$ is the transmission coefficient between the tip and the sample, E is the energy, V is the bias voltage and z is the tunneling distance. In a first approximation, the density of states of the tip ρ_T and the transmission coefficient $T(z,E,eV)$ are assumed constant when a small bias voltage is given. As a result, the tunneling current can be considered proportional to the density of states of the sample surface, which is integrated in (E_F, E_F+eV) energy window.

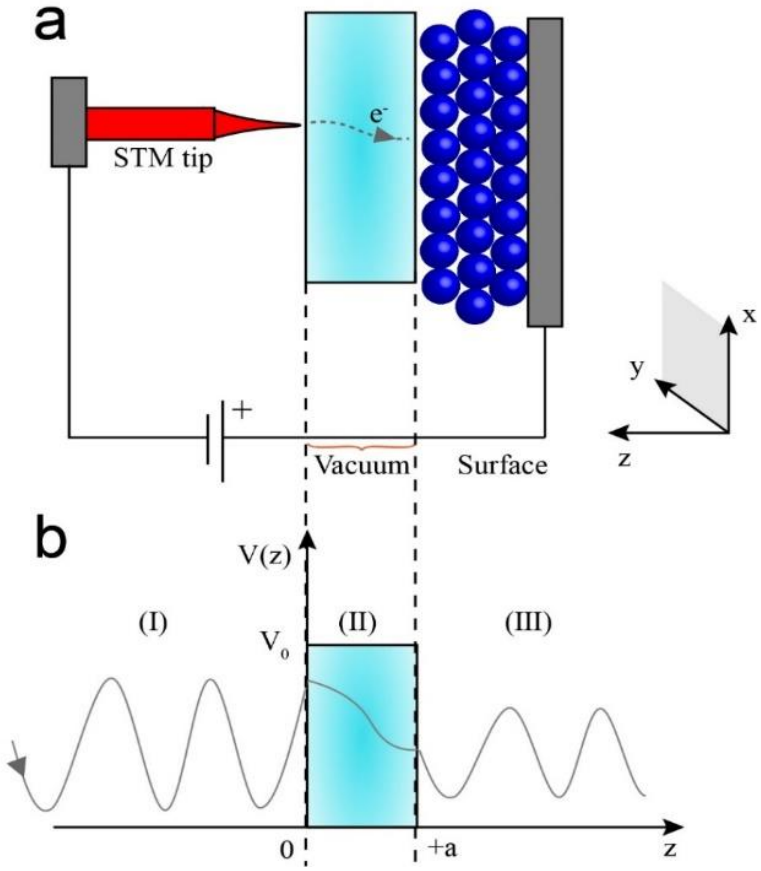

Figure 2.3: (a) Illustration of the tunneling process; (b) Electrons pass through on a potential barrier.

2.2.2 **Description of scanning tunneling microscopy**

Figure 2.4(a) shows the schematic of an STM setup. A tip is a significant ingredient of the STM setup, which is attached to a piezoelectric tube. The piezoelectric tube consists of three mutually perpendicular piezoelectric transducers, which are x, y and z, respectively. Once a voltage is applied, the piezoelectric transducers can expand or contract to make the tip move on

the sample surface. Using the coarse approach and the subsequent fine approach, the tip can be brought to the sample surface within few Ångströms. In this case, the electron wavefunction of the tip is overlapped with the electron wavefunction of the sample. Upon applying a voltage, a tunneling current can be generated between the tip and the sample, which decays exponentially with the tip-sample distance. Therefore, the tunneling current is highly sensitive to adjust the tip-sample distance.

When the tip starts to scan the sample surface along the x and y directions, there are two scanning modes, which are the constant current mode and the constant height mode, shown in Figure 2.4(b) and (c), respectively. In the constant current mode, the tunneling current is converted to a voltage by the tunneling current amplifier, which is then compared with a reference value. The difference from the reference value is amplified to drive the z piezo to move on the sample surface: if the tunneling current is smaller than the reference value, the voltage then applied to the z piezo tends to extend the tip towards the sample surface, and vice versa. In this case, the feedback loop adjusts the distance z between the tip and the sample surface at each point of x and y for keeping the tunneling current constant during scanning. In the constant height mode, the tip-sample distance z is fixed during the two-dimensional scanning (x and y). Comparing to the constant current mode, the constant height mode is suitable for a flat sample surface, otherwise, the tip might have a high risk of crashing into the sample surface.

As the tip scans over the sample surface along the x and y direction, the equilibrium z positions, which represent a contour plot of the corresponding tunneling-current surface, is acquired and displayed in the computer. Generally, the bright spots in an STM image indicate high z values (e.g. protrusions) and the dark spots refer to the low z values (e.g. holes and pits). For a more quantitative illustration of the topography of the sample, a line scan is often applied in an STM image, in which the unit of x or y is nanometer (nm) and the unit of z is picometer (pm).

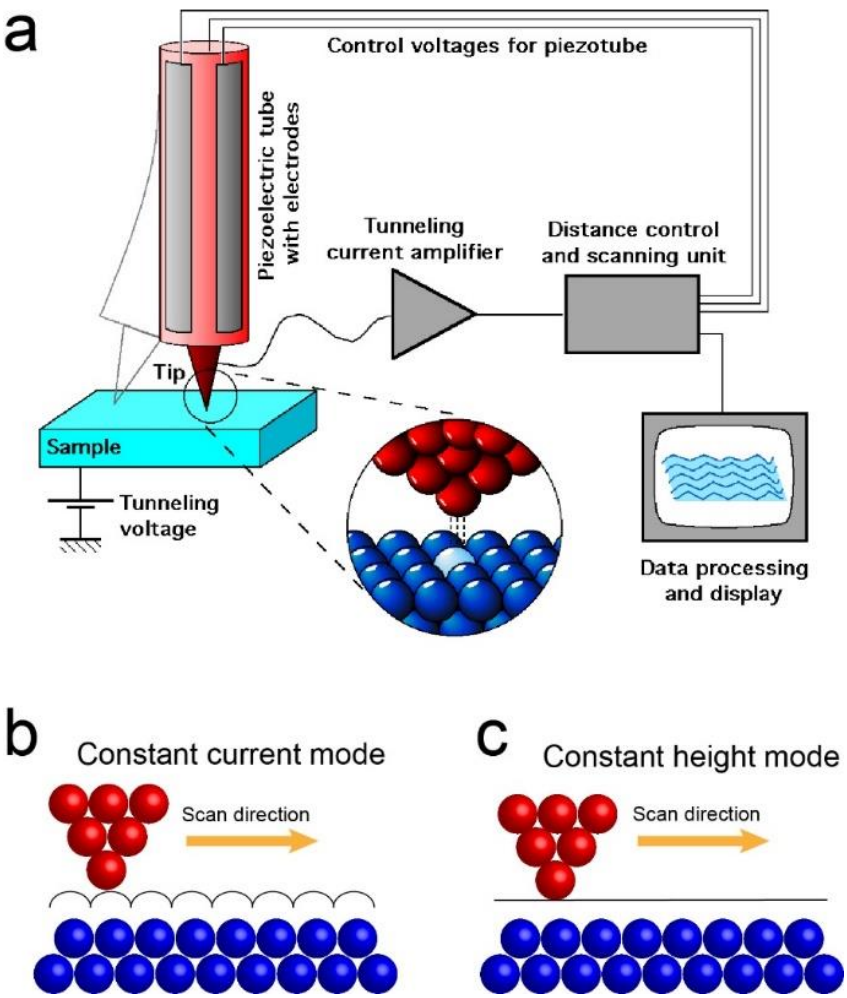

Figure 2.4: (a) Schematic representation of an STM setup. The movements of x, y and z piezo are controlled by a computer. Source: http://en.wikipedia.Org/wiki/Scanning _ tunneling _ microscope; (b) Constant current mode; (c) Constant height mode.

2.2.3 **Fabrication and cleaning of the tip for scanning tunneling microscopy**

The tip quality is important because it determines the performance of the scanning tunneling microscope. Specifically, the tip shape (mechanical rigidness), geometry (sharpness) and chemical composition (cleanness) are three key elements for acquiring a high resolution STM image [58]. Tungsten (W) tip are widely used in the UHV conditions because of its high melting temperature (3695 K), the great mechanical strength and the simple fabrication using an electrochemical etching method. Figure 2.5(a) shows the schematic of the electrochemical etching method for a W tip fabrication, which is called the drop-off technique of the electrochemical etching [59]. During the etching process, the highest etching rate of the W wire (Φ = 0.25 mm) occurs at the interface between air and an electrolyte (2M NaOH), which

gradually causes the necking and dropping of the bottom part of the W wire in NaOH, eventually results in a STM tip formation, as shown in Figure 2.5(b) and (c). The tip sharpness mainly affected by the dropping part (immersed part) of the W wire in NaOH. For example, the big weight of the dropping part may cause the tip bending and recoil, making the apex of the tip deformative and blunt. The small weight of the dropping part may cause the immersed W wire completely dissolved in NaOH. In a word, the proper immersed length of the W tip in NaOH is very significant for making a sharp tip, however the suitable parameter of the immersed length is usually obtained empirically.

Once the W tip is fabricated after the electrochemical etching process under the ambient conditions, the tip is inevitably covered by a thin residual layer of tungsten oxide and various contaminants, such as residuals and hydrocarbon from the electrolyte and ambient conditions [58]. Therefore, an annealing procedure of the tip in the UHV chamber is very mandatory to remove the surface oxide and contaminants of the tip. Moreover, the annealing process can reduce the plastic deformation and other stress-induced defects of the tip caused by the etching process [60].

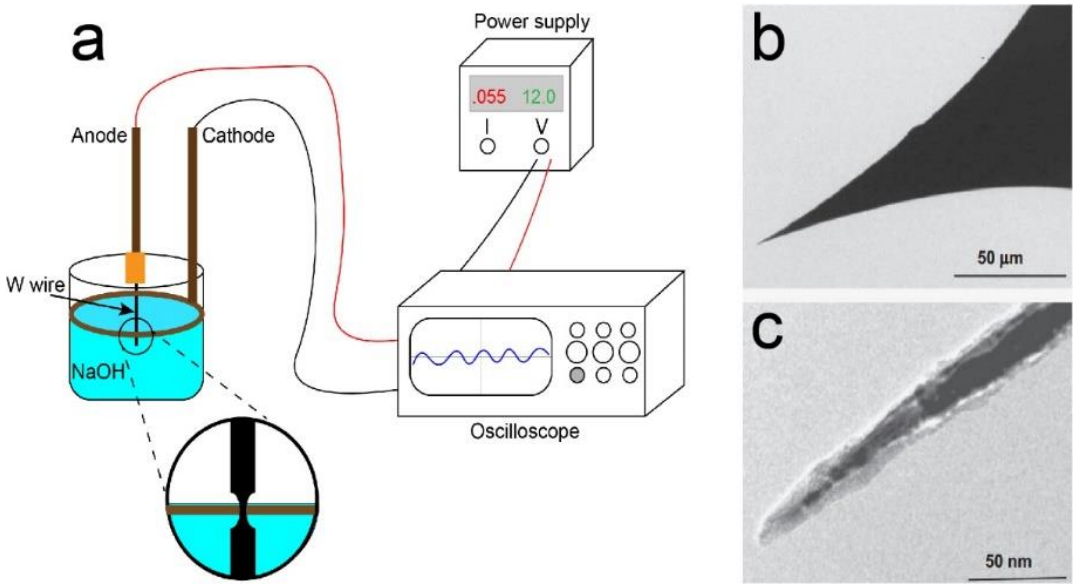

Figure 2.5: (a) Schematic of the electrochemical etching for a tip fabrication; (b) and (c) are low- and high-magnification transmission electron microscope (TEM) images of the W tip fabricated with an electrochemical etching technique [58].

2.3 Scanning tunneling spectroscopy (STS)

Not only can the STM setup image the topography of the sample surface, but it can also measure the local electronic features by taking the scanning tunneling spectroscopy on the

sample. In general, the feedback loop of the STM is off when the tip is positioned at an interesting area of the sample. Then the voltage ramps and keeps a constant tip-sample distance, meanwhile the tunneling current is obtained over the desired range of the voltages. The changes of the slopes in the I-V curve reflects the variations of conductance between the tip and the sample. If the density of states of the tip ρ_T and the transmission coefficient $T(z, E, eV)$ are assumed constant in the considered range of the bias voltage, the derivation of Equation (20) related with the bias voltage V is expressed simply as:

$$\frac{dI}{dV} \propto \rho_T(E_F)\rho_S(E_F + eV)T(z, E_F + eV, eV) \tag{21}$$

In principle, the measurement of dI/dV is a good approximation to the local density of states (LDOS) of the sample surface at the bias voltage V applied between the sample surface and the tip.

Figure 2.6 (a) and (b) show the two schematics of the tunneling processes. Once the positive sample bias voltage is applied (Figure 2.6(a)), the electrons tunnel from the occupied states of the tip to the unoccupied states of the sample, which probes the empty states of the sample (LUMO, the lowest unoccupied molecular orbital). On the contrary, when the negative sample bias voltage is applied (Figure 2.6 (b)), the electrons tunnel from the occupied states of the sample to the unoccupied states of the tip, which probes the filled states of the sample (HOMO, the highest occupied molecular orbital). Figure 2.6(c) gives an example of the I-V curve of STS measured on a semiconductor and the corresponding conductance dI/dV calculated from the I-V curve. In this schematic, the surface band gap of the sample can be recognized both from the I-V curve and the conductance dI/dV curve. Particularly, the HOMO and LUMO states of the sample near Fermi level can be observed from the conductance curve.

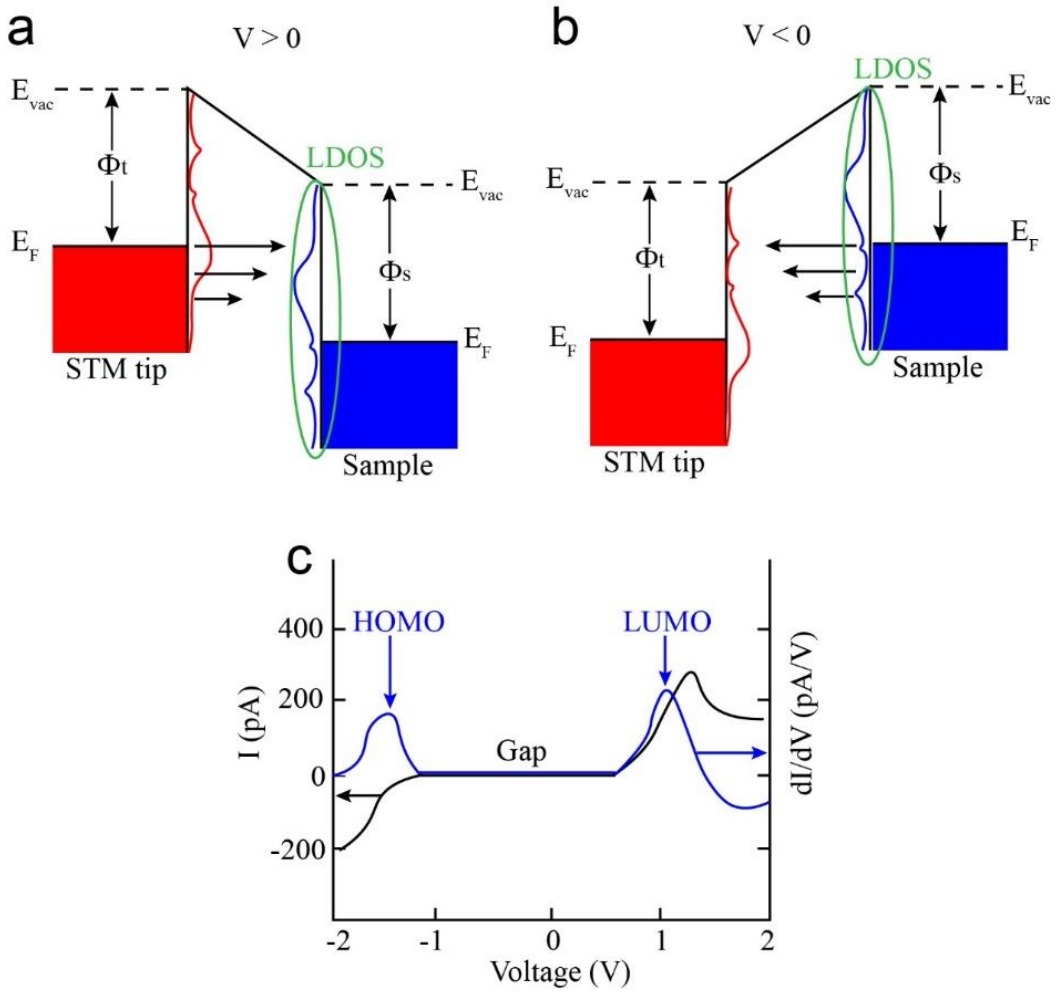

Figure 2.6: (a) Schematic of positive sample bias; (b) Schematic of negative sample bias; (c) Schematic of the I-V curve and the corresponding differential conductance dI/dV-V curve.

2.4 Low-energy electron diffraction (LEED)

Low-energy electron diffraction was discovered by Davisson and Germer in 1927 [61, 62] and did not become a popular tool for surface analysis until 1960 due to the inadequate vacuum techniques and the slow detection methods. LEED is a science tool which is very sensitive to determine the surface structure. The basic reason of the high surface sensitivity of LEED is that the mean free path of the electron is very low (5-10 Å) in solid materials based on the energy range of low-energy electrons (20-200 eV). In this case, a few atomic layers of the sample are detected by the electron beam and consequently the scattered electrons originate specifically from the sample surface.

2.4.1 **Description of low-energy electron diffraction**

Figure 2.7 shows a typical setup of LEED. In the electron gun, electrons are emitted by a cathode filament with a negative potential ranging from 10 to 600 V, which is respect to the sample. Then the electrons are focus into a beam, around 0.1-0.5 mm wide, by a series of electron lenses. Some of the electrons incident on the sample are reflected and collected by a fluorescent screen. The electric potential of the fluorescent screen rises to 3-7 kV to energize the electrons, which makes the electrons are strong enough to excite the screen. The grids, which are in between the screen and the sample, are used to cut off the inelastically scattered electrons which carry no structural information about the sample surface.

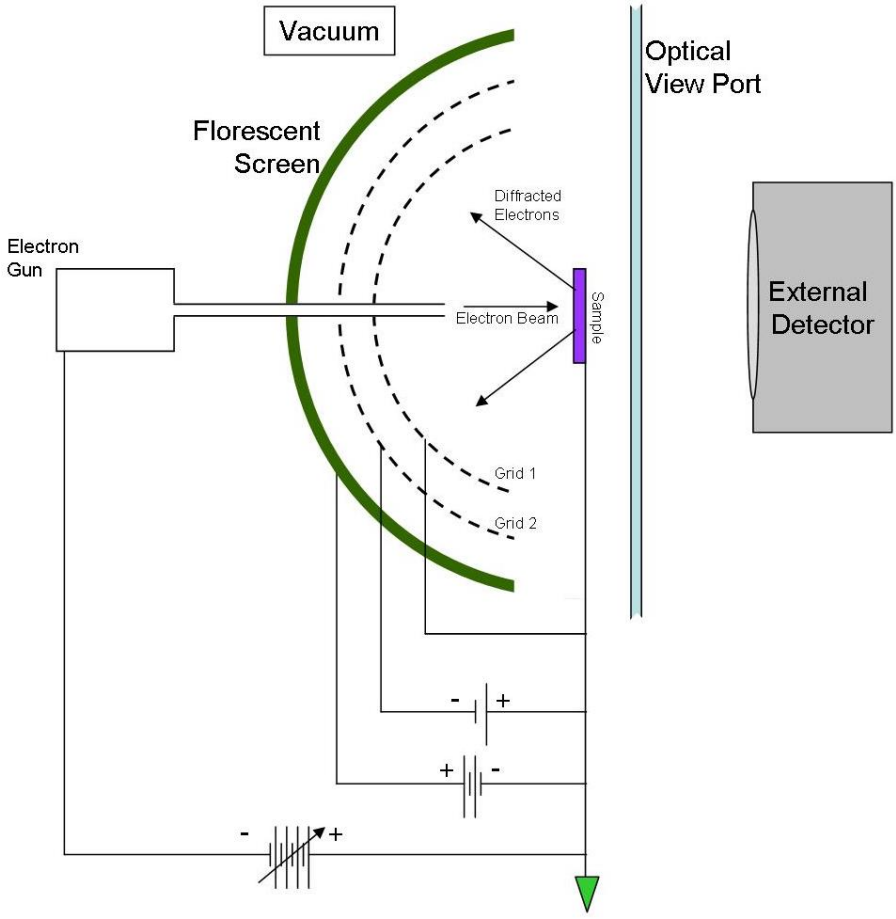

Figure 2.7: Schematic of a LEED setup. Source: https://en.wikipedia.org/wiki/Low-energy_electron_diffraction.

2.4.2 **Theory of low-energy electron diffraction**

It is very convenient to describe the interaction between scattered electrons and incident electrons in reciprocal space. In three dimensions, the correlation between the real space lattice $\{\boldsymbol{a}, \boldsymbol{b}, \boldsymbol{c}\}$ and the reciprocal lattice $\{\boldsymbol{a}^*, \boldsymbol{b}^*, \boldsymbol{c}^*\}$ is expressed as:

$$\boldsymbol{a}^* = \frac{2\pi \boldsymbol{b} \times \boldsymbol{c}}{\boldsymbol{a} \cdot (\boldsymbol{b} \times \boldsymbol{c})} \tag{22}$$

$$\boldsymbol{b}^* = \frac{2\pi \boldsymbol{c} \times \boldsymbol{a}}{\boldsymbol{b} \cdot (\boldsymbol{c} \times \boldsymbol{a})} \tag{23}$$

$$\boldsymbol{c}^* = \frac{2\pi \boldsymbol{a} \times \boldsymbol{b}}{\boldsymbol{c} \cdot (\boldsymbol{a} \times \boldsymbol{b})} \tag{24}$$

The condition of the constructive interference is described by the Laue condition,

$$\boldsymbol{k} - \boldsymbol{k}_0 = \boldsymbol{G}_{hkl} \tag{25}$$

where $\boldsymbol{k}_0$ is the wave vector of an incident electron ($k_0 = 2\pi/\lambda_0$) and $\boldsymbol{k}$ is the wave vector of a scattered electron ($k = 2\pi/\lambda$).

$\boldsymbol{G}_{hkl}$ is a vector of the reciprocal lattice and can be represented by

$$\boldsymbol{G}_{hkl} = h\boldsymbol{a}^* + k\boldsymbol{b}^* + l\boldsymbol{c}^* \tag{26}$$

where (h, k, l) is a set of integers. Since elastic scattering is only considered, the magnitudes of the incident wave vector and the scattered wave vector are unchanged, $|\boldsymbol{k}_0| = |\boldsymbol{k}|$. As we discussed above, LEED is very sensitive to the sample surface which is due to the mean free path of the low energy electrons in a crystal. In that case, the diffraction equation (23) reduces to the two-dimensional form:

$$\boldsymbol{G}_{hk} = h\boldsymbol{a}^* + k\boldsymbol{b}^* \tag{27}$$

where $\boldsymbol{a}^*$ is perpendicular to $\boldsymbol{b}$ with the magnitude $|\boldsymbol{a}^*| = \frac{1}{|a| \sin \alpha}$, $\boldsymbol{b}^*$ is also perpendicular to $\boldsymbol{a}$ with $|\boldsymbol{b}^*| = \frac{1}{|b| \sin \alpha}$ and α is the angle between the real space vector $\boldsymbol{a}$ and $\boldsymbol{b}$.

2.4.3 **Surface structures**

Considering LEED patterns are the periodic diffraction patterns in two dimensions, the general term “surface structure” should be mentioned. A surface structure could either be the surface structure of the substrate material or could be related to the structure of a deposit [63]. Different from the atoms in the bulk, the atoms near the surface usually experience the surface reconstruction or relaxation to be stabilized. Referring to the surface reconstruction, the Wood’s notation is commonly used:

$$X(hkl)\ m \times n - R\phi \tag{28}$$

which describes the reconstruction of the (hkl) plane of a material. m and n are given as multiples of the non-reconstructed surface unit cell vectors a and b. For example, in Figure 2.8(a) and (b), (2×2) reconstruction means that vectors of the unit cell (green balls) are twice longer than those of the unit cell of the non-reconstructed structure underneath (grey balls). Once the unit cell is rotated with respect to the unit cell of the non-reconstructed surface, the angle ϕ is given additionally. The example is shown in Figure 2.8(c), which indicates the unit cell of the reconstructed surface (green balls) are rotated 30° with respect to the unit cell of the surface underneath (grey balls).

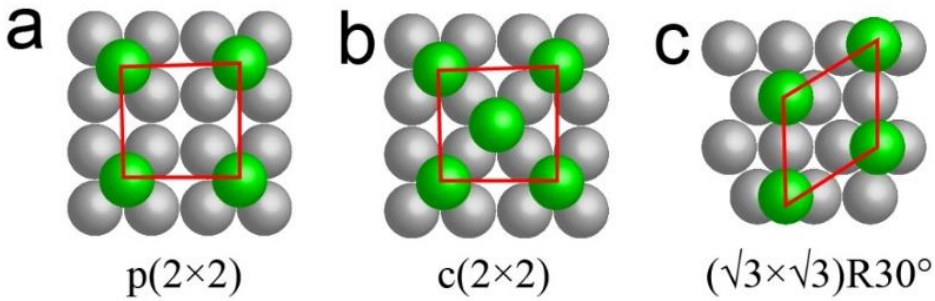

Figure 2.8: (a) p(2×2) structure (green) on the square lattice (grey); (b) c(2×2) structure (green) on the square lattice (grey); (c) $(\sqrt{3} \times \sqrt{3})$R30° structure (green) on the hexagon lattice (grey). In general, p indicates primitive and c indicates centered.

2.5 Near-ambient pressure X-ray photoelectron spectroscopy (NAP-XPS)

XPS is a surface-sensitive quantitative analysis technique. With the development of a high-resolution XPS by Kai Siegbahn and his research group in Uppsala University in Sweden [64], XPS allowed to measure accurate binding energy of photoelectron peaks, in which the investigation of electronic structure has been realized. The work of Kai Siegbahn was awarded by the physics Nobel prize in 1981.

2.5.1 Principle of X-ray photoelectron spectroscopy

An XPS measurement is operated by irradiating the sample surface with a beam of monochromatic X-rays. If the photon energy is high enough, electrons from the sample atoms can be excited and create the photoelectrons, which are then emitted from the sample surface. Figure 2.9 is the schematic of a photoemission process. In this process, the electrons on a given orbital are first promoted from a bound state to an excited state by absorbing certain photon energy $h\nu$. Before escaping to vacuum, the photoelectrons travel some distance inside the

sample, in which the photoelectrons collide elastically or inelastically with the lattice atoms of the sample. The elastically scattered electrons escape from the sample surface without any kinetic energy loss, which will form the main XPS core level peak (also called adiabatic peak). On the contrary, the inelastically scattered electrons escape from the sample surface with losing a part of the kinetic energy, which will create the background of the XPS spectrum. Therefore, the surface sensitivity of XPS is determined by the electron inelastic mean free path (IMFP), which is the characteristic length that an electron on average travels through before suffering an inelastic scattering. After reaching the sample surface, the photoelectrons still need to overcome a barrier potential which exist at the sample surface in order to get to the vacuum level. That barrier potential refers to the work function of the sample.

In general, the binding energy of a photoelectron coming from the sample can be obtained by the Einstein equation:

$$E_b = h\upsilon - E_k - \Phi_{sample} \tag{29}$$

where E_b is the binding energy of the core level, $h\upsilon$ is the photon energy of the X-ray, , E_k is the kinetic energy and Φ_{sample} is the work function of the sample.

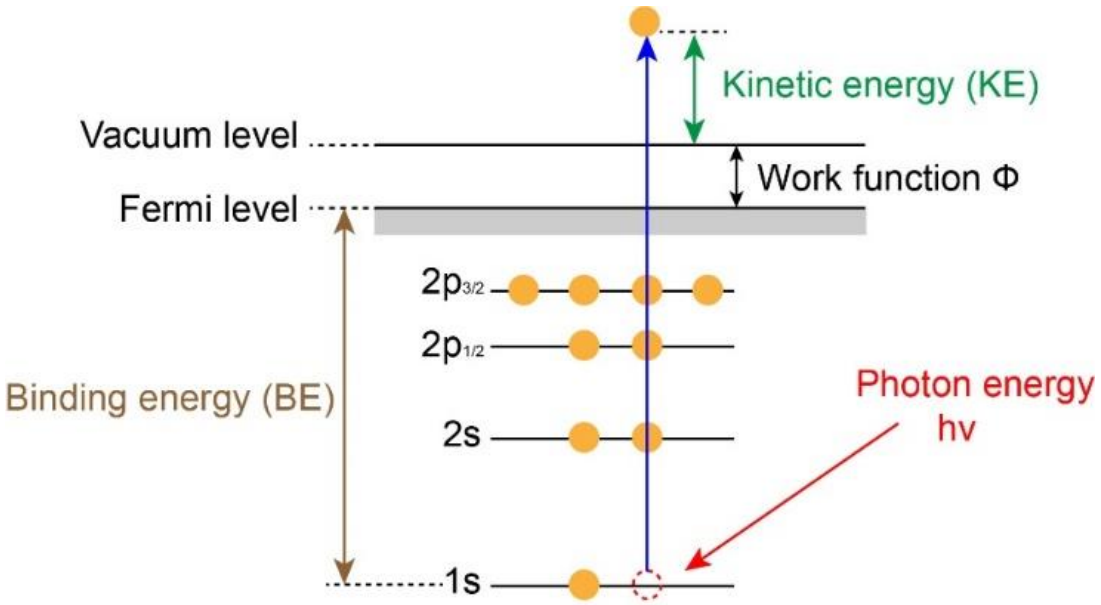

Figure 2.9: Schematic of the photoemission process.

Particularly, when the kinetic energy is measured by the XPS analyzer (Figure 2.10), the work function of the analyzer should be considered. By grounding both the sample and the analyzer to align the Fermi level, the equation (29) can be rewritten as:

$$E_k = h\upsilon - E_b - \Phi_{analyzer} \tag{30}$$

where E_b is the binding energy of the core level, hv is the photon energy of the X-ray, , E_k is the kinetic energy and $\Phi_{analyzer}$ is the work function of the analyzer.

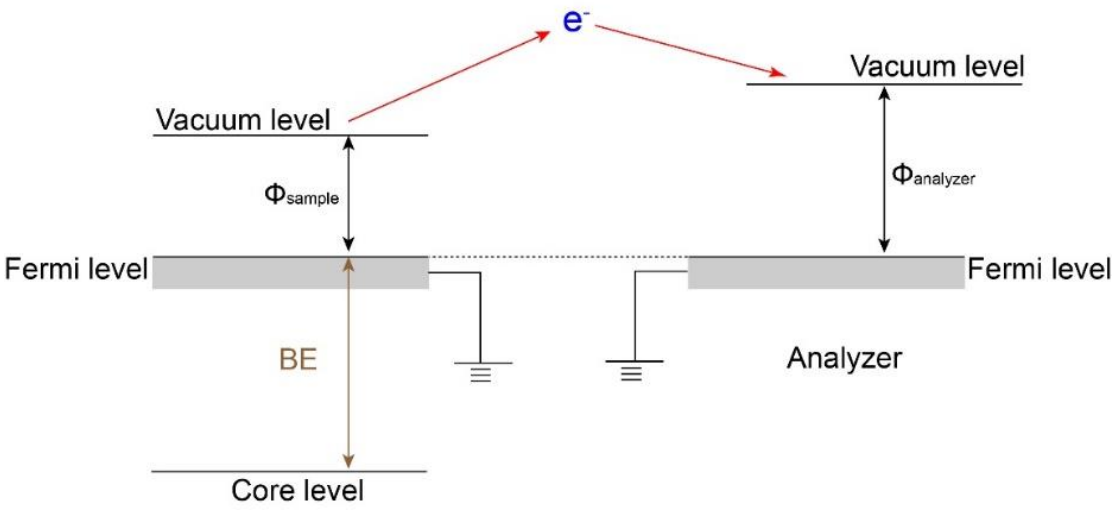

Figure 2.10: Schematic of the sample and analyzer energy level.

The binding energy of a core electron measured by XPS is influenced by the interactions between the electron and the surrounding environment, which are Coulomb interactions with other electrons and the attraction from the nuclei. Changes in the chemical environment have an influence on the valence electron of the element, which then lead the electrons to a spatial redistribution and affect the value of the binding energy of the core electron. Consequently, the variation of the binding energy of the core electron is observed as a shift on the XPS peak of the core electron, which is called the chemical shift ($\Delta\xi$). Due to the advantage of XPS, chemical shift can be easily interpretable in XPS spectrum with a well-defined energy position, such as the different oxidation state and different chemical environment.

Due to the spin-orbit splitting effect, all orbital levels (except s orbital) will show two spin-orbit splitting peaks in XPS spectrum, i.e. doublet pairs. Based on the quantum mechanics, the total angular momentum (j) is expressed as:

$$j = l + s \tag{31}$$

where l is the orbital angular momentum ($l = 1$ for p orbital, $l = 2$ for d orbital and $l = 3$ for f orbital) and s is the spin angular momentum ($s = \pm 1/2$). The formula (31) gives two values j_1 and j_2, which corresponds to the two peaks due to splitting, respectively. (e.g. $nf_{5/2}$ and $nf_{7/2}$, where n is the principal quantum number.) Moreover, the relative intensities of the doublet pairs are given by $\frac{j_1+1}{j_2+1}$. Thus, for p electrons the relative intensities are $1:2$, while for d electrons the relative intensities are in the proportion $2:3$ and for f orbital the ratio is $3:4$.

Also, the energy separation of the doublet pairs depends on both the principal (n) and angular momentum (j) of the core level electrons and can result in widely separated doublet pairs.

2.5.2 **Description of X-ray photoelectron spectroscopy**

Figure 2.11 shows the schematic of the XPS principal in UHV. Basically, the XPS system consists of three critical components, which are the X-ray source, the electron analyzer and the detector with appropriate signal counting electronics. Electrons are first emitted from the sample surface by the X-ray source (usually Mg/Al X-ray sources). Then they are supposed to decelerate or accelerate by the electrostatic lenses in the analyzer to the pass energy E_p and focus on the inlet slit. The potentials applied to the inner and outer hemisphere of the electron analyzer correspond to a selection of electrons with the kinetic energy E_p. Therefore, the photoelectrons are registered in a small kinetic energy range, which determines the resolution of the analyzer. Electrons are finally detected by the electron multiplier of the detector in pulse counting mode.

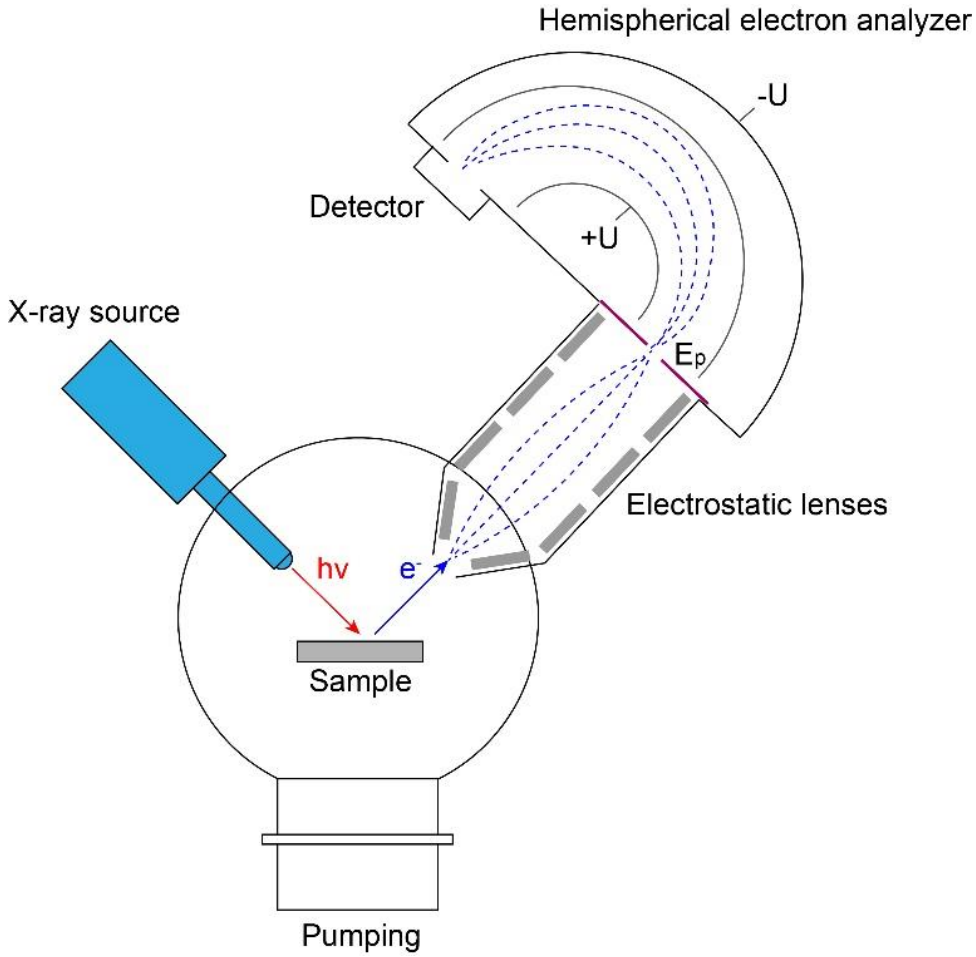

Figure 2.11: Schematic diagram of the XPS apparatus in UHV.

The XPS system should be kept in UHV because the photoelectron signal will be strongly decreased by the interaction of the photoelectrons with the atmosphere if the vacuum is not good enough. Standard XPS systems operate in a vacuum in the low 10^{-10} mbar range. Although the inelastic mean free path (IMFP) of electrons in the gas phase is determined by the kinetic energy of electrons and the gas pressure, the count rate of detected photoelectrons is exponentially decreasing with increasing the pressure of atmosphere, as shown in Figure 2.11. For example, electrons with a kinetic energy 100 eV have an IMFP around 1 mm in 1 mbar gas phase. Besides, the sample should also be kept in UHV to be clean because the sample surface will be contaminated by the gas phase if the vacuum is bad.

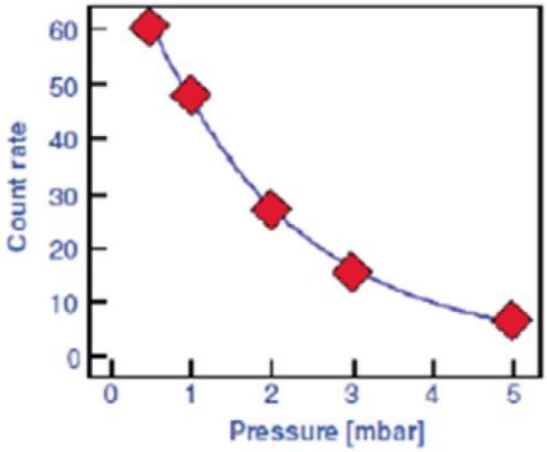

Figure 2.11: XPS signal versus increasing pressure [65].

2.5.3 **Description of near-ambient pressure X-ray photoelectron spectroscopy**

Due to the exponential decrease of the photoelectron signal in gas phase, NAP-XPS technique is designed to partially overcome the pressure gap in surface science. Unlike the ordinary XPS, NAP-XPS allows the sample to be exposed in high pressures in order of millibars, which can study the dynamics of catalytic reactions. The most significant change for NAP-XPS is the introduction of the differential pumping in the electron analyzer system which dramatically decreases photoelectron attenuation between the sample and the analyzer. The early design of the differential pumping system is shown in Figure 2.12 (a). In this design, the photoelectrons travel through differential pumping regions before reaching the analyzer, which are unfocused between the apertures. The unfocused photoelectrons would cause a serious loss in collection efficiency. Fortunately, the new design of the differential pumping system (Figure 2.12 (b)) is combined with a series of electrostatic lenses which greatly increase the electron collection rate. Different from the laboratory X-ray source (Al/Mg source) used in the XPS, the

synchrotron-based light is applied onto the NAP-XPS, which can produce a high flux of photons and a more focalized size at the sample generating more photoelectrons. Nowadays, a number of synchrotron-based NAP-XPS setups have arisen all over the world, such as SOLEIL, DIAMOND, BESSY, ALS and SSRL [66].

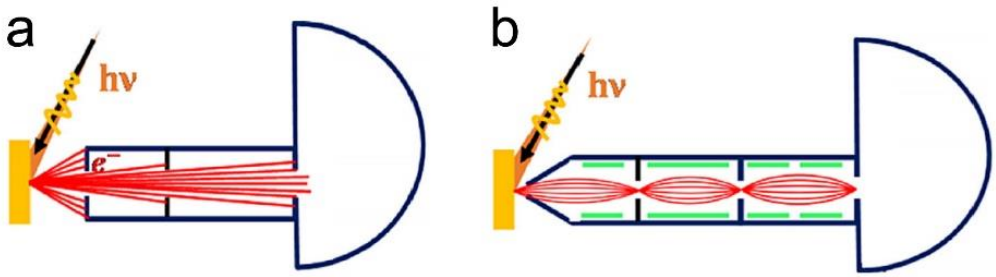

Figure 2.12: Schematic of photoelectron path from the sample to the analyzer entrance. (a) Early design of differential pumping system and (b) the new design of the differential pumping system with electrostatic lens (green lines) [67].

A schematic diagram of the SOLEIL synchrotron is shown in Figure 2.13. Several steps are involved to obtain the synchrotron radiation. First, the electron beam is emitted by the electron gun, which is then accelerated by the linear accelerator to 10 MeV. The electrons are further accelerated to 100 MeV in the booster ring and up to a maximum energy of several GeV in the storage ring where the electrons are stored. When the electron beam circulates in the storage ring, the trajectory of the electron beam is altered by the diploe magnets and the electron beam is focused by the quadrupole magnets after the change of the trajectory. The beamlines, the end stations, are installed tangentially to take advantage of the synchrotron light for experiments. Comparing to the laboratory X-rays, the synchrotron light has a very broad spectral range, which covers from microwaves to hard X- rays. Thus, the photon energy can be selected based on different experiments. As for the TEMPO beamline, the synchrotron beam, a high flux of photons with the energy range from 50 to 1500 eV, is introduced into the analysis chamber of the NAP-XPS through a Si_3N_4Al window in order to keep the beam in UHV (the pressure range of 10^{-9} mbar).The beam spot has a diameter of 0.1 mm on the sample in the analysis chamber, which makes an angle of 54˚ with the sample normal.

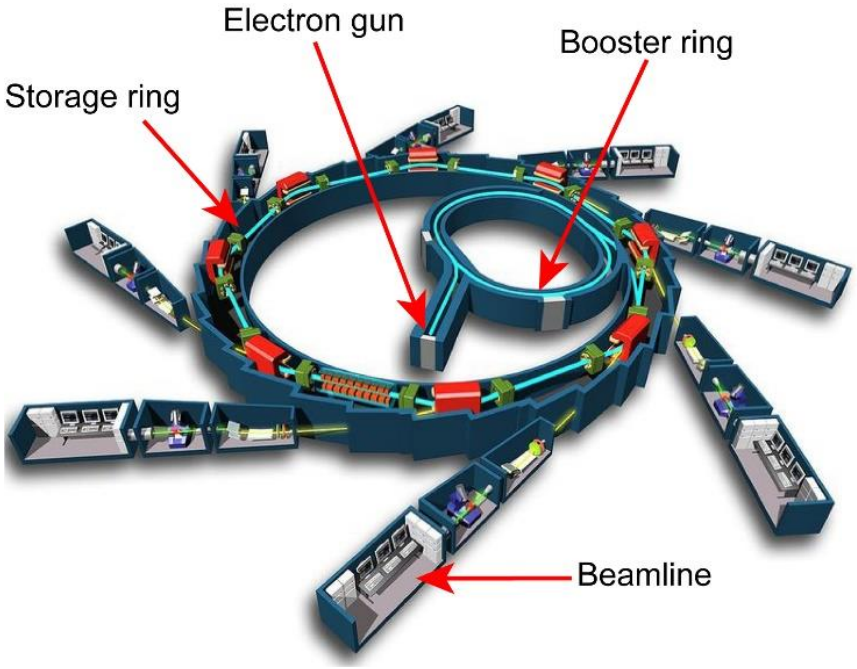

Figure 2.13: Diagram of SOLEIL synchrotron radiation facility in France. Source: https://www.synchrotron-soleil.fr/fr/recherche

Figure 2.14 shows the NAP-XPS at the TEMPO beamline, which is composed of several chambers, i.e. the load lock, the preparation chamber, the analysis chamber and the catalysis chamber (not shown in Figure 2.14). Especially, the analysis chamber is the gold coated mu-metal chamber which equipped with 7 lines inlets. Five lines are reserved for dosing gases, in which four for pure gases and one for mixed gases. The other two lines are used as dosing liquid like water for example. The sample stage is mounted on a vertical manipulator (the inset of Figure 2.14), which is mainly dedicated to catalysis reactions as the sample can be heated up to 1000 °C in the atmosphere of the reactive gases (the maximum working pressure 20 mbar) allowing to investigate the in situ catalytic reactions.

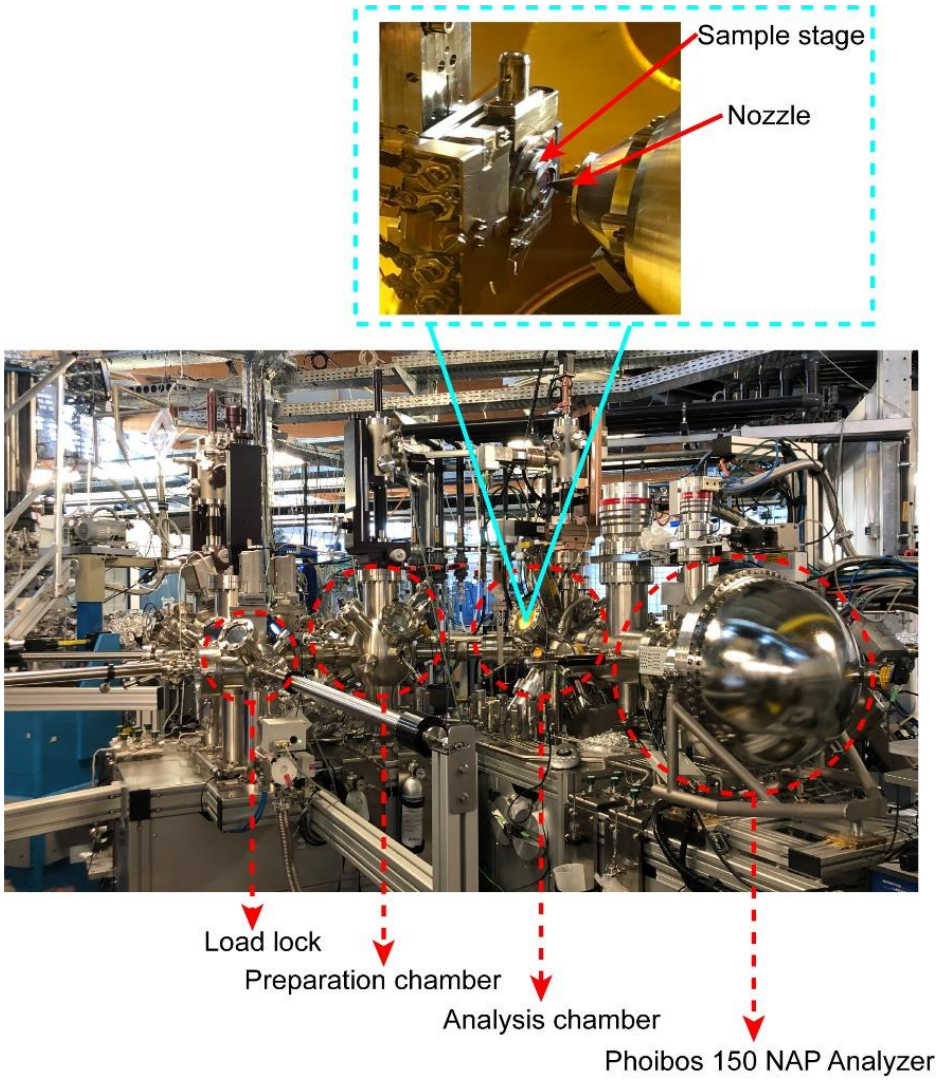

Figure 2.14: The NAP-XPS at the TEMPO beamline. Inset is the profile of the sample stage and the nozzle.

The analyzer of the NAP-XPS at the TEMPO beamline is the Phoibos 150 NAP energy hemispherical analyzer (Figure 2.15), which has four separate pressure stages separated by small apertures. The first pumping stage (hosting the wide-angle pre-lens) is separated from the analysis chamber by a conically-shaped nozzle pierced with a 0.3 mm diameter hole, which maximizes the differential pumping and brings the pressure in the first pumping stage down to $p_{ch}/10000$, where p_{ch} is the pressure in the analysis chamber. The second stage represents the front part of the electrostatic lenses of the PHOIBOS, separated by an iris aperture from the rear part, the third pumping stage. The fourth and final pumping stage at least work at a pressure of 10^{-7} mbar, which contain the true 180˚ hemispherical energy analyzer with 150 mm mean radius and the 3D delay line detector.

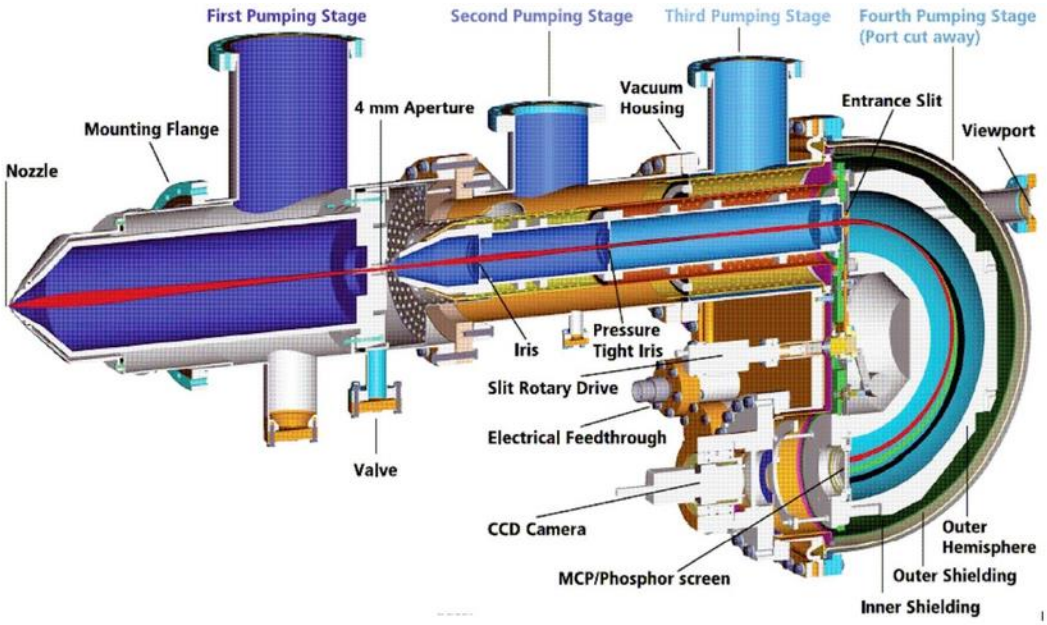

Figure 2.15: Diagram of the Phoibos NAP 150 analyzer. Source: http://www.specs.de/cms/upload/PDFs/SPECS_Prospekte/2010_11_PHOIBOS_150_NAP_product_brochure_final_web.pdf

For gas phase spectra, NAP-XPS probes the gas phase layers close to the sample surface within a volume of height approximately 0.12 mm considering the X-ray beam diameter of 0.1 mm and the sample normal/beam angle of 54°. The binding energy of the gas phase core-levels BE_{FL} (gas phase) measured from the Fermi level is used to track changes in the surface work function. The relationship between BE_{FL} (gas phase) and the ionization energy IE_{vac} (gas phase) measured from the vacuum level is:

$$BE_{FL}(gas\ phase) = IE_{vac}(gas\ phase) - \Phi \quad (32)$$

where Φ is the sample work function [18, 68]. Therefore, any change in ΔBE_{FL} (gas phase) will lead to a change in the work function ΔΦ equal to:

$$\Delta\Phi = -BE_{FL}(gas\ phase) \quad (33)$$

2.6 Quadrupole mass spectrometer (QMS)

The quadrupole mass spectrometer (QMS) is one type of mass analyzers in mass spectrometry, which consists of four cylindrical rods, parallel to each other [69], as shown in Figure 2.16 (a). In QMS the quadrupole is the mass analyzer, which is responsible for selecting ions depending on their mass-to-charge ratio (m/z). Ions can be selected in a quadrupole based on the stability of their trajectories in the oscillating electric fields applied to the rods. Only ions of a certain m/z ratio can reach the detector of the QMS for a given ratio of voltage, while

other ions having unstable trajectories will collide with the rods. At the TEMPO beamline in SOLEIL, since the aperture at the end of the nozzle cone is placed at a distance of 1.5 mm from the sample surface, the local gas in front of the sample is evacuated, which is then monitored by the QMS installed in the second stage of the differential pumping system, as shown in Figure 2.16 (b).

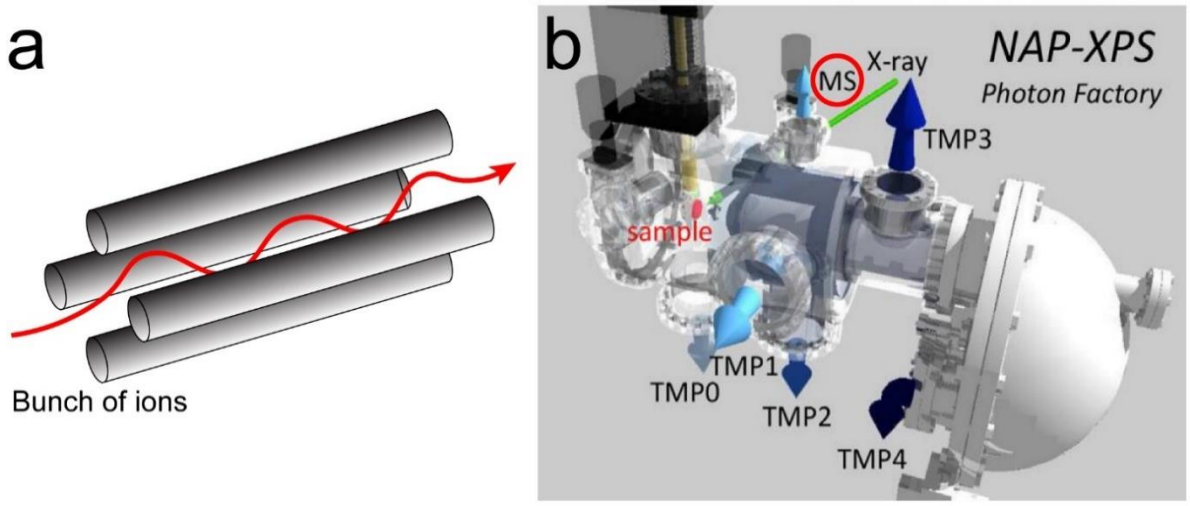

Figure 2.16: (a) Schematic of a quadrupole; (b) Illustration of the analysis chamber of NAP-XPS. MS indicates the mass spectrometer in the red circle [70].

Chapter 3: Fabrication of ZnO thin films on Pt(111)

The cleaning of the Pt(111) single crystal and the subsequent deposition of ZnO films on Pt(111) have been prepared in UHV. The structure and morphology of ZnO films on Pt(111) were studied by STM and LEED. In addition, the electronic properties of ZnO films were investigated using STS.

3.1 Preparation of the Pt(111) substrate

Platinum crystallizes in the face-centered cubic (fcc) structure with the lattice parameter $a = 3.92$ Å, as shown in Figure 3.1 (a). The close-packed plane of platinum is (111), which has the stacking order "a-b-c-a-b-c", as shown in Figure 3.1 (b). The lattice constant in Pt(111) is 2.78 Å and the distance between two nearest (111) planes is 2.26 Å.

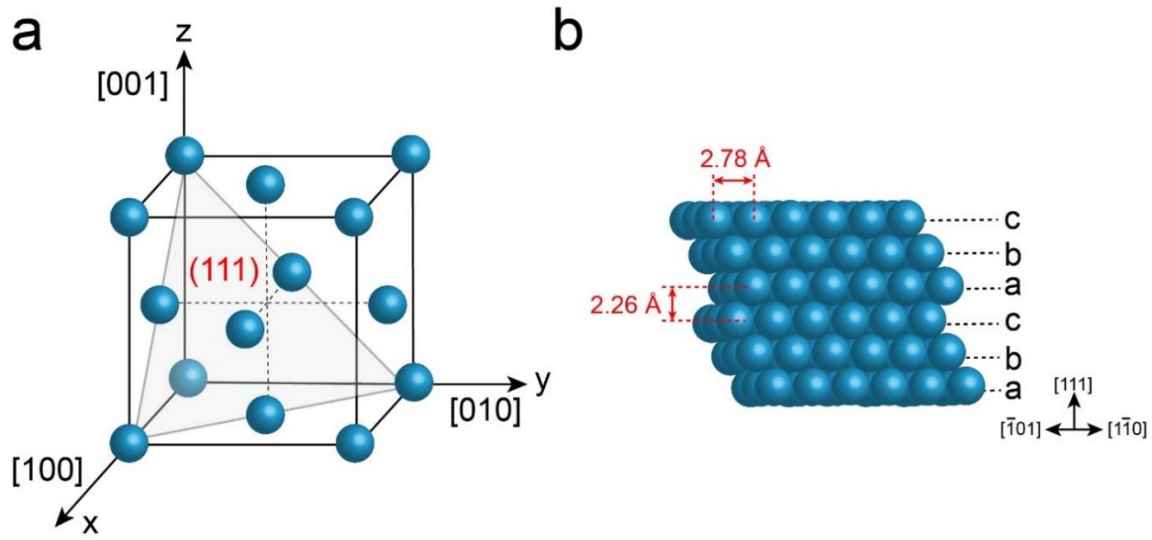

Figure 3.1: (a) Unit cell of the face-centered cubic Pt structure. The light gray triangle indicates the (111) plane; (b) Stacking order of Pt(111) planes.

The clean Pt(111) surface was obtained by cycles of Ar^+ sputtering and annealing at ~ 900 K in UHV. The subsequent annealing in the pressure of 10^{-7} mbar O_2 at ~ 1000 K was performed to remove residual carbon and then flashing to ~ 1200 K is to desorb residual O_2 from the surface. Figure 3.2 (a) shows the STM image of the clean Pt(111) surface, in which two terraces are separated by one step. The inset in Figure 3.2 (a) shows the atomic resolution STM image of the Pt(111) surface, in which the coordinates $[10\bar{1}]$ and $[1\bar{1}0]$ are defined by the fcc Pt structure. Figure 3.2 (b) shows the LEED pattern of the Pt(111) substrate, which displays a six-fold symmetry and a (1 × 1) periodicity. Moreover, the apparent height (Figure

3.2 (c)) along the turquoise line in Figure 3.2 (a) shows a monoatomic step with ~ 2.2 Å high, which is corresponding to the nearest distance between two layers of Pt(111) planes.

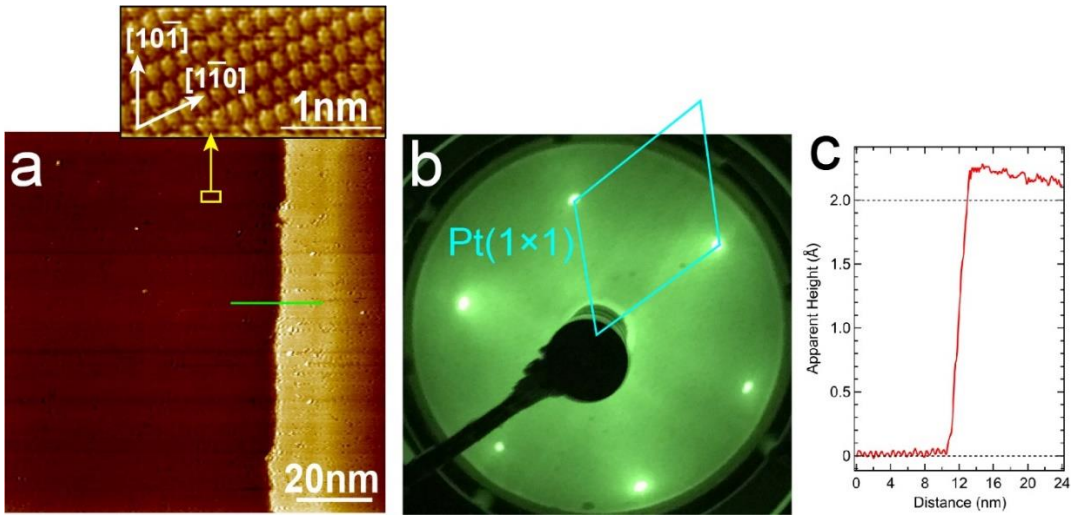

Figure 3.2: (a) STM image of the clean Pt(111) substrate (0.2 V, 500 pA). The inset is the atomic resolution STM image indicated in the yellow square (0.14 V, 270 pA); (b) LEED pattern of the Pt(111) substrate; (c) Apparent height of the Pt(111) terrace along the turquoise line in (a).

3.2 Preparation of ZnO films on Pt(111)

Zinc was deposited onto the clean Pt(111) surface by e-beam evaporation in the pressure of 10^{-7} mbar O_2 at room temperature in UHV, followed by oxidation at 600 K in 10^{-6} mbar of O_2 for ca. 20 min to achieve a better ordered ZnO film. The films are indicated as "as-deposited" in the following text. Also note that in the structural studies by STM, the thickness of the ZnO film is equivalent to the film coverage at the sub-monolayer regime and estimated from the deposition time when the film is more than one monolayer (ML).

Figure 3.3 (a)-(f) show STM images of the as-deposited ZnO films on Pt(111) as a function of film thickness. When the thickness is below 1 ML, the Pt(111) surface is randomly covered by irregular and flat ZnO islands, which gradually form large areas seen in Figure 3.3 (a)-(c). The apparent height (Figure 3.3 (g)) measured in Figure 3.3 (a) shows most of the ZnO islands are ~ 2 Å thick and few of them are ~ 4 Å thick, which means the islands coexist in monolayers and bilayers on Pt(111). Despite the bilayer ZnO islands are observed on Pt(111), the growth of ZnO films on Pt(111) follows a layer-by-layer mode. In addition, compared to the single step height of the bulk ZnO structure (~ 2.6 Å), the height of the ZnO monolayer is reduced to 2 Å, which suggests the ZnO film adopt a planar structure like the h-BN or graphene

structure, which is in agreement with the previous studies of ZnO on Pt(111) [31], Pd(111) [34], Ag(111) [42] and coinage metals [43, 71-73]. At 0.3 ML of the ZnO film, the Moiré structure can be recognized with a periodicity of ~ 17 Å (shown in the inset of Figure 3.3 (b)), which is due to the lattice mismatch between the in-plane lattice constant (3.25 Å) of the ZnO(0001) surface and the lattice constant (2.78 Å) of Pt(111) [34, 45]. This structure corresponds to 6 times the Pt(111) lattice constant or 5 times the ZnO(0001) lattice constant, which results in the (5×5) unit of ZnO grown on the (6×6) unit of Pt(111), forming ZnO(5×5)/Pt(111)-(6×6) superstructure, abbreviated to the (6×6) structure. Increasing the thickness to 0.53 ML, two types of the ZnO structures coexist on the Pt(111) surface. The minority phase is assigned to the compact (6×6) structure shown in Inset (i) of Figure 3.3 (c). The majority is the network structure exhibiting a honeycomb-like hexagonal unit cell (as seen in Inset (ii) of Figure 3.3 (c)) with a periodicity of ~ 11 Å, which corresponds to 4 times the lattice constant of Pt(111), resulting in the (4×4) structure for brevity. Based on the apparent height measurement (Figure 3.3 (h)) along the line scan in Figure 3.3 (c), the (4×4) structure exhibits one monolayer thick (~ 2 Å), which is the same as the (6×6) structure. However, the (4×4) structure has a relatively large surface roughness compared to the (6×6) structure. As the thickness reaches 1 ML, most of the Pt(111) surface is covered by ZnO, where the dark brown, medium brown and light brown areas correspond to the bare Pt(111), the monolayer ZnO and the bilayer ZnO. The white dots appearing on the monolayer ZnO is the Moiré structure (seen in the inset of Figure 3.3 (d)), which adopts the compact (6×6) structure. Continuing to increase the thickness to 1.8 ML, no bare Pt(111) can be observed, both the dark and light brown indicate the ZnO film, which shows the evident Moiré pattern exhibiting the (6×6) structure, as seen in the inset of Figure 3.3 (e). When the thickness is up to 4 ML, the triangular islands with various areas (from 7.8 nm^2 to 32.6 nm^2) are observed on the ZnO film, whose orientations are along the close-packed direction of Pt(111), i.e., $[\bar{1}\bar{1}0]$ and $[110]$, respectively (indicated in the yellow arrows in Figure 3.3 (e)). This type of surface belongs to the ZnO(0001)-Zn terminated bulk surface [30], which further proves the structural transition from the planar structure to the bulk wurtzite ZnO structure occurs ~ 4 ML [31, 42, 44, 74].

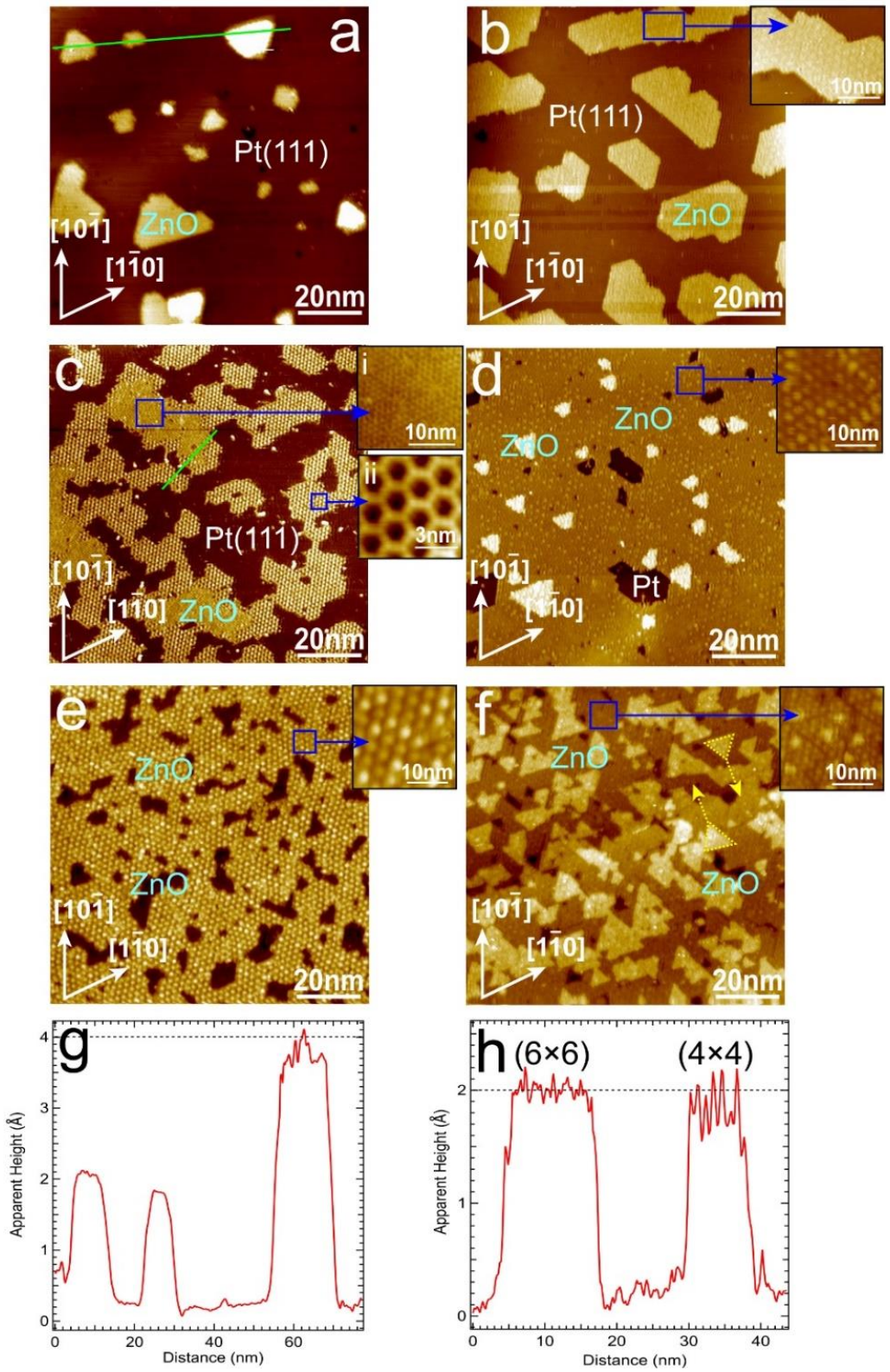

Figure 3.3: STM images of the as-deposited ZnO films on Pt(111) as a function of film thickness. (a) 0.15 ML (0.5 V, 150 pA); (b) 0.3 ML (2.6V, 700 pA); (c) 0.53 ML (0.5 V, 100 pA); (d) 1 ML (1.7 V, 270 pA); (e) 1.8 ML (2.6 V, 190 pA); (f) 4 ML (1.3 V, 700 pA). The Moiré structure is shown in the inset of each STM image marked by the blue rectangle. (g) and (h) are the apparent heights of ZnO films measured from the turquoise lines in (a) and (c).

Figure 3.4 shows the schematics of the (6×6) structure and the (4×4) structure, respectively. Note that the (4×4) structure only appears at the very low ZnO coverage (the sub-monolayer regime). DFT calculations of the cognate system, ZnO/Pd(111) [34], illustrate that the (4×4) structure is stabilized by H termination forming the $Zn_6(OH)_5$ -(4×4) structure, and the (6×6) structure could be also hydroxylated under the form of $Zn_6(OH)_6$. Further experiments [34, 45] shows H atoms do not mainly come from the residual gas during the film preparation in UHV, instead they are provided by the Pd(111) or Pt(111) surface due to the high affinity of the Pd(111) and Pt(111) surfaces towards hydrogen.

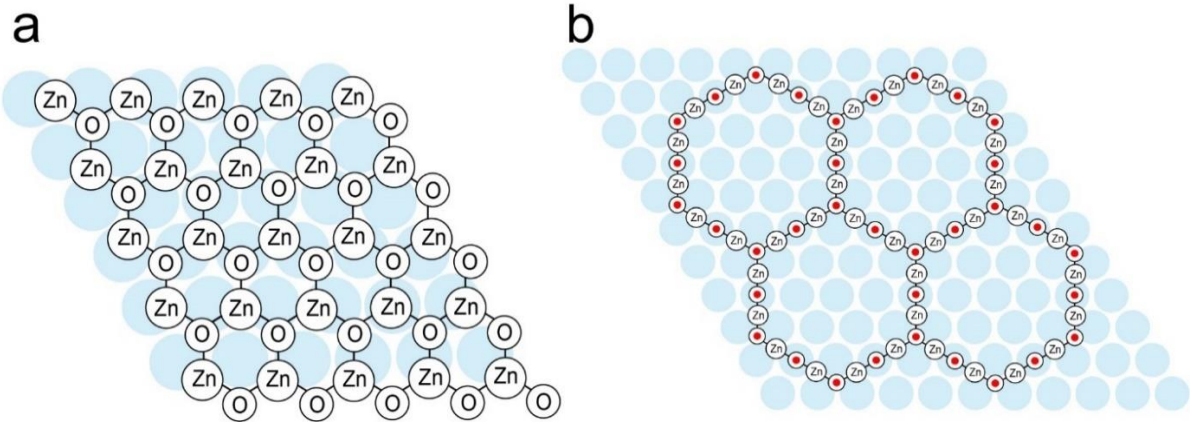

Figure 3.4: Schematics of (a) the (6×6) structure and (b) the (4×4) structure. Pt atoms are shown in light blue and H atoms are in red.

Figure 3.5 reveals the LEED patterns of the as-deposited ZnO films on Pt(111) as a function of film thickness. At 0.15 ML of the ZnO film, only one set of the LEED pattern appears attributed to the reciprocal lattice of Pt(111), which is reasonable due to the small amount of ZnO deposited on Pt(111). As the thickness reaches 0.3 ML, two sets of LEED patterns are recognized, in which the larger reciprocal lattice is assigned to Pt(111) and the smaller is attributed to the ZnO film. The epitaxial growth of the ZnO film on Pt(111) is verified as a result of the same direction of the two reciprocal lattice vectors. In addition, a set of satellite spots starts to appear which is caused by the coincident lattice formed at the interface between the ZnO film and the Pt(111) substrate [31]. These satellite spots agree well with the Moiré structure observed in the corresponding STM image shown in Figure 3.3. When the thickness is 0.53 ML, two sets of LEED patterns are also obtained, one is assigned to the (4×4) structure and the other is assigned to the (6×6) structure, in agreement with these two structures observed in the corresponding STM image. Increasing the thickness of the ZnO film from 1 ML to 4 ML, the reciprocal spot of ZnO turns out to be surrounded by the satellite spots. Moreover, the satellite spots gradually become attenuate as the film grows thicker, which is in line with the

layer-by-layer growth mechanism of the ZnO film on Pt(111), which is also observed in STM images shown above.

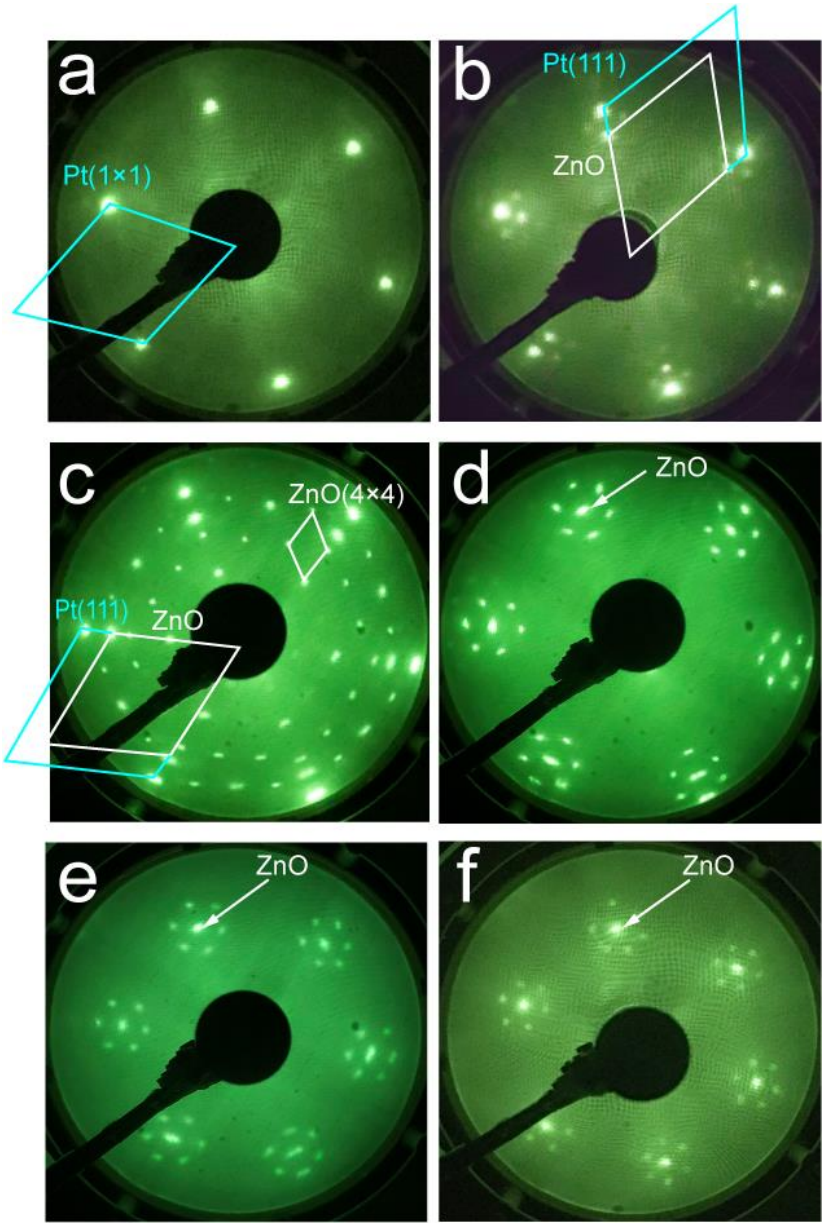

Figure 3.5: LEED patterns of the as-deposited ZnO films on Pt(111) as a function of film thickness. (a) 0.15 ML (electron energy 67 eV); (b) 0.3 ML (electron energy 66 eV); (c) 0.53 ML (electron energy 48 eV); (d) 1 ML (electron energy 45.3 eV); (e) 1.8 ML (electron energy 62 eV); (f) 4 ML (electron energy 69 eV).

3.3 Electronic properties of ZnO films on Pt(111)

The electronic properties of ZnO films on Pt(111) are investigated by STS at room temperature, as shown in Figure 3.6 (a). Increasing the ZnO thickness from the sub-monolayer (0.15 ML) to several layers (4 ML), the onset of the metallic behavior to the n-type

semiconducting behavior of the ZnO film is observed. Since the Pt(111) substrate serves as an electron reservoir to the ZnO film and provides electrons to the ZnO surface within the tunneling length (< 1 nm), the availability of electrons at the external surface of ZnO causes a significant change in the local density of states (LDOS), as seen in the schematic of Figure 3.6 (a). Further measurements of the conductance dI/dV are obtained from the I-V curves, which is related to the LDOS at $E - E_F = eV_s$ [75, 76]. The band gap of the ZnO film near Fermi level starts to open at 1.8 ML, which is only 1.4 ± 0.02 eV, much smaller than 3.37 eV obtained from the bulk ZnO (seen in Figure 3.6 (b)).

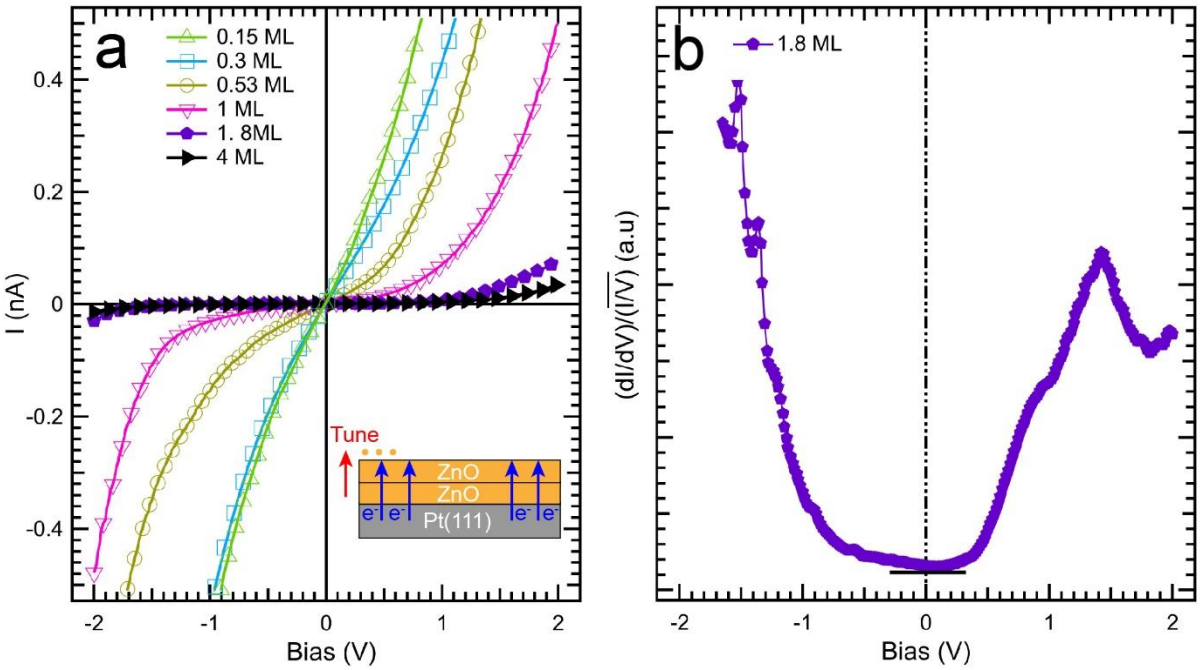

Figure 3.6: (a) Current-voltage (I-V) curves from different thickness of ZnO films on Pt(111) taken at room temperature in UHV. All curves plotted correspond to the average of at least 60 curves for each thickness of the ZnO film. The inset shows the schematic of electrons of Pt(111) transferring across ZnO films; (b) The normalized differential conductance calculated from the I-V curve of 2 ML in (a).

3.4 Summary and conclusions

The well-ordered ZnO thin films, from sub-monolayer up to several monolayers, were prepared in ultrahigh vacuum by electron beam evaporation on Pt (111). The structure and morphology of ZnO films on Pt (111) were studied by scanning tunneling microscopy (STM) and LEED. The ZnO islands, at low coverage, appear to be flat with a step height of 2.0 Å, corresponding to one monolayer (1ML) thick islands. The ZnO film grows seemingly in layer-

by-layer mode. When the ZnO film reaches multilayers, triangular islands are observed on the surface which is a characteristic of the ZnO (0001)-Zn-terminated surface. From high-resolution STM investigations, the Moiré structure on the surface were observed, which is assigned to a coincident lattice formed at the interface of ZnO and Pt (111). Particularly, at the low coverage of the ZnO film, the (4×4) structure appears as the majority phase along with the (6×6) structure, which forms the stoichiometry of $Zn_6(OH)_5$ -(4×4). The corresponding LEED pattern shows two sets of spots, one assigned to the (4×4) structure and the other attributed to the (6×6) structure. As the ZnO film grows thicker, the satellite spots begin to be gradually attenuated around the ZnO spots, which is in agreement with the layer-by-layer growth mode observed in the STM images. The current-voltage (I-V) measurements on the ZnO films were performed using scanning tunneling spectroscopy (STS) as a function of the ZnO film thickness. The electronic local density of states (LDOS) of ZnO exhibited a gradual transition from a metallic behavior to the n-type semiconducting behavior, illustrating the charge transfer from the Pt across the thin ZnO film.

Chapter 4: Morphology evolution of ZnO films on Pt(111) under CO oxidation conditions

The low temperature CO oxidation over ZnO films on Pt(111) has been performed under 1 mbar of the O_2: CO mixture in O_2 rich condition to circumvent the possible de-wetting and reduction of the oxide films. The evolution of the ZnO film morphology and structure as a function of the exposure temperature was characterized by STM and LEED ex situ. Specifically, three different thickness of the as-deposited ZnO films were studied in CO oxidation respectively, ranging from the sub-monolayer (0.53 ML), one monolayer (1 ML) to more than one monolayer (1.8 ML).

Figure 4.1 (a) shows the surface of the as-deposited ZnO film with the thickness of 0.53 ML at room temperature in UHV, which has been described in the previous chapter. After exposure to 1 mbar of the O_2: CO mixture (4:1) at room temperature for 1 hour and then pumping down to UHV, the surface of the same sample is shown in Figure 4.1 (b), in which the ZnO film shrinks from 0.53 ML to 0.45 ML. In addition, the rough disordered structure appears instead of the (6×6) structure while the (4×4) structure fairly seems intact. The line scan (seen in Figure 4.1 (h)) shows the nominal height of the (4×4) structure is still 2 Å and the nominal height of the disordered structure increases to 2.5 Å comparing with the height of the (6×6) structure (seen in Figure 4.1 (g)). The LEED pattern (Figure 4.1 (e)) shows that the spots related to the (6×6) structure become diffuse (indicated in the white dashed rectangle in Figure 4.1 (e)) while the spots relevant to the (4×4) structure can still be recognized, which is in agreement with the corresponding STM image. Further exposure to 1 mbar of the O_2: CO mixture (4:1) at 440 K for 1 hour, then pumping down to UHV and cooling to room temperature, the sample surface is shown in Figure 4.1 (c), where the ZnO film is partially de-wetted and the film coverage continues to reduce from 0.45 ML to 0.37 ML. Moreover, neither the (4×4) structure nor the disordered structure is observed on the surface. The line scan (Figure 4.1 (i)) shows the average height of the film rises to 2.5 Å, which is not very consistent with the work made by Martynova and colleagues [19], who found that after CO oxidation at 450 K the ZnO film transferred from one monolayer thick (2 Å) to bilayer thick (4 Å). The discrepancy compared to our result is probably due to the different tunneling conditions [77]. The LEED pattern (seen in Figure 4.1 (f)) just shows one set of spots attributed to the reciprocal lattice of Pt(111), which is corresponding to the dramatic decrease of the ZnO coverage after CO oxidation.

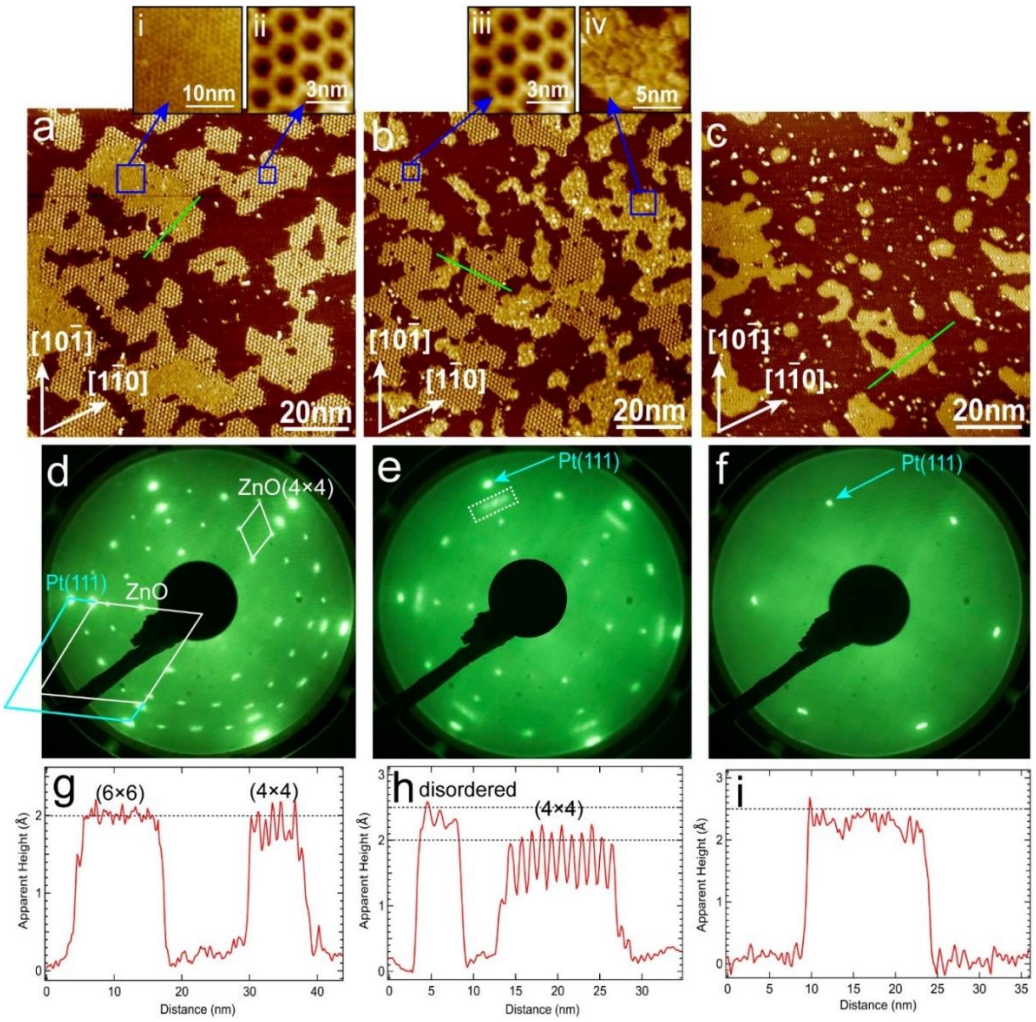

Figure 4.1: (a) STM image (0.5 V, 100 pA) of the as-deposited ZnO film on Pt(111). Inset (i) and (ii) are the (6×6) structure and the (4×4) structure marked by blue rectangles, respectively; (b) STM image (2.1 V, 100 pA) of the same sample as (a) but after exposure to 1 mbar of the O_2:CO mixture (4:1) at room temperature, followed by pumping down to UHV. Inset (iii) and (iv) are the (4×4) structure and the disordered structure marked by blue rectangles; (c) STM image (2.0 V, 100 pA) of the same sample as (b) but after a subsequent exposure to 1 mbar of the O_2:CO mixture (4:1) at 440 K, followed by pumping down to UHV and cooling to room temperature; (d) (electron energy 48 eV), (e) (electron energy 46 eV) and (f) (electron energy 63 eV) are the LEED patterns corresponding to (a), (b) and (c), respectively; (g), (h) and (i) are the line scans corresponding to the turquoise lines in (a), (b) and (c), respectively.

Figure 4.2 (a) shows the surface of the as-deposited ZnO film with the thickness of 1 ML at room temperature in UHV, whose structure has been described in the previous chapter. Most of the Pt(111) surface is covered by a ZnO monolayer film (89.5% of the whole surface) and a bilayer ZnO film (7% of the surface). The free Pt area is only 3.5% of the whole area. After exposure to 1 mbar of the O_2: CO mixture (4:1) at room temperature for 1 hour and then

pumping down to UHV, the surface of the same sample is shown in Figure 4.2 (b), in which the Pt area increases (17.5% of the whole surface) at the expense of the ZnO area. Not only does the ZnO film shrink, but also its morphology changes. The Moiré structure eliminates and leads to an apparent disorder comparing with that of the as-deposited ZnO film, which is in agreement with the faint satellite spots observed in the corresponding LEED pattern (shown in Figure 4.2 (e)). Interestingly, a "bulge" forms specifically at the Pt/ZnO boundary (seen in the line scan in Figure 4.2 (h)). The observed bulge can result either from the formation of a second ZnO sheet or from a chemical reaction at the Pt/ZnO boundary affecting the electron density or. The further statistics (shown in Figure 4.2 (i)) are made to compare the "peripheral bulge" heights (1.43 ± 0.23 Å) to those on "mono-to-bilayer" step heights, prior to the gas exposure (2.00 ± 0.04 Å). Another statistics (seen in Figure 4.2 (j)) are also made to show the width of the bulge is ~ 19 Å. In fact, this width is the only apparent extension due to the inertia of the tip during scanning (as shown in the schematic of Figure 4.2 (j)). An evidence of this effect is given by the lateral extension of the as-deposited ZnO edge, which shows the atomically abrupt "platinum-to-ZnO-monolayer" step of the pristine ZnO/Pt(111) surface is already ~ 15 Å (indicated in the schematic of Figure 4.2 (j)). Therefore, the hypothesis of a chemical reaction limited to the Pt/ZnO boundary coping with the STM data. Subsequent exposure to 1 mbar of the O_2: CO mixture (4:1) at 440 K for 1 hour, then pumping down to UHV and cooling to room temperature, the sample surface is shown in Figure 4.2 (c), in which the ZnO film becomes rough and de-wetted. In addition, the coverage of the ZnO film drops drastically to 67% of the whole surface compared to that of the as-deposited ZnO film (96% of the whole surface). The corresponding LEED pattern (Figure 4.2 (f)) just shows two sets of reciprocal lattices, the smaller one assigned to the ZnO film and the larger one attributed to Pt(111). No more satellite spots are observed in the LEED pattern due to the disordered interfacial lattice between the ZnO film and the Pt(111) substrate, which agrees well with the de-wetted ZnO film shown in Figure 4.2 (c).

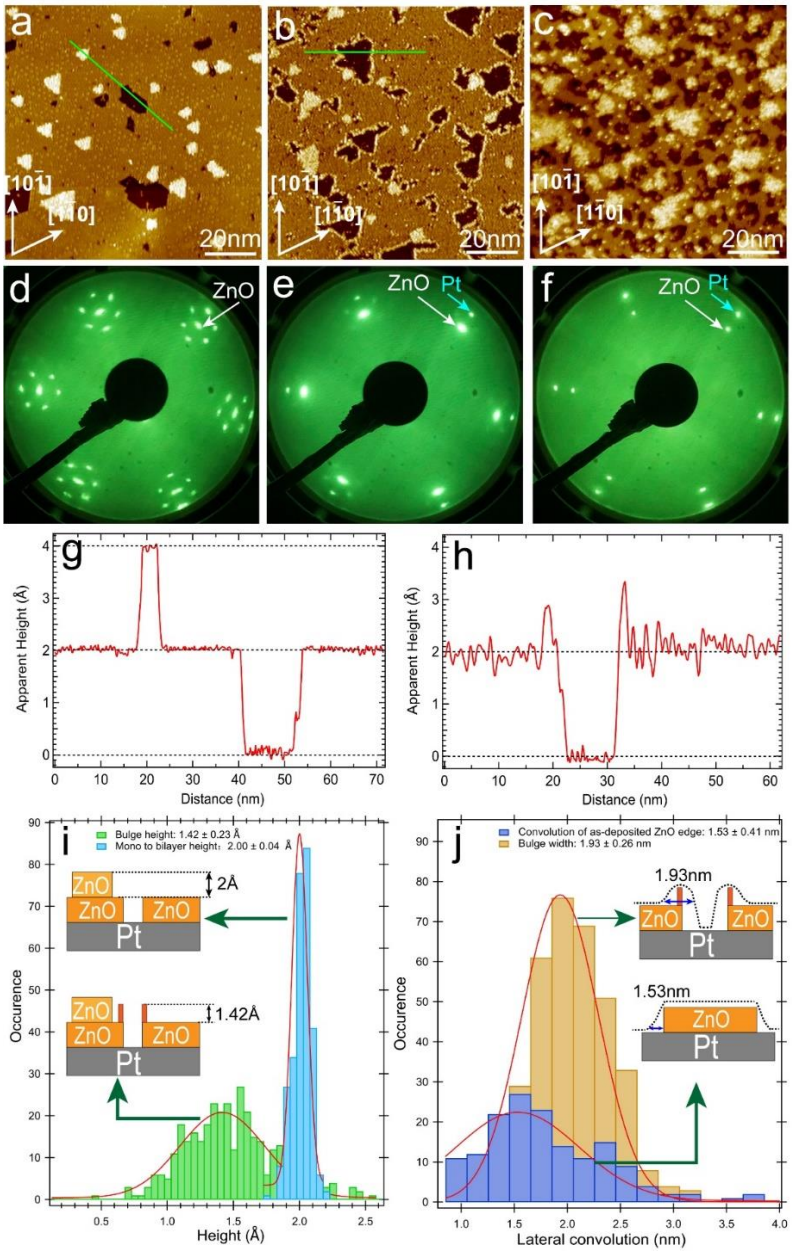

Figure 4.2: (a) STM image (1.7 V, 270 pA) of the as-deposited ZnO film on Pt(111); (b) STM image (1.3 V, 270 pA) of the same sample as (a) but after exposure to 1 mbar of the O_2:CO mixture (4:1) at room temperature, followed by pumping down to UHV; (c) STM image (0.6 V, 130 pA) of the same sample as (b) but after a subsequent exposure to 1 mbar of the O_2:CO mixture (4:1) at 440 K, followed by pumping down to UHV and cooling to room temperature; (d) (electron energy 45.3 eV), (e) (electron energy 47.8 eV) and (f) (electron energy 48 eV) are the LEED patterns corresponding to (a), (b) and (c), respectively; (g) and (h) are the line scans corresponding to the turquoise lines in (a) and (b), respectively; (i) Statistics on " peripheral bulge " heights (1.43 ± 0.23 Å) and those on " mono-to-bilayer" step heights, prior to gas exposure (2.00 ± 0.04 Å); (j) Statistics on the bulge width (~ 19 Å) and on the lateral extension of the as-deposited ZnO edge (~ 15 Å).

Figure 4.3 (a) shows the surface of the as-deposited ZnO film with the thickness of 1.8 ML at room temperature in UHV, which has been described in the previous chapter. After exposure to 1 mbar of the O_2: CO mixture (4:1) at room temperature for 1 hour and then pumping down to UHV, the surface of the same sample is shown in Figure 4.3 (b), in which the Moiré structure becomes less obvious comparing with that of the as-deposited ZnO film. This is in agreement with the much lower visibility of the satellite spots in the corresponding LEED pattern (seen in Figure 4.3 (e)). Further exposure to 1 mbar of the O_2: CO mixture (4:1) at 440 K for 1 hour, then pumping down to UHV and cooling to room temperature, the sample surface is shown in Figure 4.3 (c), where the ZnO film still seems intact but appears rough with some white adsorbates atop. Figure 4.3 (f) shows the satellite spots completely disappear but only the ZnO and Pt(111) reciprocal spots exist in the LEED pattern. The coverage of the ZnO film almost keeps constant (~ 83% of the whole surface) from UHV to the gas exposure at room temperature and 440 K, which suggests the ZnO film at 1.8 ML somehow behaves inert when exposed under the O_2: CO mixture, comparing with 0.53 ML and 1 ML of the ZnO films mentioned above. Therefore, the Pt/ZnO boundaries are suggested to be crucial to the reactivity of CO oxidation over the ZnO/Pt(111) system, which are also confirms by other works [78-80].

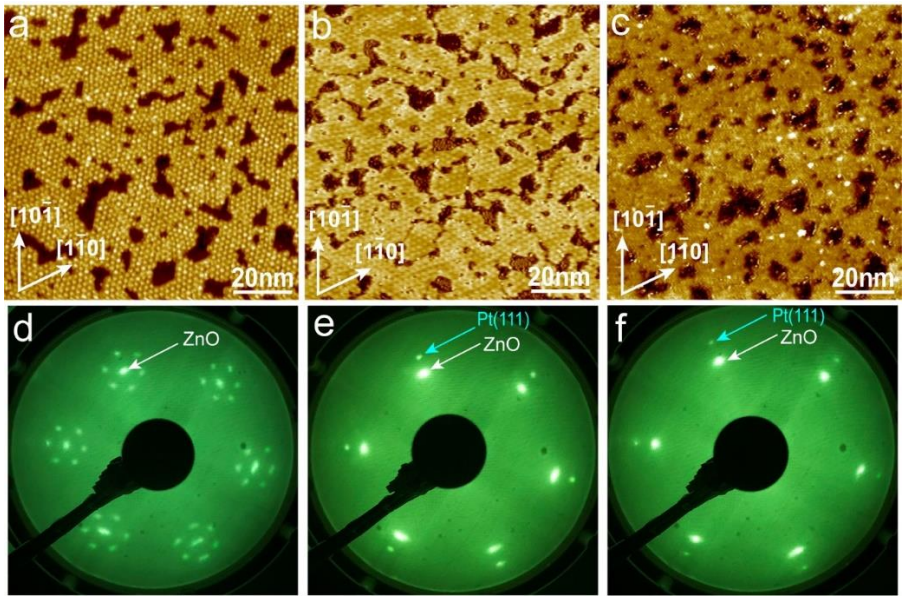

Figure 4.3: (a) STM image (2.6 V, 190 pA) of the as-deposited ZnO film on Pt(111); (b) STM image (2.4 V, 190 pA) of the same sample as (a) but after exposure to 1 mbar of the O_2:CO mixture (4:1) at room temperature, followed by pumping down to UHV; (c) STM image (0.8 V, 100 pA) of the same sample as (b) but after a subsequent exposure to 1 mbar of the O_2:CO mixture (4:1) at 440 K, followed by pumping down to UHV and cooling to room temperature; (d) (electron energy 62 eV), (e) (electron energy 61.8 eV) and (f) (electron energy 66.8 eV) are the LEED patterns corresponding to (a), (b) and (c), respectively.

Summary and conclusions

The morphology evolution of ZnO films on Pt(111) under CO oxidation reaction conditions were studied after exposure to the O_2:CO mixture at room temperature and 440 K. Specially, three representative thickness of as-deposited ZnO films were investigated, i.e. the sub-monolayer thickness (0.53 ML), the one-monolayer thickness (1 ML) and the quasi two-monolayer thickness (1.8 ML). It is found that the well-ordered surface structures of the films gradually vanish after gas exposure at room temperature, and de-wetted after the subsequent exposure at 440 K, which are in line with the corresponding LEED patterns at room temperature and at 440 K. Exceptionally, the (4 × 4) structure has no change compared to the (6 × 6) structure at 0.53 ML of the ZnO film after exposure at room temperature. Moreover, the film coverage at the sub-monolayer and one monolayer thick decreases after exposure at room temperature and finally de-wetted after exposure at 440 K, while the film coverage at the quasi two-monolayer thick, almost stays intact through the whole process of the gas exposure, which suggests the crucial role of the Pt/ZnO boundaries for the low-temperature CO oxidation reaction.

Chapter 5: CO oxidation mechanisms at the ZnO/Pt(111) model catalyst

The catalytic role of the inverse ZnO nano-islands on Pt(111) in the low-temperature CO oxidation was studied by near ambient pressure X-ray photoemission (NAP-XPS) in operando conditions. To illustrate the special role played by the oxide/Pt boundaries, a systematic comparative study of the inverse ZnO/Pt(111) catalyst with the plain Pt(111) surface was undertaken. The CO oxidation experiments were carried out within a temperature range of 293-520 K and in an O_2 rich O_2:CO mixture (4:1), under a total pressure of 1 mbar. NAP-XPS provides a "synoptic view" of both the catalytic surface and the gas phase in the immediate vicinity of the surface, as the solid-state core-levels are, at least in the present case, well separated from those of the gas-phase reagents and products. Moreover, a quadrupole mass spectrometer (QMS), embedded in the NAP-XPS spectrometer, provides additional information on the gas phase composition in the vicinity of the surface, which can be cross-checked with gas phase XPS data.

5.1 NAP-XPS setup as a flow reactor

During the experiments, an O_2:CO mixture (4:1) is fed into the chamber with a CO molar fraction at the inlet f_{in}^{CO} equal to 0.2. The overall pressure is kept constant at p_{ch}~1 mbar by feeding the analysis chamber via a leak valve, to compensate the diminishing number of molecules due to the pumping through the analyzer nozzle and the beamline entrance and to the reaction $2CO + O_2 \rightarrow 2CO_2$ that diminishes the number of molecules. Therefore, the analysis chamber/NAP-XPS ensemble is considered as a special case of a flow reactor, where pumping is realized via the NAP-XPS nozzle and the beamline entrance. To limit the attenuation of the photoelectron signal by inelastic scattering in the gas phase [81], the nozzle is placed at distance d of 1.5 mm from the sample surface. Under a total pressure of 1 mbar, the molecule mean free path λ_m is ~0.05 mm, the gas flow regime is nearly attained, the Knudsen number λ_m/d being ~0.03 [81]. The molar flow rate F_{out} through a pinhole of area A can be calculated from the flow rate of a gas at choked conditions [81, 82]. Expressed in mol·s^{-1} F_{out} is:

$$F_{out} = \frac{A \times C_d \times p_{ch}}{\sqrt{MRT}} \gamma^{\frac{1}{2}} \left(\frac{2}{\gamma+1}\right)^{\frac{\gamma+1}{2\gamma-2}} \quad (34)$$

where C_d is the coefficient of discharge (~0.61 for an orifice plate), γ the adiabatic index (1.4 for the diatomics, and 1.28 for CO_2), R the gas constant and T the absolute temperature.

Therefore, at room temperature, under a pressure of 1 mbar, and for an aperture of 7.07×10^{-8} m^2 (the nozzle pinhole area), F_{out} is equal to 3.3×10^{-7}, 3.5×10^{-7} and 4.47×10^{-7} $mol\cdot s^{-1}$, for O_2 and CO and CO_2 respectively. As the capillary through which the X-ray beam is introduced has also a diameter of 0.3 mm, its contribution to the molar flow rate is equal to that of the nozzle. Therefore, for the inlet gas composition (80% O_2 and 20% CO) at room temperature the estimated total average molar flow rate F_{out} is 6.7×10^{-7} $mol\cdot s^{-1}$ (0.9 mL_n/min).

5.2 QMS molar fractions for the plain Pt(111) and the ZnO/Pt(111) surfaces

The QMS signal is converted into mbar by normalizing the CO and O_2 signal to the known initial partial pressures, and the CO_2 signal is scaled to match the observed conversion of CO. The CO partial pressure is corrected from the cracking pattern contribution of CO_2. Then the molar fractions of CO (f_{QMS}^{CO}), O_2 ($f_{QMS}^{O_2}$), and CO_2 ($f_{QMS}^{CO_2}$) are deduced from the calibrated QMS. Figure 5.1 (a) and (b) shows the time-dependence of the QMS molar fractions for the Pt(111) surface and the ZnO/Pt(111) surface. In Figure 5.1 (c) and (d), the QMS CO_2 molar fractions of both surfaces are given on a logarithmic y-scale to highlight the reaction starting at 410 K. The QMS molar fractions are sensitive to the successive temperature increases. The transients, which can last ~100 min, are followed by the steady states in each temperature stage. The response of the ZnO/Pt(111) surface is very similar to that of the reference Pt(111) surface. Three different regimes can be highlighted, which are the low temperature regime (Regime I, 410 K), the high temperature range (Regime III, from 485 K to 520 K), and in between, the intermediate regime (Regime II, from 445 to 465 K).

In Regime I (at 410 K), the steady-state values of the molar fraction $f_{QMS}^{CO_2}$ is 0.0074 for the Pt(111) surface (the corresponding CO_2 partial pressure in the QMS, $p_{QMS}^{CO_2} = 7\times10^{-3}$ mbar) and 0.011 for the ZnO/Pt(111) surface ($p_{QMS}^{CO_2} = 1\times10^{-2}$ mbar). The 30% deviation in the $p_{QMS}^{CO_2}$ signal is indicative that the ZnO/Pt(111) surface is more reactive than the Pt(111) surface at this temperature. Note that the very low partial pressure of CO_2 makes it undetectable in the gas phase O 1s spectra of the Pt(111) surface and the ZnO/Pt(111) surface, which are shown in Figure 5.2 and Figure 5.3.

In Regime II, the steady-state CO_2 partial pressure above the Pt(111) surface increases by about one order of magnitude with respect to Regime I (seen in Figure 5.1 (a)). When the

surface temperature is raised to 445 K, the molar fraction $f_{QMS}^{CO_2}$ reaches 0.072 ($p_{QMS}^{CO_2}$=0.07 mbar) for the Pt(111) surface after a long transient. Interestingly, when the surface temperature is raised to 465 K, a strong enhancement in $f_{QMS}^{CO_2}$ is not observed. Instead, the molar fraction $f_{QMS}^{CO_2}$ reaches a plateau at 0.09 ($p_{QMS}^{CO_2}$ is ~0.09 mbar). In the gas layer comprised between the surface and the NAP-XPS nozzle, CO_2 starts to accumulate, but CO is far from being fully depleted. Indeed, the steady-state values of f_{QMS}^{CO} at 445 K and 465 K, are 0.13 and 0.115, respectively, which is about half of the CO molar fraction in the gas mixture fed into the gas chamber ($f_{QMS}^{CO} = 0.2$). The same kind of observations for ZnO/Pt(111) is made, as shown in Figure 5.1 (b). The steady-state $f_{QMS}^{CO_2}$ (p_{QMS}^{CO}) values are 0.08 (0.12 mbar) and 0.09 (0.11 mbar) at 445 K and 465 K, respectively.

For both surfaces, Regime III is characterized by a complete depletion of CO above the sample surface after a transient of ~92 min for the Pt(111) surface and ~155 min for the ZnO/Pt(111) surface at 485 K. p_{QMS}^{CO} is not measurable after the due correction of the CO_2 contribution to mass 28, and absent from C 1s and O 1s NAP-XPS spectra, as seen in Figures 5.2 and Figure 5.3. When the steady state is reached in the final part of the 485 K heating stage, $f_{QMS}^{CO_2}$ is ~0.22 ($p_{QMS}^{CO_2}$ is ~0.22 mbar) for both surfaces and does not vary when the temperature increases to 520 K.

The QMS data lead to two main observations. Within Regime II (where the CO pressure is divided by a factor of 2 or so) or within Regime III (where the CO pressure is almost zero), changes in temperature, and thus in the activated surface reaction rate, have no effect on $f_{QMS}^{CO_2}$. Such observations suggest that a relationship between the intrinsic production rate of CO_2 (the turnover frequency) and the steady-state value of $f_{QMS}^{CO_2}$ measured at the sample surface is lost. Indeed, the reaction rate is equal to the product concentration divided by a transit (or residence time) in the flow regime only for perfectly mixed reactors (which is not the case here), and, of course, at low pressure in the free molecular regime [83]. Second, in Regime II and III no difference is seen in the steady-state values of $f_{QMS}^{CO_2}$ between the pure Pt(111) surface and the ZnO/Pt(111) surface. Especially at high temperature (Regime III), one should expect a higher reaction rate for Pt(111) than for ZnO/Pt(111), for which the surface is made of Pt and ZnO mesoscopic areas (the ZnO layer de-wets, as seen in Figure 4.2 of Chapter 4), the platinum patches being much more reactive (NAP-XPS shows that CO leaves the platinum patches, as seen in Figure 5.2 and Figure 5.3) than the ZnO ones. These two observations suggest that mass

transport limitation (MTL) is already effective in Regime II, leading to the partial CO depletion and CO_2 accumulation at the surface. In contrast, in Regime I (360 K), when $f_{QMS}^{CO_2}$ is one order of magnitude smaller than the partial pressures of the reagents, i.e. the boundary layer is not saturated, it is found that the steady-state value of $f_{QMS}^{CO_2}$ is different for both surfaces (higher for the ZnO/Pt(111) surface than for the Pt(111) surface), which is in line with the findings of Martynova and coworkers [19].

What is the spatial extent of the boundary layer? In our case, the gas phase is probed either by NAP-XPS in a volume of height 0.12 mm above the surface, or through the gas sampling by QMS through the analyzer nozzle, at 1.5 mm above the surface. The CO_2 molar fractions $f_{NAPXPS}^{CO_2}$ are calculated from the intensities of the gas phase XPS O 1s components of CO_2, of the $^2\Sigma$ and $^4\Sigma$ O_2 doublet, and of the CO, whose energy positions are indicated in Figures 5.2 (the Pt(111) surface) and Figure 5.3 (the ZnO/Pt(111) surface). The $f_{NAPXPS}^{CO_2}$ values are reported in Figures 5.1(a) and (b). The agreement between $f_{NAPXPS}^{CO_2}$ and $f_{QMS}^{CO_2}$ is qualitatively good, which means that CO-depleted (CO_2-accumulated) volume has an extension comparable or even greater than the surface-nozzle gap. The extension of the CO_2-rich "boundary layer" over a catalytic crystal surface is a question that has been addressed carefully by planar laser-induced fluorescence (PLIF) in several papers [84-86], including one in which the NAP-XPS geometry is reproduced [86]. In that work the boundary layers extension is a few mm, i.e. a value comparable to the sample-nozzle gap. However, in the present experiment the much smaller mass flow (one order of magnitude smaller than the total flow of 10 ml_n/min in Ref.[86]) and above all the much lower overall pressure (Helium is used in Ref.[86] to balance the overall pressure to 1 bar) should lead to much larger extensions of the boundary layer (in the limit of the very low pressures, the CO_2 boundary layers extends in the whole reaction vessel).

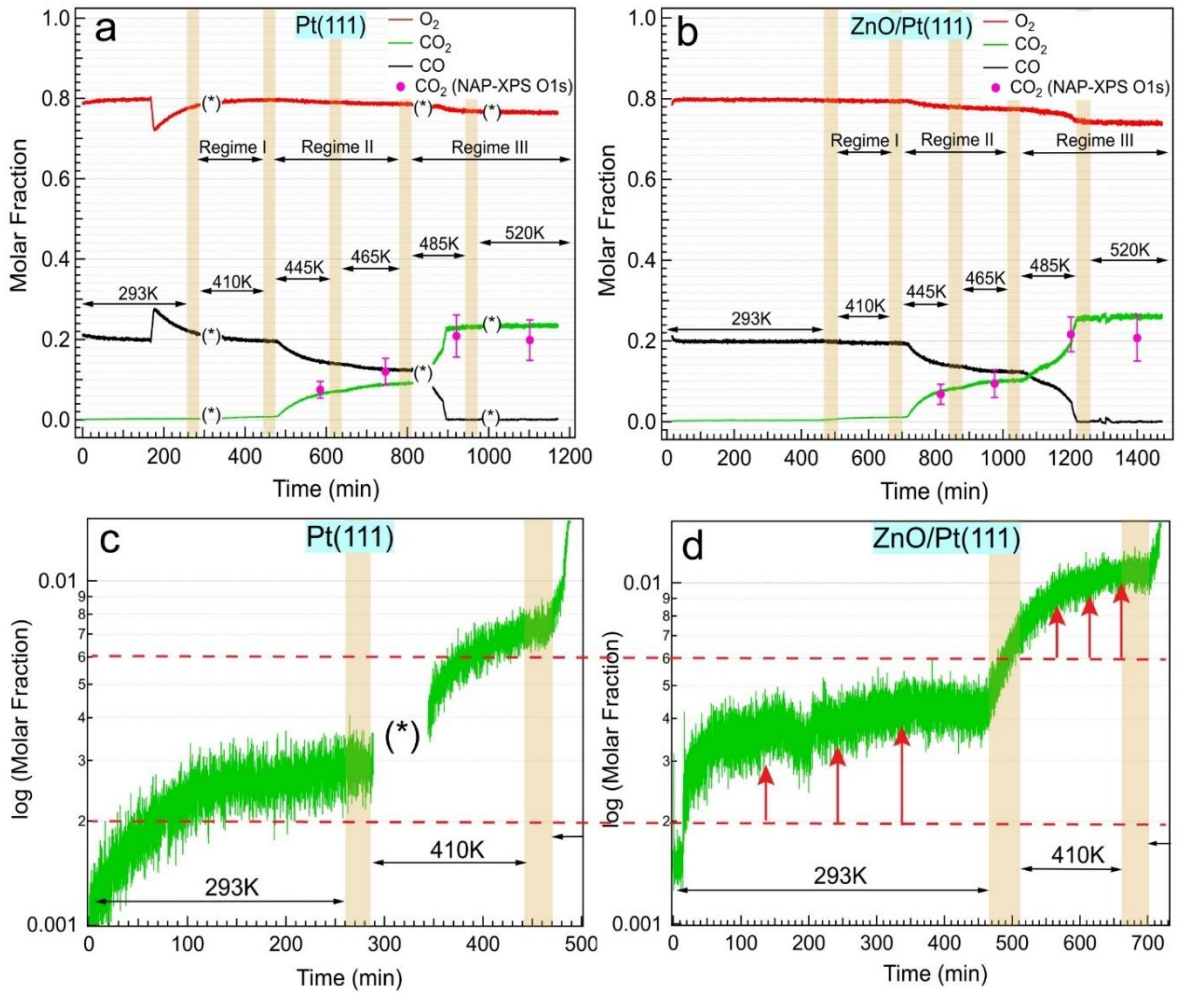

Figure 5.1: Time evolution of the QMS molar fractions (a) of CO (f_{QMS}^{CO}), O_2 ($f_{QMS}^{O_2}$) and CO_2 ($f_{QMS}^{CO_2}$) for the five heating steps (293 K, 410 K, 445 K, 465 K, 485 K and 520 K) for (a) the Pt(111) surface and (b) the ZnO/Pt(111) surface. Pink filled disks in (a) and (b) are CO_2 molar fractions $f_{NAPXPS}^{CO_2}$ deduced from gas phase O 1s spectra (Regime II and III); In panel (c) and (d) we compare the $f_{QMS}^{CO_2}$ values of Pt(111) and ZnO/Pt(111) at low temperature (y-logarithmic plot). The experiment is performed under a total pressure of 1 mbar. In panel (a) the deviation of the molar fractions from the nominal values observed at 293 K is due to a temporary malfunction of the flowmeter. (*) indicates the non-measurement of the QMS in panel (a) and (c).

5.3 CO oxidation reaction on the plain Pt(111) surface

First, the reference sample is considered, the bare platinum Pt(111) surface, whose corresponding C 1s, O 1s and Pt 4f spectra are given in Figure 5.2. The UHV C 1s XPS spectrum taken at room temperature after surface cleaning presents a graphitic contamination at a BE_{FL}

of ~284 eV, but no oxygen contamination is detected in the O 1s spectrum, and a clear surface component appears at 70.85 eV to the right of the bulk component (at 71.15 eV).

Once the 1 mbar CO:O_2 mixture is introduced at room temperature, two new C 1s components appear, one at a BE of 286.0 eV (attributed to the "bridge" adsorbed CO) and one at 286.6 eV (attributed to the "on-top" CO) [87]. The "on-top": "bridge" ratio is ~0.86. The appearance of these two adsorption geometries is corroborated by that of two components of the O 1s spectrum (as seen in Figure 5.2(b)) at 530.9 eV (bridge) and 532.5 eV (on-top) [87]. As observed by others [88], the on-top: bridge ratio of ~1.83 is different from that found from the C 1s spectra, but the discrepancy may be attributed to photoelectron diffraction effects. Note that in the O 1s spectrum, there is no measurable component attributable to the chemisorbed oxygen, which should give a distinctive peak at ~530 eV [89]. Thus, despite the exposure to a CO/O_2 mixture, only CO bonds to the surface at room temperature. This suggests that CO coverage is close to saturation, between 0.6 ML [87] and 0.68 ML [88]). The Pt 4f spectrum measured in surface sensitive conditions (the kinetic energy of 4f7/2 electrons ~94 eV) confirms the presence of a CO overlayer at room temperature, as the surface component has vanished, and two new peaks have appeared at the higher binding energies than the bulk metallic 4f7/2 peak, at 72.1 eV and 71.6 eV attributable to Pt making bonds with on-top and bridge CO, respectively [87].

As discussed before, CO_2 is detected by QMS in Regime I at 410 K, corresponding to $p_{QMS}^{CO_2}$ of ~7×10^{-3} mbar, but its component is not yet visible in the C 1s spectrum. The Pt(111) surface remains poisoned, as demonstrated by the observation of the adsorbed CO components in the C1s (Figure 5.2 (a)) and O 1s (Figure 5.2 (b)) spectra and of the Pt-CO bond components in the Pt 4f spectrum (Figure 5.2 (c)). To compare the intensity of the adsorbed CO at a high temperature (T) with that at room temperature (293 K), a calibration is proceeded as follows: First the XPS intensities of the adsorbed CO and the corresponding gas-phase CO are compared to each other. The adsorbed CO photoelectrons are emitted directly from the Pt(111) surface, while the gas-phase photoelectrons are emitted from a volume height of about 0.12 mm, a small value compared to the surface-nozzle gap 1.5 mm. The attenuation of the photoemission signal by inelastic energy losses in the gas phase is therefore considered to be practically identical for the surface signal and for that from the gas layer immediately above. Consequently, the XPS intensities of the adsorbed CO peaks is calibrated by dividing the XPS intensity of the CO gas phase ($\frac{I_{C\,1s\,NAPXPS}^{CO_{ads}}(T)}{I_{C\,1s\,NAPXPS}^{CO_{gas}}(T)}$), which then is divided by the corresponding CO partial pressure given by

QMS ($\frac{I_{C\ 1s\ NAPXPS}^{CO_{ads}}(T)}{I_{C\ 1s\ NAPXPS}^{CO_{gas}}(T)} \times p_{QMS}^{CO}(T)$), as the partial pressure of CO varies with the time and the temperature. Second, a normalized adsorbed CO intensity is then obtained after the calibrations, which is described as:

$$I_{Normalized} = \frac{R_{C\ 1s}^{CO}(T)}{R_{C\ 1s}^{CO}(293\ K)} = \frac{\left[\frac{I_{C\ 1s\ NAPXPS}^{CO_{ads}}(T)}{I_{C\ 1s\ NAPXPS}^{CO_{gas}}(T)} \times p_{QMS}^{CO}(T)\right]}{\left[\frac{I_{C\ 1s\ NAPXPS}^{CO_{ads}}(293K)}{I_{C\ 1s\ NAPXPS}^{CO_{gas}}(293K)} \times p_{QMS}^{CO}(293K)\right]} \quad (35)$$

After the normalization mentioned above, the normalized adsorbed CO intensities ($I_{Normalized}$) are shown in Figure 5.2 (d) and Table 5.1. At 410 K the normalized adsorbed CO intensity is 0.9, which indicates that the CO coverage now decreases to 90% of that at room temperature.

Temperature(K)	P_{QMS}^{CO} (mbar)	$I_{C\ 1s\ NAPXPS}^{CO_{gas}}$	$I_{C\ 1s\ NAPXPS}^{CO_{ads}}$	$I_{Normalized}$
293	0.25	1.20	6.81	1.00
410	0.22	1.09	6.53	0.90
445	0.16	1.00	7.26	0.80
465	0.13	0.80	6.86	0.74

Table 5.1: The normalized adsorbed CO intensities as a function of temperature.

As discussed before, in Regime II, at 465 K (as shown in Figure 5.1 (a)), $p_{QMS}^{CO_2}$ reaches a plateau at 0.09 mbar, greater by an order of magnitude than the CO_2 partial pressure in Regime I. CO is not fully depleted in the gas layers above the surface (p_{QMS}^{CO} is about an half of the CO pressure fed into the chamber) and is still found adsorbed on the surface (Figure 5.2 (a) and (b)). This view is corroborated by the analysis of the Pt 4f spectra (Figure 5.2 (c)), where the characteristic binding energy of the Pt-CO bonds are observed. The CO coverage (as seen in Figure 5.2 (d)) has diminished as it is now 74% of that found at room temperature. As the on-top: bridge ratio in the C 1s and O 1s spectra decreases to ~0.77 and ~1.29, respectively, with respect to that observed at room temperature, which is possible that the on-top sites are more depopulated than the bridge sites. Despite the surface loses the CO adsorbates, the O 1s component related to chemisorbed oxygen that should appear at ~530 eV [89] in Figure 5.2 (b) is yet undetectable. The C 1s (O 1s) BE_{FL}(gas phase) of CO and the O 1s BE_{FL}(gas phase) of $^2\Sigma$ ($^4\Sigma$) O_2 state remain rather constant between room temperature and 465 K, at 290.93 ± 0.3 eV and 539.56 eV (538.46 eV), respectively. Therefore, the partial desorption of the adsorbed

CO has a small impact on the work function. In fact, the work function change between the CO-covered surface (high coverage) and the clean one is extremely small (+15 meV) [90]. The O 1s spectrum and the work function variation do not advocate the formation of sizeable oxidized areas coexisting with CO-covered areas. Therefore, the first MTL regime is reached (with a partial pressure of CO equal to half the nominal pressure of CO fed into the chamber) while CO is the largely dominant surface species.

The situation is completely different in Regime III, which starts at the end of the 485 K stage (the O 1s spectrum displayed in Figure 5.2 (b) pertains to this steady state). Then, CO is fully depleted from the gas layers above the sample, as the CO_2 boundary layer has fully developed. Concomitantly, the components of the adsorbed CO have disappeared from the O 1s spectrum (Figure 5.2 (b)), while the adsorbed CO still exists in the C1s spectrum (Figure 5.2 (a)) due to the transient-state condition. Instead of the adsorbed CO, the O 1s component attributed to the chemisorbed atomic oxygen [87] appears at 530.1 eV. The latter behavior was also observed by authors using NAPXPS in the study of CO oxidation with the large O_2:CO ratio (9:1, under 0.15 mbar) [91]. Passing from Regime II to Regime III, a new interesting observation is that of a change in the gas-phase binding energies, which is the ΔBE_{FL}(gas phase) of -0.46 eV from O_2 in the O 1s spectra. Therefore, the replacement of a CO-covered surface by an O-covered one is accompanied by a positive increase (Equation (33) in Chapter 2) of the work function by $+0.5$ eV. This behavior is quite opposite that of the Pd(110) surface whose work function diminishes ($\Delta\Phi \approx -0.5$ eV) when the surface shifts from CO-covered to O-rich [92]. In the latter case a surface oxide develops at the surface. The present observation may be a useful piece of evidence in the ongoing debate about the presence of active platinum oxide phases on top of platinum surfaces [93].

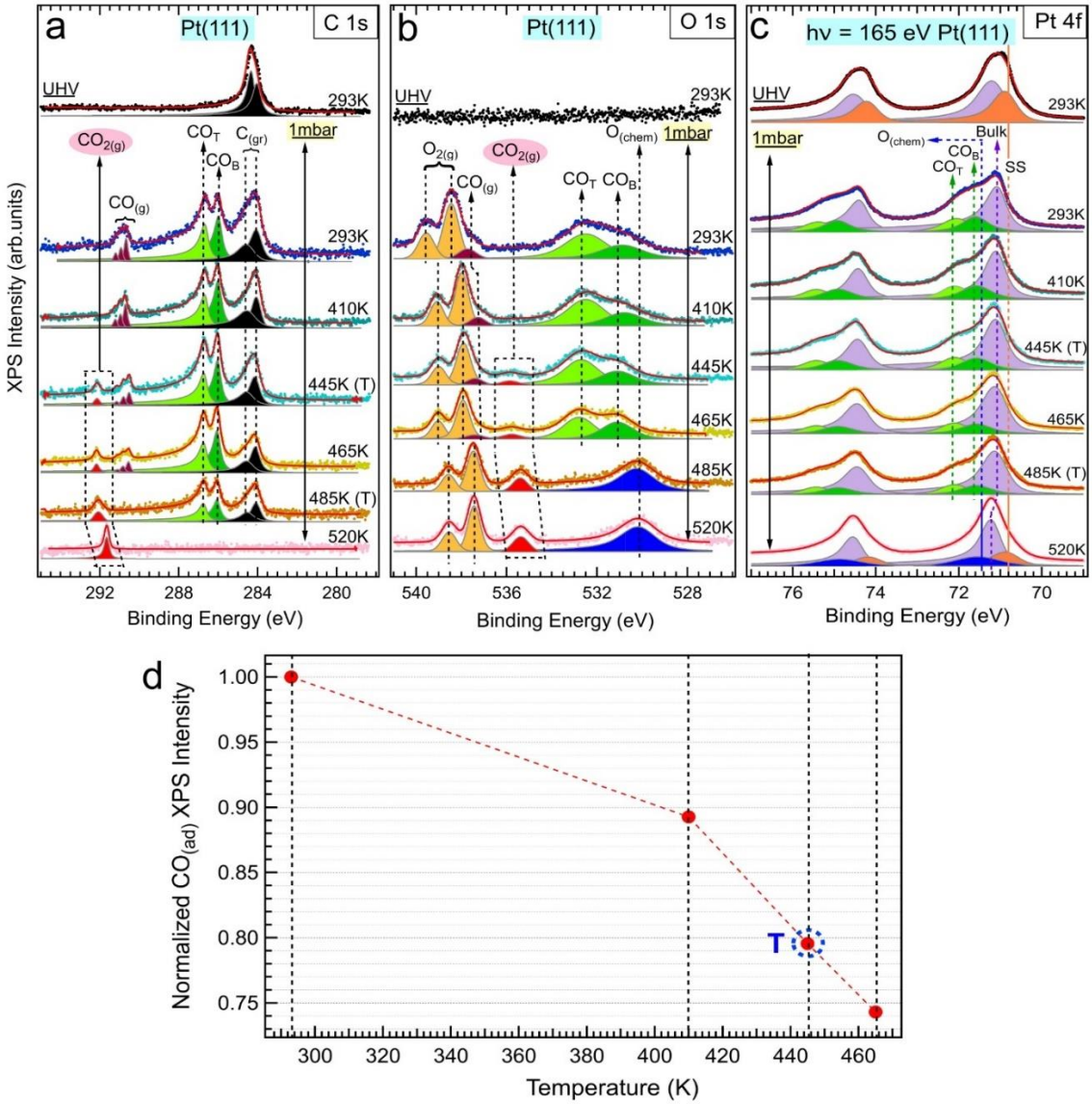

Figure 5.2: (a) C1s (hν = 400 eV), (b) O1s (hν = 635 eV) and (c) Pt 4f core-level spectra of the Pt(111) sample obtained as a function of the heating temperature. The temperature noted with (T) means the corresponding spectrum was acquired under the transient-state condition. The spectra labeled UHV were those of samples kept at room temperature, before any exposure to gases. The other spectra are recorded under a nominal pressure of 1 mbar, with an O_2: CO ratio of 4:1 (oxygen rich mixture). Gas-phase components are denoted by the "g" index, their positions are sensitive to changes in the surface work function. In C 1s, O 1s and Pt 4f spectra, the adsorbed CO exhibits two components, the bridge CO_B and on-top CO_T geometries. The component $C_{(gr)}$ and $O_{(chem)}$ are attributed to the graphitic carbon and the chemisorbed oxygen, respectively. The component Bulk and SS are assigned to the bulk Pt(111) and the surface state of Pt(111), respectively; (d) Normalized adsorbed CO intensities on Pt(111) as a function of the heating temperature. Note that at 445 K a steady state is not reached, indicated as the dash circle with T.

5.4 CO oxidation reaction on the ZnO/Pt(111) surface

As previously discussed, the CO_2 pressure plateaus on the bare Pt(111) and the ZnO covered Pt(111) are practically identical from a temperature of 445 K, as MTL, leading to CO depletion in the gas overlayers, determines the steady-states for both surfaces. However, in Regime I, at 410 K, the reactivity is low and MTL is not yet a limiting step. In this range the ZnO/Pt(111) is more reactive than the bare Pt(111) (the CO_2 partial pressure is ~30% higher). Therefore, in this context, an examination of the surface chemistry of the ZnO/Pt(111) is more interesting in this regime, as this point was not addressed in the previous work by Martynova and coworkers [19].

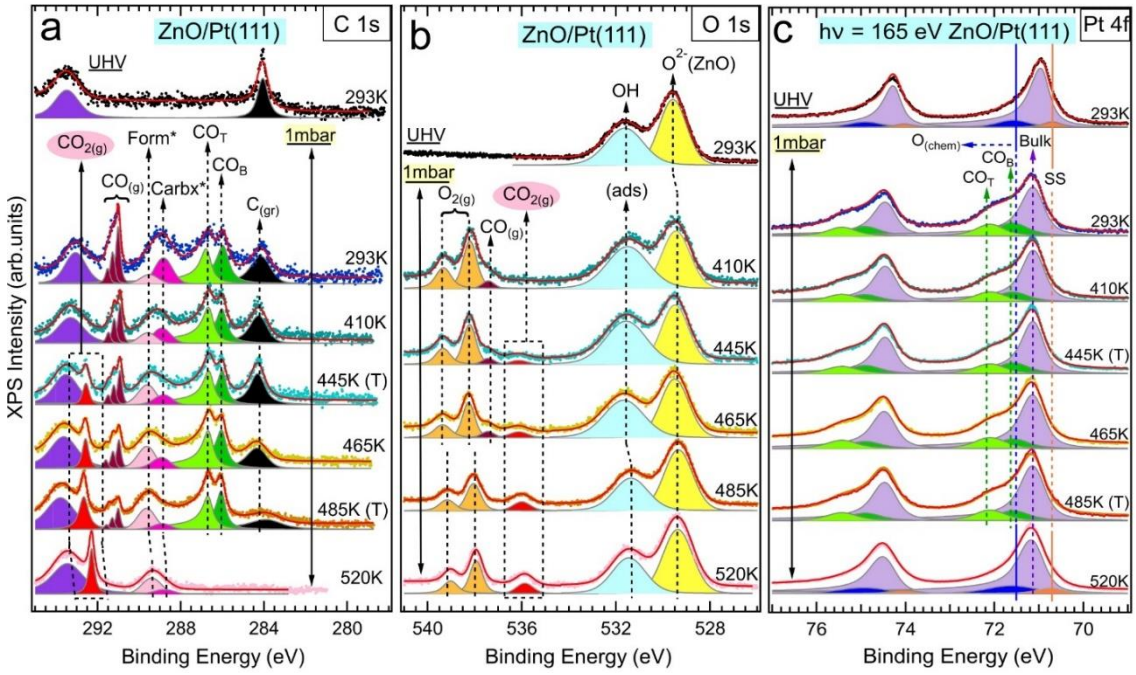

Figure 5.3: (a) C1s (hν = 400 eV), (b) O1s (hν = 635 eV) and (c) Pt 4f core-level spectra of the ZnO/Pt(111) sample obtained as a function of the heating temperature. The temperature noted with (T) means the corresponding spectrum was acquired under the transient-state condition. The spectra labeled UHV were those of samples kept at room temperature, before any exposure to gases. The other spectra are recorded under a nominal pressure of 1 mbar, with an O_2 :CO ratio of 4:1 (oxygen rich mixture). Compared to Figure 5.2, Form* and Carbx* are assigned to the formate and the carboxyl, respectively. The violet peak is due to K 2p photoelectrons. In the O 1s spectra, the O^{2-} and OH components are the oxygen components of ZnO and of its hydroxide, respectively. The components of the adsorbed CO, of the chemisorbed O on the platinum areas, of the formate and of the carboxyl are hidden in the O^{2-} and OH peaks.

At room temperature and in UHV conditions, the C 1s spectrum (Figure 5.3 (a)) of the as-deposited sample presents a graphitic contribution at ~284 eV, similar to the reference Pt(111) surface. Note also the presence of a K 2p component resulting from the ZnO deposition process, which is absent in the UHV spectrum of the reference plain Pt(111) surface (as shown in Figure 5.2 (a)). The corresponding O 1s spectrum (Figure 5.3 (b)) exhibits two components related to the zinc oxide layer. The one at the lower binding energy of 529.5 eV, matches that of O^{2-} in the bulk ZnO [94], which corresponds to 57% of the spectral weight. The second one (43% of the spectral weight), found at higher binding energy, 531.7 eV, is attributed to hydroxyls HO^{-} [29], stabilizing the ZnO layers. Indeed, Pt(111) [45, 95], like Pd(111) [34], is able to decompose residual H_2 or H_2O. While hydroxyls were previously detected by IRAS spectroscopy on this system [95], NAP-XPS has the advantage of quantifying their distribution.

When the gas mixture is introduced at room temperature, the C 1s spectrum (Figure 5.3 (a)) exhibits the two characteristic components of CO adsorbed on Pt(111) at the binding energies of 286.7 eV and 285.9 eV, corresponding to CO molecules adsorbed on on-top and bridge sites of Pt(111), respectively. The on-top: bridge distribution is 0.81, similar to the case of the reference Pt(111) surface at the same temperature (as seen in Figure 5.2 (a)). This indicates clearly that the ZnO is discontinuous and the patches of CO-covered Pt(111) surface coexist with the ZnO areas. Therefore, the coverage of the Pt areas on the ZnO/Pt(111) surface (θ_{Pt}) is defined as:

$$\theta_{Pt} = \frac{[R_{C\,1s}^{CO}(T)]_{ZnO/Pt(111)}}{[R_{C\,1s}^{CO}(T)]_{Pt(111)}} \tag{36}$$

where $[R_{C\,1s}^{CO}(T)]_{ZnO/Pt(111)}$ is the calibrated intensity of the adsorbed CO measured from the ZnO/Pt(111) surface, and $[R_{C\,1s}^{CO}(T)]_{Pt(111)}$ is that measured from the plain Pt(111) surface at the corresponding temperature. The calculation results of $R_{C\,1s}^{CO}(T)$ for the Pt(111) and the ZnO/Pt(111) surface are shown in Table 5.2.

Pt(111)

Temperature(K)	P_{QMS}^{CO} (mbar)	$I_{C\ 1s\ NAPXPS}^{CO_{gas}}$	$I_{C\ 1s\ NAPXPS}^{CO_{ads}}$	$R_{C\ 1s}^{CO}(T)$
293	0.25	1.20	6.81	1.44
410	0.22	1.09	6.53	1.29
445	0.16	1.00	7.26	1.15
465	0.13	0.80	6.86	1.07

ZnO/Pt(111)

Temperature(K)	P_{QMS}^{CO} (mbar)	$I_{C\ 1s\ NAPXPS}^{CO_{gas}}$	$I_{C\ 1s\ NAPXPS}^{CO_{ads}}$	$R_{C\ 1s}^{CO}(T)$
293	0.25	2.19	3.88	0.44
410	0.18	1.45	3.84	0.48
445	0.17	1.30	3.38	0.44
465	0.13	1.15	4.06	0.45

Table 5.2: The calibrated adsorbed CO intensities as a function of temperature for the plain Pt(111) surface and the ZnO/Pt(111) surface, respectively.

The fact CO adsorbs only on Pt, its coverage on the plain Pt(111) surface depending on the temperature (see above) is taken into consideration. Considering that, at each heating step, the CO surface density is the same on the pure Pt(111) and on the ZnO-free Pt(111) patches, this ratio can be assimilated to the fraction of the surface which is not covered by ZnO. θ_{Pt} is shown in Figure 5.4 (a). The platinum areas covered with CO make up 30% of the total surface at room temperature.

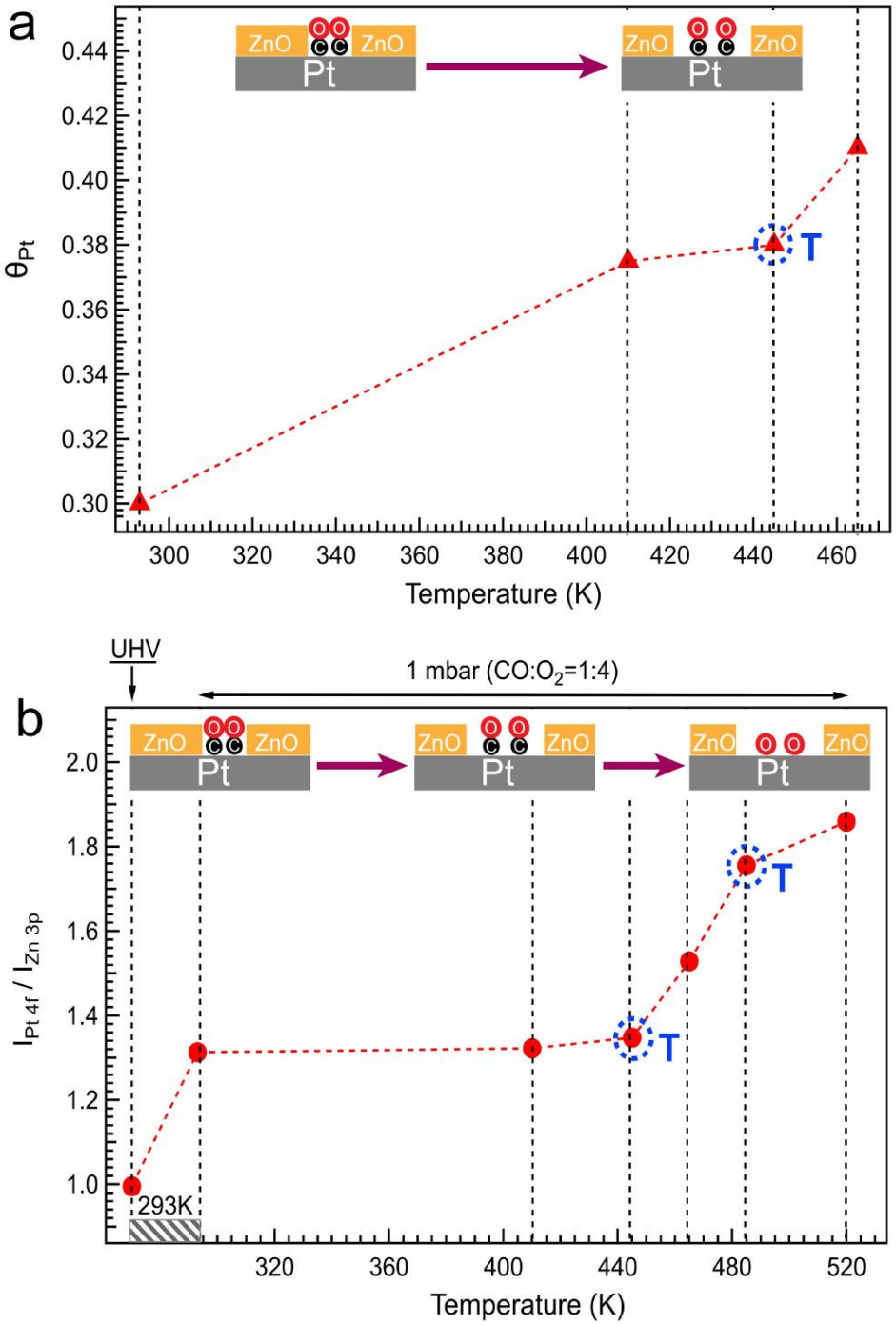

Figure 5.4: (a) Variation of the parameter θ_{Pt} measured for the ZnO/Pt(111) surface after exposure to 1mbar of the O_2:CO mixture (4:1) in the temperature range where CO is still adsorbed on Pt patches (steady-state conditions, except for 445 K; (b) The $I_{Pt\ 4f}/I_{Zn\ 3p}$ ratio obtained as a function of the temperature (from the Zn 3p and Pt 4f spectra measured at hν =165 eV, see Figure 5.5). The dash lines are only the guides for the eye.

The Pt 4f to Zn 3p intensity ratios ($I_{Pt\ 4f}/I_{Zn\ 3p}$), which are deduced from the Zn 3p and Pt 4f spectra presented in Figure 5.5, also gives the qualitative information on the surface fraction uncovered by ZnO, especially when CO titration is impossible in UHV. A variation in

the $I_{Pt\ 4f}/I_{Zn\ 3p}$ ratios sheds light on a rather unexpected event: ZnO de-wetting already occurs at room temperature upon exposure to CO and O_2. Even though the Pt 4f signal should be attenuated at the kinetic energy of ~94 eV by the adsorption of a layer of CO (Note that CO does not adsorbs on ZnO), the $I_{Pt\ 4f}/I_{Zn\ 3p}$ intensity increases after introduction of the gas mixture.

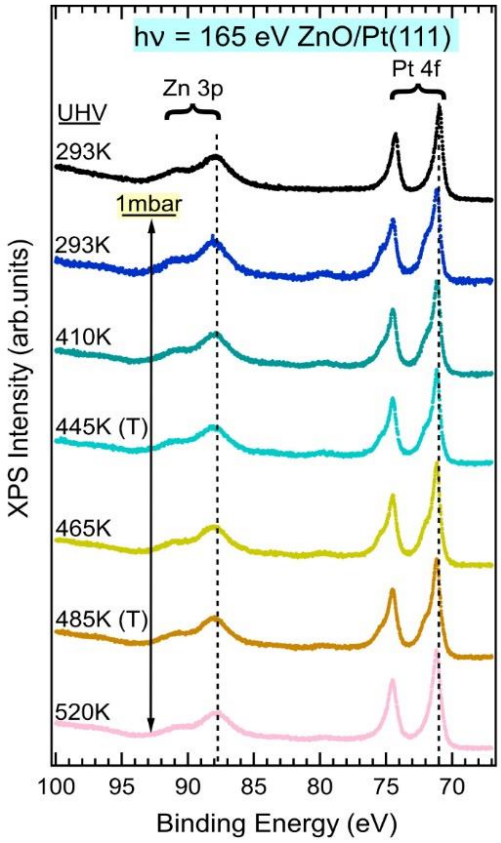

Figure 5.5: The Zn 3p and Pt 4f core-level spectra recorded at hν = 165 eV. The spectra labeled UHV were those of samples kept at room temperature, before any exposure to gases. The other spectra are recorded under a nominal pressure of 1 mbar, with an O_2: CO ratio of 4:1 (oxygen rich mixture).

The de-wetting of the ZnO film at room temperature after exposure to the gas mixture is also confirmed by the morphology changes in the STM images of the ZnO/Pt(111) surface, that were obtained in a separate UHV chamber, as shown in Figure 4.1 and Figure 4.2 in Chapter 4. Besides the de-wetting effect due to the exposure to the gas mixture at room temperature, the second noticeable observation provided by NAP-XPS is the appearance of a C 1s component peak at ~289.0 eV. Such a component is absent in the spectrum of the reference bare Pt(111) surface (Figure 5.2 (a)). Therefore, this component is attributed to an adsorbate sitting on the ZnO patches and/or at their periphery. The observed binding energy is too low for being attributed to that of a carbonate (290.4 eV [96] on the wurtzite ZnO), but falls within the range

of a carboxyl (OCOH), found at ~289 eV (on OH/Au(111) at 90 K [97]) or of a formate (HCOO), found at ~289.6 eV on the wurtzite ZnO [96, 98]. Carboxyls make strong bonds on Pt top sites (-2.44 eV according to DFT calculations [99] via the formation of a Pt-C bond), and therefore they should be expected at the ZnO/Pt boundary. Formates, which form on hydroxylated wurtzite surfaces [100] may also appear on the ZnO patches. They could also be present at the Pt/ZnO boundary, as the bond energy of the bidentate on platinum (2 Pt-O bonds) is similar to that of the carboxyl (−2.31 eV [99]). The C 1s spectrum (Figure 5.3 (a)) is in fact fitted with two components of the FWHM ~1 eV each, one positioned at ~289.0 eV (carboxyls) and one at ~289.6 eV (formates). At room temperature the carboxyl component dominates ~70% of the spectral weight.

It is conjectured that the appearance of the carboxyl/formate species results from the associative reaction of CO with hydroxyls provided by the ZnO patches (the issue of a reaction occurring on the ZnO patches or at the ZnO/Pt boundaries will be addressed further on). The ratio between the intensity of the carboxyl/formate species on ZnO and the intensity of the bridge and on-top CO on Pt(111) ($\frac{I_{C\ 1s\ NAPXPS}^{carboxyl/formate}(293\ K)}{I_{C\ 1s\ NAPXPS}^{CO_{ad}}(293\ K)}$) is ~0.67. Therefore, taking into account that the Pt fraction is ~ 0.3, and taking a (maximum) CO coverage of 0.68 ML on Pt(111) [88], the surface density of the carboxyl/formate species is $0.67 \times 0.3 \times 0.68$ ML on Pt(111), that is ~ 0.137 ML or 2×10^{14} atoms/cm^2 (1 ML Pt(111) is 1.5×10^{15} atoms/cm^2). Most importantly for the following discussion, the evolution of the carboxyl/formate surface coverage as a function of temperature is determined from its calibrated C 1s intensity, which is described as :

$$R_{C1s\ NAPXPS}^{carboxyl/formate}(T) = \frac{I_{C\ 1s\ NAPXPS}^{carboxyl/formate}(T)}{I_{C\ 1s\ NAPXPS}^{COgas}(T)} \times p_{QMS}^{CO}(T) \qquad (37)$$

The value of $R_{C1s}^{carboxyl/formate}$ does not change much (the variation is less than 17%) between room temperature and 485 K (a transient state). Its coverage at 520 K is unknown due to the lack of the gaseous signal, as shown in Table 5.3.

Temperature(K)	p_{QMS}^{CO}(mbar)	$I_{C\ 1s\ NAPXPS}^{CO_{gas}}$	$I_{C\ 1s\ NAPXPS}^{carboxyl\ /formate}$	$R_{C1s}^{carboxy\ l/formate}$
293	0.25	2.19	2.6	0.30
410	0.18	1.45	2.3	0.29
445	0.17	1.30	2.1	0.27
465	0.13	1.15	2.2	0.25
485	0.09	0.83	2.4	0.26

Table 5.3: The calibrated carboxyl/formate coverage as a function of temperature for the ZnO/Pt(111) surface.

In Regime I, at 410 K, the ZnO/Pt(111) surface is more reactive than the plain Pt(111) surface, as indicated by the QMS data in Figure 5.1 (c) and (d). The de-wetting of the ZnO layer has still increased with respect to room temperature, as now the platinum patches represent ~ 38% of the surface area, as seen in Figure 5.4 (a). The binding energy of the centroid of the carboxyl/formate species increases by ~0.2 eV with respect to the room temperature value, corresponding to an increase of the formate component at the expense of the carboxyl one (now 60% of the spectral weight). The solid phase O 1s spectrum encompasses several components relative to the (hydroxylated) oxide and the various adsorbates that may have overlapping binding energies: O^{2-} in ZnO (529.5 eV), bridge CO on Pt (531.0 eV), OH in ZnO (531.7 eV), on-top CO on Pt (532.5 eV) and the carboxyl/formate on ZnO (~533.0 eV [96]). Keeping the two components A (at ~529.5 eV, FWHM = 0.12 eV) and B (at ~531.7 eV, FWHM = 0.30 eV), that accounted for the O^{2-} (A) and OH (B) in UHV (prior to the exposure to the gas mixture), the B/A ratio (as shown in Figure 5.6) increases ~38% at 410 K in the presence of the gas mixture, compared to that in UHV. This is because of the appearance of the "CO+OH" (carboxyls/formates) at ZnO patches and of CO molecules on the Pt(111) areas.

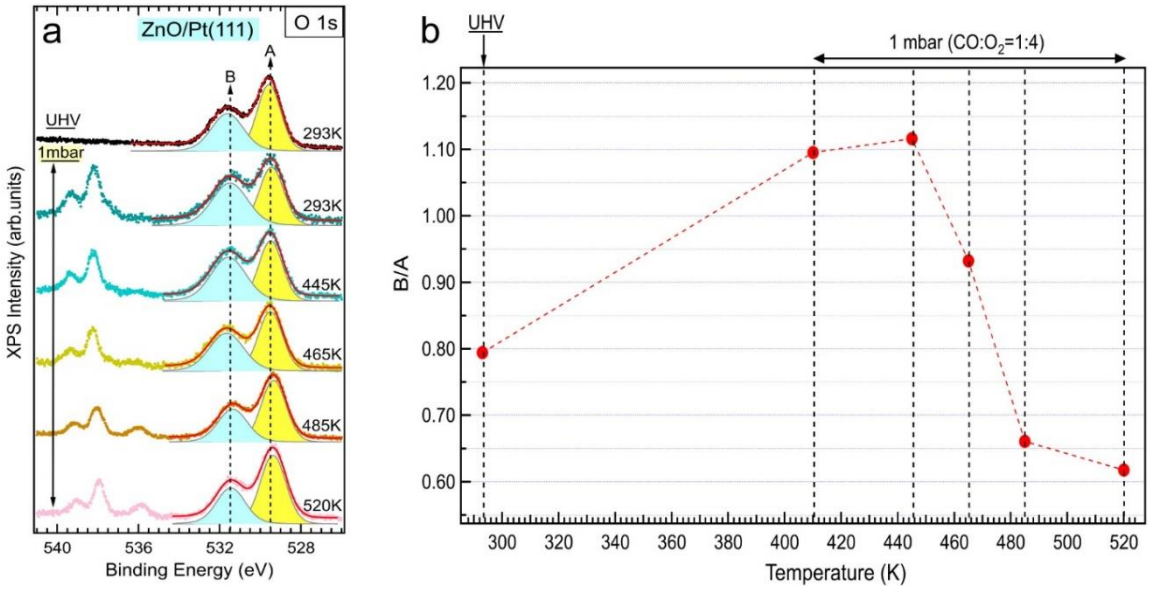

Figure 5.6: (a) O1s (hν = 635 eV) core-level spectra of the ZnO/Pt(111) sample obtained as a function of the heating temperature. Two components (one in cyan and the other in yellow) are indicated as A and B, respectively; (b) B/A ratios deduced from (a) as a function of temperature.

In regime II (up to 465 K), as in the case of the plain Pt(111) surface, there is an appreciable increase in the surface reactivity as CO starts to be depleted in the gas layers close to the surface. As CO is still adsorbed on the Pt patches (as shown in Figure 5.3 (a)), the de-wetting still increases as $\theta_{Pt} = 41\%$ (as seen in Figure 5.4 (a)). Despite the ZnO film coverage is about 60%, the measured partial pressure of CO (or of CO_2) is identical to that of the plain Pt(111) surface. Unless the intrinsic CO oxidation rates on the plain Pt(111) surface and on the ZnO/Pt(111) surface are coincidentally equal at this temperature, some scaling effect [84] of θ_{Pt} would be expected on the steady-state CO_2 partial pressures. Imagine for instance that the Pt is orders of magnitudes more reactive than the ZnO, then a lower partial CO_2 pressure would have been expected for the ZnO/Pt(111) surface than for the plain Pt(111) surface. However, this is not observed. The intricacy between the physics (transport) and the surface chemistry is already such that the intrinsic reaction rates cannot be determined for the both types of surfaces, although the CO partial pressure is not nullified, a generally admitted criterion is produced for mass transfer limitations (MTLs). Even though the intrinsic TOFs of the ZnO/Pt(111) surface and the plain Pt(111) surface cannot be compared in this regime, the NAP-XPS setup still provides invaluable data on the chemical state of the surface in operando conditions. Besides the ZnO de-wetting, a binding energy change in the "CO+OH" (OCOH/HCOO) species is observed at 445 K. Indeed, the corresponding C 1s binding energy centroid increases from 289.0 eV (room temperature) to 289.46 eV. This 0.46 eV binding energy shift is significant of a change in the bonding configuration. The formates are found to be the majority species (60%

of the spectral weight). This situation holds for the following higher temperatures (as seen in Figure 5.3 (a)). Therefore, the carboxyl is proposed to transform into the formates when the temperature is raised. Indeed, this process is certainly activated as the OH bond and the Pt-C bond must be broken. Note that the produced CO_2 does not transform ZnO film into $ZnCO_3$.

In Regime III (up to 520 K) the surface intrinsic reactivity is so high that the gaseous CO is fully depleted, similar to what is seen for the plain Pt(111) surface. However, the dramatic changes in the NAP-XPS spectra of the condensed phase concerning essentially the platinum patches. The C 1s spectrum (Figure 5.3 (a)) shows that all CO molecules have desorbed from the surface. The obvious remaining C 1s component is still peaked at 289.5 eV, and therefore the majority "CO+OH" species is the formates, the same as in Regime II. No carbonates are formed. The work function increases by about +0.4 eV (the ΔBE_{FL}(gas phase) is of -0.37 eV (CO_2 gas phase in the C 1s spectra) and -0.36 eV (O_2 gas phase in the O 1s spectra), which suggests that CO is replaced by the atomic oxygen on platinum patches, as it is the case for the Pt(111) reference. However, it is difficult to get a direct evidence of Pt-O bond formation as the corresponding O 1s component, positioned at ~530.0 eV (Figure 5.3 (a)), is hidden by the O^{2-} in the ZnO component (component A). The B/A ratio is now smaller than that in UHV (room temperature). This is essentially due to the desorption of CO and the formation of Pt-O bonds (as shown in Figure 5.6 (b)). In this oxygen rich conditions, and because of the extremely low CO partial pressure, OHs could be expected to be replaced by O^{2-} [95]. This is not observed in our conditions. Note that in UHV, hydroxyls on ZnO leave the surface at ~500 K for the monolayer (but at a higher temperature of ~700 K for the bilayer) [95].

5.5 Carboxyl/formate species, reaction intermediates or spectators?

While there are abundant experimental and theoretical literatures on the adsorption of small molecules" like CO and CO_2 on the wurtzite ZnO surfaces [29, 98, 101, 102], the surface chemistry of mono- and bi-layers of ZnO on Pt(111), not to mention that of the hydroxylated ZnO monolayer, has not been explored yet in great detail. In fact, the present NAP-XPS study sheds new light on the chemistry of discontinuous ZnO monolayer films on Pt(111). Two major experimental facts brought about by NAP-XPS are (i) the hydroxylation of the ZnO layer on Pt(111), and (ii) the associative reaction between CO molecules and hydroxyls provided by ZnO. In the following, we will discuss how ZnO-bound hydroxyls play a pivotal role in the first two phenomena. The role of OHs in the catalytic oxidation of CO on the ZnO/Pt(111) surface was not addressed in the preceding work (2013) by Martynova and coworkers [19], but the

observation that ZnO on Pt(111) is (partially) hydroxylated was made later on by the same group [45, 95]. A negative experiment concerning the ZnO/Ag(111) system points also to the role of hydroxyls: the ZnO/Ag(111) system is not more reactive than the bare noble metal [73]. In fact, Ag(111) does not share the capacity of Pt(111) and Pd(111) [34] to dissociate water (and H_2) from the residual, and then to hydroxylate the ZnO layers [95]. Because of the presence of hydroxyls attached to ZnO, it is not surprising that in the present case, the oxidation of CO by O_2 exhibits similarities with the water gas shift reaction, especially with regard to the "CO+OH" species, carboxyls and formates [17, 23, 97, 99, 103].

We believe that the "CO+OH" associative reaction observed by NAP-XPS, at the heart of the discussion on ZnO/Pt synergistic effects, occurs at the Pt/ZnO boundary, following the general screenplay [17, 104, 105] of inverse oxide/Pt model catalysts. First, the elimination of the moiré pattern in the STM images (as shown in Chapter 4) cannot be used as an evidence for the reaction of "inner" OHs, as the strain due to the peripheral reaction may impact the coincidence mesh. Second, as discussed before, the "bulge" seen in the STM images (Figure 4.2 in Chapter 4) at the Pt/ZnO boundary may be signature of reaction products building up there. Third, more importantly, the associative reaction should necessarily take place at the Pt/ZnO boundary, where both adsorbed CO (via a Pt-CO bond) and hydroxyls (bound to ZnO) can be found at short distances.

To support this hypothesis, we have estimated the amount of carboxyl/formate species that could be formed considering the Pt/ZnO boundary length per surface unit. For Pt patches representing 17.5% of the total surface (see the STM images in Figure 4.2 of Chapter 4), the boundary length per unit area is ~0.2 nm/nm^2 at room temperature after exposure to the gas mixture. The sample studied by NAP-XPS presents more developed Pt patches (~30% of the whole area), therefore the boundary length per unit area should be greater than that seen in the STM image of Figure 4.2(b). Considering the STM data provided by Martynova and coworkers [19], where the boundary length per unit area is plotted against the ZnO coverage, a value of ~0.3 nm/nm^2 is obtained. Taking the parameter of the wurtzite ZnO (0.325 nm), one obtains ~10^{14} O or Zn sites per cm^2. This value has the same order of magnitude as our estimate of the carboxyl/formate coverage (1.8 ×10^{14} cm^{-2}, from calibrated C 1s NAPXPS, as mentioned above), which remains roughly constant through the various temperature stages. Therefore, "CO+OH" species formed at the periphery of the ZnO patches can contribute to a large part of the species detected by NAP-XPS.

To understand the formation of the carboxyl/formate species, the description of the Pt/ZnO boundary must go down to the atomic level. We limit ourselves to the simple case of

the monolayer ZnO patches on Pt(111). If the "bulge" observed in STM does correspond to a two-layer thick boundary (although the apparent height is less, as shown in Figure 4.2 (i) of Chapter 4), the present modelling must be refined, but the general ideas exposed here are still valid. The monolayer ZnO "ribbon" depicted in Figure 5.7 exhibits two types of hydroxyl terminations, the S-type hydroxyl (bonded to one Zn ion) and the D-type one (bridging two Zn ions) on O-edges. The "inner" T-type hydroxyl (bonded to three Zn ions, the most highly coordinated of all OHs) is not considered for the reaction.

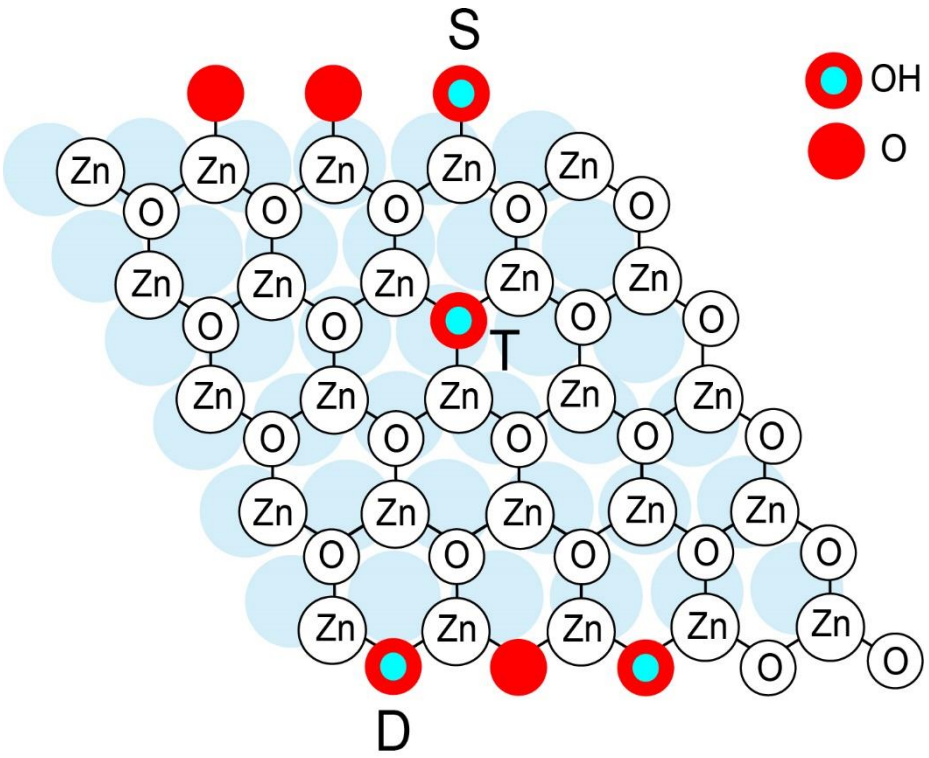

Figure 5.7: Scheme of the ZnO/Pt boundaries. On the top of the ribbon, the zinc edge presents undercoordinated Zn ions, zinc ions with O terminations resulting from the dissociation of an O_2 molecule, where S-type hydroxyls forms. The bottom part of the ribbon is terminated by an oxygen edge, where each oxygen (or D-type hydroxyl) is coordinated to two zinc atoms. The "inner" T-type hydroxyl is bonded to three Zn ions, which is the most highly coordinated of all OHs.

We do not consider in this discussion the direct reaction of a CO molecule with the D type hydroxyl (as seen in Figure 5.7), as it would lead to the formation of an O vacancy. We show the scheme of the possible reaction steps between CO and a S-type hydroxyl in Figure 5.8. The CO and the OH sit at short distance (Step 1). From the transition state (TS), a carboxyl is formed (step 2). An O_2 molecule dissociates (step 3) next to the carboxyl on two free Zn ions (this is the reaction on the coordinatively unsaturated metal cation combined to a nearby platinum atom, described theoretically by Sun and colleagues [48]), giving 2 Zn-O bonds (step

3). Then the H from the carboxyl can be transferred to one Zn-O to re-form a new S-type hydroxyl, and the CO_2 molecule desorbs (step 4). In that case, CO oxidation is co-catalyzed by the OHs, whose surface density is not depleted by the reaction. The inverse ZnO/Pt(111) model catalyst should present similarities with the FeO/Pt(111) system, in which hydroxyls act also as co-catalysts [106].

By increasing the temperature, the C 1s NAP-XPS (Figure 5.3 (a)) shows that the (CO+OH) associative species change their bonding configuration. On the basis of the simple geometric considerations and considering the bonding modes of the adsorbed CO on the Pt surface and the OH at the peripheries of the ZnO patches, the direct formation of a formate HCOO from CO and a S-type OH in a single elementary step seems impossible: in fact, CO binds through its C end to Pt, and thus, CO has to flip and change its orientation before the formate can be produced, as the latter one binds only through its two O atoms. Therefore, we propose that the reaction path leading to a formate species starts from the same TS as that of the carboxyl. However, instead of reaching a nearby O atom, the H atom jumps onto the C atom of the TS while the Pt-C bond is broken (step 2'). This leads to a bidentate formate. As there is no re-formation of a peripheral hydroxyl, the production of a formate would be a dead-end. Therefore, contrary to the carboxyl species which are the intermediary species in CO oxidation, we believe that the formate species that appear at high temperatures are simply spectators. Even in the water gas shift reaction on plain Pt(111) where water is fed in, formate species are considered as spectators [99].

It is clear that reaction paths envisioned here should be calculated to give a theoretical support to our proposition. However, it is clear that the model used in Ref. [48] (where a single TM oxide monolayer is considered) should be substantially improved, by taking into account the presence of OH and, possibly, the formation of a two-layer thick zinc oxide at the Pt/ZnO boundary.

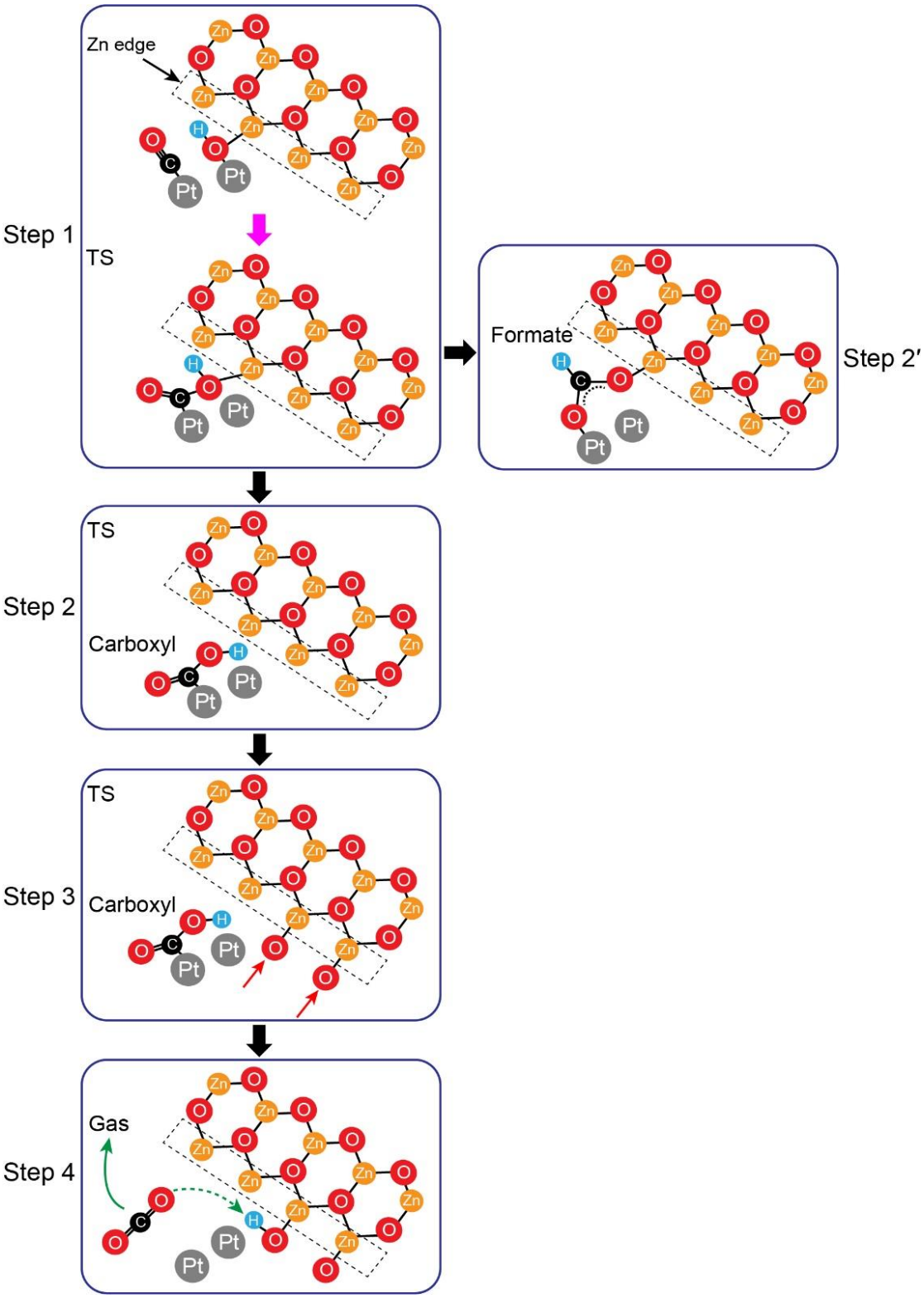

Figure 5.8: Scheme of the reaction steps. Associative reactions at a Zn-edge ZnO boundary between a CO molecule bound to Pt and an S-type hydroxyl leading to a carboxyl, then to CO_2 desorption (steps 1 to 4) with OH as a co-catalyst or leading to a formate (step 1 to 2').

5.6 Summary and conclusions

The oxidation of carbon monoxide over the inverse model catalyst ZnO/Pt(111), a discontinuous ZnO monolayer on Pt(111), was systematically compared to the same reaction over Pt(111), using principally NAP-XPS in operando conditions (O_2:CO mixture with a 4:1 ratio, under a pressure of 1 mbar), and, additionally STM in UHV. The NAP-XPS analysis chamber is a special case of a flow reactor, with a large volume of 35 L, and a small molar flow rate of 0.9 mL_n/min. Thanks to a mass spectrometer embedded in the NAP-XPS setup, we could compare the molar fractions of the reagents and products at a given temperature for both surfaces, and validate them by comparison with the gas-phase XPS data. It was possible to determine the conditions under which mass transfer limitation effects start to occur and affect the measurement of the reaction rates, an issue that is too often overlooked in the field of operando measurements. In particular, contrary to a widely accepted belief, our comparative study has shown that mass transfer limitation is seen at a rather early stage, before the CO reactant (the limiting species in the mixture) is fully depleted from the gas layers above the surface, and before CO is replaced by atomic O on Pt. As the present NAP-XPS setup design is one of the most popular worldwide, lessons drawn from the present experiments, especially the mass-transfer issue, have some generality and impact.

The general objective of the study was to characterize the surface chemistry of the inverse catalyst, especially in conditions where it appears more reactive than the plain Pt(111) surface. Via the measurement of the steady-state CO_2 molar fraction, a proxy of the reactivity, we observed that the reaction rate over the ZnO/Pt(111) system is superior to that over Pt(111) in a temperature range extending to 410 K. At higher temperatures (from 465 K), mass transfer limitation occurs on both surfaces, which makes the comparison of their intrinsic reactivity impossible. However, the crucial information on the surface chemistry in operando conditions can be collected at any temperature. This is the great advantage of NAP-XPS with respect to catalytic studies based solely on measurements of reagent/product concentrations in the gas phase.

In addition, the measurement of the gas-phase components in the NAP-XPS spectra, provides a straightforward procedure to calibrate the surface concentration of the various species adsorbed on the surface. The comparison with the plain Pt(111) surface is always fruitful. The CO titration method we used enabled us to follow the dynamics of the discontinuous ZnO monolayer film in the presence of the gas mixture, and more especially the extension of the Pt patches at the expense of the ZnO ones, even at room temperature. Given

that the surface concentration of CO on the plain Pt(111) surface is well known, estimates of the surface concentration of the surface reaction products between CO and ZnO could be also obtained.

Indeed, another benefit drawn from the comparison of the ZnO/Pt(111) system with the well-studied Pt(111) was the possibility to detect straightforwardly the adsorbed species common to both surfaces, i.e. CO on the Pt patches of ZnO/Pt(111), and those specific to ZnO/Pt(111), i.e. the species resulting from the "CO+OH" associative reaction (carboxyl and formates). The OH is provided by the ZnO that is heavily hydroxylated. An estimate of their surface concentration provided by NAP-XPS, and the determination of the ZnO film coverage, make that the "CO+OH" species are, in all likelihood, formed at the Pt/ZnO boundary during the exposure to the gas mixture. The carboxyl, the majority species present at low temperature (410 K), can be the intermediate species that leads to the evolution of CO_2, the ZnO-bound OH being the co-catalyst. However, the majority species observed at high temperature (from 445 K to 520 K) is a formate. We discuss why the formate should be essentially a spectator, and why the synergistic effects between the Pt and the (hydroxylated) ZnO can only be expected at the low temperature.

Chapter 6: Conclusion and perspectives

6.1 Conclusions

In this thesis, the research dedicated to the inverse ZnO/Pt(111) nanocatalysts has been investigated, which are relevant for the environmental remediation and energy generation systems (e.g. hydrogen fuel cells). Three parts have been involved in this research: (i) the design and fabrication of ZnO thin films on Pt(111), (ii) the structure evolution of ZnO films on Pt(111) under CO oxidation reaction conditions and (iii) the CO oxidation mechanism at the ZnO/Pt(111) catalyst under realistic conditions.

We first designed the fabrication of well-ordered ZnO thin films on Pt(111) using electron beam evaporation. The structure and morphology of ZnO films on Pt (111) were studied by scanning tunneling microscopy (STM) and LEED. The ZnO islands, at low coverage, appear to be flat with a step height of 2.0 Å, corresponding to one monolayer (1ML) thick islands. The ZnO film grows seemingly in layer-by-layer mode. When the ZnO film reaches multilayers, triangular islands are observed on the surface which is a characteristic of the ZnO (0001)-Zn-terminated surface. From high-resolution STM investigations, the Moiré structure on the surface were observed, which is assigned to a coincident lattice formed at the interface of ZnO and Pt (111). Particularly, at the low coverage of the ZnO film, the (4×4) structure appears as the majority phase along with the (6×6) structure, which forms the stoichiometry of $Zn_6(OH)_5$ -(4×4). The corresponding LEED pattern shows two sets of spots, one assigned to the (4×4) structure and the other attributed to the (6×6) structure. As the ZnO film grows thicker, the satellite spots begin to be gradually attenuated around the ZnO spots, which is in agreement with the layer-by-layer growth mode observed in the STM images. The current-voltage (I-V) measurements on the ZnO films were performed using scanning tunneling spectroscopy (STS) as a function of the ZnO film thickness. The electronic local density of states (LDOS) of ZnO exhibited a gradual transition from a metallic behavior to the n-type semiconducting behavior, illustrating the charge transfer from the Pt across the thin ZnO film.

Then we studied the structure evolution of ZnO films on Pt(111) after exposure to 1mbar of the O_2: CO (4:1) mixture. Specially, three representative thickness of as-deposited ZnO films were investigated, i.e. the sub-monolayer thickness (0.53 ML), the one-monolayer thickness (1 ML) and the quasi two-monolayer thickness (1.8 ML). It is found that the well-ordered surface structures of the films gradually vanish after gas exposure at room temperature, and de-wetted

after the subsequent exposure at 440 K, which are in line with the corresponding LEED patterns at room temperature and at 440 K. Exceptionally, the (4 × 4) structure has no change compared to the (6 × 6) structure at 0.53 ML of the ZnO film after exposure at room temperature. Moreover, the film coverage at the sub-monolayer and one monolayer thick decreases after exposure at room temperature and finally de-wetted after exposure at 440 K, while the film coverage at the quasi two-monolayer thick, almost stays intact through the whole process of the gas exposure, which suggests the crucial role of the Pt/ZnO boundaries for the low-temperature CO oxidation reaction.

Last but not least, we unveiled the CO oxidation mechanism at the inverse ZnO/Pt(111) catalyst. The CO oxidation over the inverse ZnO/Pt(111) catalyst, a discontinuous ZnO monolayer on Pt(111), was systematically compared to the same reaction over Pt(111), using principally NAP-XPS in operando conditions (O_2:CO mixture with a 4:1 ratio, under a pressure of 1 mbar). Thanks to a mass spectrometer embedded in the NAP-XPS setup, we could compare the molar fractions of the reagents and products at a given temperature for both surfaces and validated them by comparison with the gas-phase XPS data. It was possible to determine the conditions under which mass transfer limitation effects start to occur and affect the measurement of the reaction rates, an issue that is too often overlooked in the field of operando measurements. In particular, contrary to a widely accepted belief, our comparative study has shown that mass transfer limitation is seen at a rather early stage, before the CO reactant (the limiting species in the mixture) is fully depleted from the gas layers above the surface, and before CO is replaced by atomic O on Pt.

Via the measurement of the steady-state CO_2 molar fraction, a proxy of the reactivity, we observed that the reaction rate over the ZnO/Pt(111) system is superior to that over Pt(111) in a temperature range extending to 410 K. At higher temperatures (from 465 K), mass transfer limitation occurs on both surfaces, which makes the comparison of their intrinsic reactivity impossible. However, the crucial information on the surface chemistry in operando conditions can be collected at any temperature. This is the great advantage of NAP-XPS with respect to catalytic studies based solely on measurements of reagent/product concentrations in the gas phase.

The measurement of the gas-phase components in the NAP-XPS spectra, provides a straightforward procedure to calibrate the surface concentration of the various species adsorbed on the surface. The comparison with the plain Pt(111) surface is always fruitful. The CO titration method we used enabled us to follow the dynamics of the discontinuous ZnO monolayer film in the presence of the gas mixture, and more especially the extension of the Pt

patches at the expense of the ZnO ones, even at room temperature. Given that the surface concentration of CO on the plain Pt(111) surface is well known, estimates of the surface concentration of the surface reaction products between CO and ZnO could be also obtained.

Indeed, another benefit drawn from the comparison of the ZnO/Pt(111) system with the well-studied Pt(111) was the possibility to detect straightforwardly the adsorbed species common to both surfaces, i.e. CO on the Pt patches of ZnO/Pt(111), and those specific to ZnO/Pt(111), i.e. the species resulting from the "CO+OH" associative reaction (carboxyl and formates). The OH is provided by the ZnO that is heavily hydroxylated. An estimate of their surface concentration provided by NAP-XPS, and the determination of the ZnO film coverage, make that the "CO+OH" species are, in all likelihood, formed at the Pt/ZnO boundary during the exposure to the gas mixture. The carboxyl, the majority species present at low temperature (410 K), can be the intermediate species that leads to the evolution of CO_2, the ZnO-bound OH being the co-catalyst. However, the majority species observed at high temperature (from 445 K to 520 K) is a formate. We discussed why the formate should be essentially a spectator, and why the synergistic effects between the Pt and the (hydroxylated) ZnO could only be expected at the low temperature.

6.2 Perspectives

Based on the knowledge we gained from the ZnO/Pt(111) catalysts related to the low temperature CO oxidation, at present we plan to study the growth and reactivity of ZnO nanostructures supported on Cu(111) using XPS and STM. The study of the ZnO/Cu(111) system is experiencing a great revival of interests, given its importance as a catalyst in the synthesis of methanol [107-111]. This process is related to the catalytic reaction of CO_2 hydrogenation with the help of the ZnO/Cu catalyst. One of the major advantages of this mechanism is the possibility of transforming a greenhouse gas into a highly useful chemical product, both as an intermediate in the synthesis, such as formaldehyde, or as a product for energy storage, i.e. oxymethylene dimethyl ethers [107, 112]. The Cu/Zn catalyst is now the most important state-of-art industrial catalyst for methanol synthesis, but this catalyst suffers from the degradation of catalytic performance and the poor control of the fabrication. Therefore, the aim of this research project is to improve the performance of this catalyst through a better understanding of catalytic reaction of CO_2 hydrogenation on the ZnO/Cu catalyst.

Appendix: Synthesis of the large-diameter ZnTe crystal for THz emitting and detection

A high-quality, large-size ZnTe ingot with the diameter of 60 mm and the length of 80 mm were prepared by the modified temperature gradient solvent method, where the Te rich solution acted as both solubility promoter and reactant. Using this method, the crystallization temperature was reduced from 1568 K to 1333 K, plus, the crystal defects could be reduced in some extent due to the lower zinc partial pressure. The qualities and properties of the ZnTe crystals were analyzed using X-ray diffraction (XRD), infrared transmission microscope, fourier transform infrared (FT-IR) spectrometer, ultraviolet–visible (UV–Vis) spectrophotometer. Besides, the terahertz (THz) radiation and detection spectra of the ZnTe crystal were obtained using terahertz time-domain spectroscopy (THz-TDS) at room temperature.

Introduction

Terahertz (THz) radiation as the electromagnetic waves falls in between infrared radiation and microwave radiation in the electromagnetic spectrum with the band of frequencies from 0.3 THz to 10 THz (wavelengths from 1 mm to 0.1 mm) [113-116]. Up to now, THz technology based on THz radiation has been widely employed in many fields, including medical imaging [117-119], security inspection [120, 121], communication [122], amateur radio [123, 124], etc. Generation and detection of THz pulses through electro-optical rectification technique has been proved to be the most direct and effective way. The electro-optical crystals, such as $LiNbO_3$, $LiTaO_3$, DAST, GaAs and ZnTe [123-125], have been used for the THz radiation generation and detection [126-129]. Among of these electro-optical crystals, single crystal ZnTe demonstrates superior performance in detective sensitivity, detective bandwidth, and stability [130-133]. Meanwhile, ZnTe showed large second-order nonlinear susceptibility and favorable phase-matching conditions with 800 nm light, which are vital important for producing terahertz emitter and sensor [134].

However, the preparation of ZnTe crystal with high quality is still remaining a big challenge because of its high melting point (1295 °C), low thermal conductivity and low stacking fault energy. So far, several methods have been developed for the synthesis of ZnTe crystals, such as physical vapor transport technique [135-138], cold travelling heater method

[139], vertical Bridgman method [140], and double crucible liquid encapsulated pulling method [141, 142]. But most methods involve complex synthetic route, which cannot avoid the introduction of impurities in ZnTe crystals. Take vertical Bridgman method used by Seki Y et al. [143] as example, a sapphire substrate used as seed crystal enabled ZnTe crystal growth in a controllable direction to form single crystal, by suppressing the multi-crystal generation in a certain extent. However, poor ZnTe multi-crystal appears in the contact area between the sapphire and ZnTe crystal. In addition, this synthetic route is costly and complex due to the high cost of sapphire and the requirement of high-insensitive production equipment. Although the ZnTe crystal with high quality could be easily produced by physical vapor transport technique, it is unsuitable to grow the large size ZnTe crystal for mass production due to its low growth rate. Therefore, identification of a highly efficient and general synthetic route for the production of large-size ZnTe crystals remains a serious challenge.

Recently, a temperature gradient solvent method was developed for the synthesis of electro-optical crystals. In 2016, Kinoshita et al [144] successfully prepared the homogeneous $Si_{0.5}Ge0_{0.5}$ crystals by using temperature gradient solvent method. This method not only significantly reduces temperature and vapor pressure for the crystal growth, but also avoid the contamination from the crucible. However, the dimensions of most crystals synthesized based on this method were relatively small because the used solubility promoter limited the size of crystal.

Herein, a large-diameter ZnTe ingot with high purity was prepared by the modified temperature gradient solvent method, the Te rich solution acted as both solubility promoter and reactant. In this case, the growth temperature and zinc partial pressure were much lower than that of in-melting growth, through which the crystal defects were reduced. In addition, the synthesis and crystal growth can be carried out in the same ampoule, which simplified the procedure and reduced the possibility of contamination of ZnTe crystal. The synthesized large-diameter ZnTe crystal was characterized using different technologies. Finally, the performance of ZnTe crystal as a THz emission and detection device was measured.

Experimental setup

ZnTe crystals were grown by the temperature gradient solvent method in a super-saturated solution with the mole ratio of Zn: Te = 3:7. High purity elemental Zn (7N) and Te (7N) raw materials were sealed in a quartz ampoule and then synthesized in a rocking furnace under 1100 ℃ for 24 h. Then, a quench process to room temperature with the cooling rate of

15 °C/h was carried out to reduce concentration segregation in the ingot. After that the ampoule was transferred to a modified vertical Bridgman furnace for crystal growth. The growth process was undertaken at the normal Bridgman process by pulling down the ampoule through the gradient temperature field with pulling rate of less than 0.3 mm/h. After the growth, the temperature was gradually decreased with the cooling rate of 15 °C/h. ⟨110⟩ direction wafers free from twins and grain boundaries with the dimension of 10 × 10 × 2 mm^3 were cut from the as-grown ZnTe ingot. The samples were mechanically lapped and chemo-mechanical polished prior to performing the measurements.

The phase purity of the Te-rich polycrystals and the resulting ZnTe crystals were characterized by X-ray powder diffraction (a RICOH D/max2500 powder X-ray Diffractometer). Crystallization quality of ZnTe crystal was tested by using Raman spectroscopy with 785 nm laser (Renishaw RM1000). The UV–Visible-NIR (SHI-MADZU UV-3150) and Fourier transform infrared spectrometer (Nicolet Nexus) were used to extract the transmittance spectra at room temperature. Imaging of Te-rich particles was measured by using an IR transmission microscopy (IRTM) system. THz spectra were obtained using THz-TDS system at room temperature. In this THz-TDS setup, the laser source was a Ti: Sa femtosecond regenerative amplifier (RegA 9000, Coherent Inc.) operating at a repetition rate of 250 kHz and delivering 120 fs long pulses with a central wavelength of 800 nm. A beam splitter was used to split the laser beam into two: a pump beam (~90%) and a weak probe beam (~10%). The strong pump beam went through an optical delay line and then was focused on ZnTe crystal to generate pulsed THz wave, while the weak beam was focused on ZnTe detector to detect THz radiation from ZnTe emitter. A silicon slice was used as a filter to block the pump light. The transmitted THz beam was collimated with a parabolic mirror first and then focused on to ZnTe detector with another parabolic mirror. The probe beam is focused on the same spot of ZnTe detector as the THz wave. After passing through quarter wave plate (λ/4) and a Wollaston prism, a differential detection with balanced photodiodes was used to measure the different intensities of the probe beam caused by generated THz wave. The final differential signal from balanced photodiodes was collected with a lock-in amplifier and then processed with the computer.

Results and discussion

As shown in Figure 1 (a), the as-grown ZnTe ingot with the diameter of 60 mm and the length of 80 mm is made up of two parts, i.e. as-grown ZnTe crystal and the mixture of ZnTe

and Te solution. The as-grown cross-sectional slice of ZnTe wafer contains several grains but has large size single crystals, including those with the cross-section areas of 30 mm × 35 mm and 25 mm × 25 mm, as shown in Figure 1 (b). To the best of our knowledge, the size of as-grown ZnTe ingots in current research is larger than those ever reported by using the similar growth method [141]. The as-grown ZnTe single crystal shows the transparency with reddish orange color (Figure 1 (c)) because the absorption edge of ZnTe crystal is about 550 nm at the room temperature, which is corresponding to the wavelength of visible light.

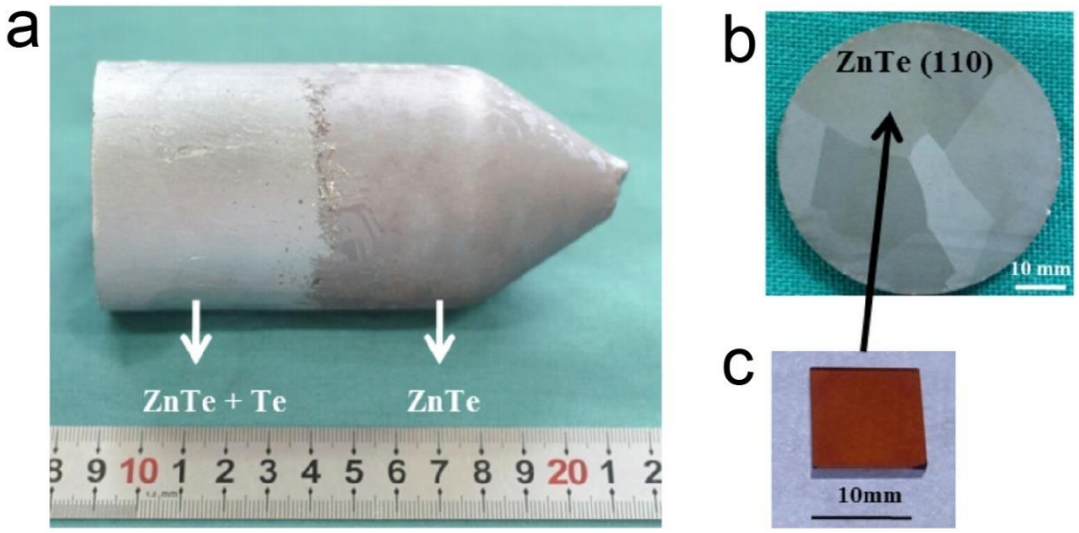

Figure 1: As-grown ZnTe crystal (a) The ZnTe ingot; (b) The cross-sectional slice of ZnTe wafer; (c) ⟨110⟩ direction of ZnTe (10 mm × 10 mm × 2 mm) crystal.

Figure 2 (a) shows the X-ray diffraction pattern of ⟨110⟩-oriented ZnTe crystal with a sharp (220) peak, indicating that the ZnTe crystal has a perfect configuration without any other orientation. In addition, the narrow and strong XRD peak at (220) crystal plane suggests that the ZnTe single crystal has a high crystalline quality. Furthermore, the Figure 2 (b) shows the normalized Raman spectra from 125-500 cm^{-1} of the ZnTe crystal at room temperature. The transverse optic (TO) and longitudinal optic (LO) modes at the U-point correspond to the first-order Raman Scattering peaks [1]. The second $2TA_2(K)$ in the low-frequency region and a mixed two-phonon combination (LO(L) + TA(L) and LO(X) + TA(X)) above the LO(Γ) are observed respectively. Generally, the LO(Γ) peak is dominated by the crystallinity. The full width at half maximum (FWHM) of the LO peak is fitted with FWHM of 2.66 cm^{-1}, as shown in the inset of Figure 2 (b). Moreover, the corresponding peak Intensity (I) to FWHM ratio is 23857, which suggests the high quality of the ZnTe crystal. The clearly obvious LO(L) + TA(L) and LO(X) + TA(X) peaks reflect the low dislocation density in the ZnTe crystal, because the two peaks are normally degraded by the dislocation related strain [113].

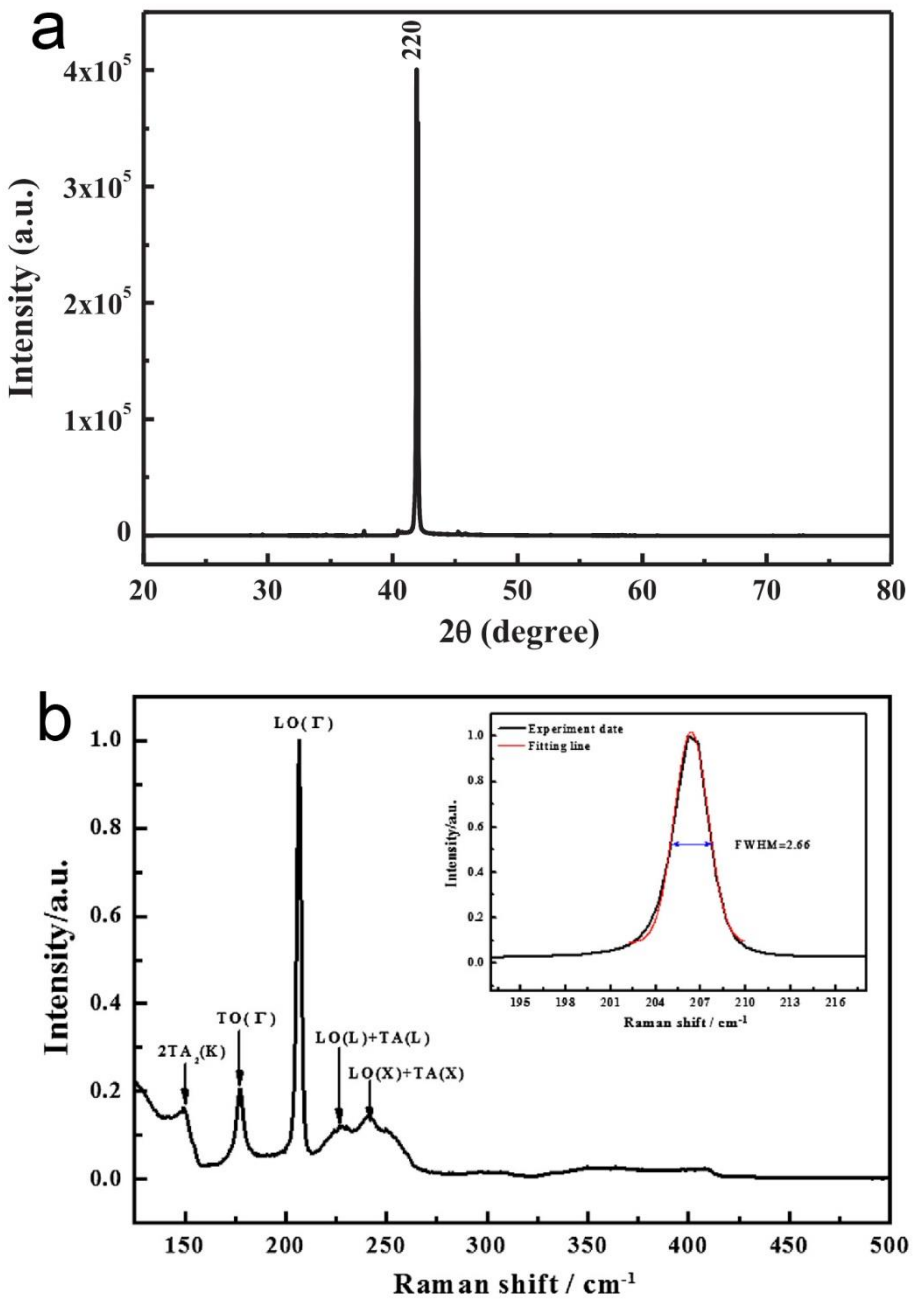

Figure 2: (a) X-ray diffraction spectrum of ZnTe single crystal; (b) The normalized Raman spectra from 125 to 500 cm^{-1} of the ZnTe crystal.

Next, the typical infrared transmittance image of the ZnTe single crystal is shown in Figure 3 (a). A small number of Te inclusions (black dot), distributed uniformly with the typical size of 3-10 μm are found in the ZnTe single crystal, as seen in Figure 3 (b). The total concentration of Te inclusions over the whole ZnTe single crystal was estimated to be less than 0.1%, which indicated the preferable crystal quality.

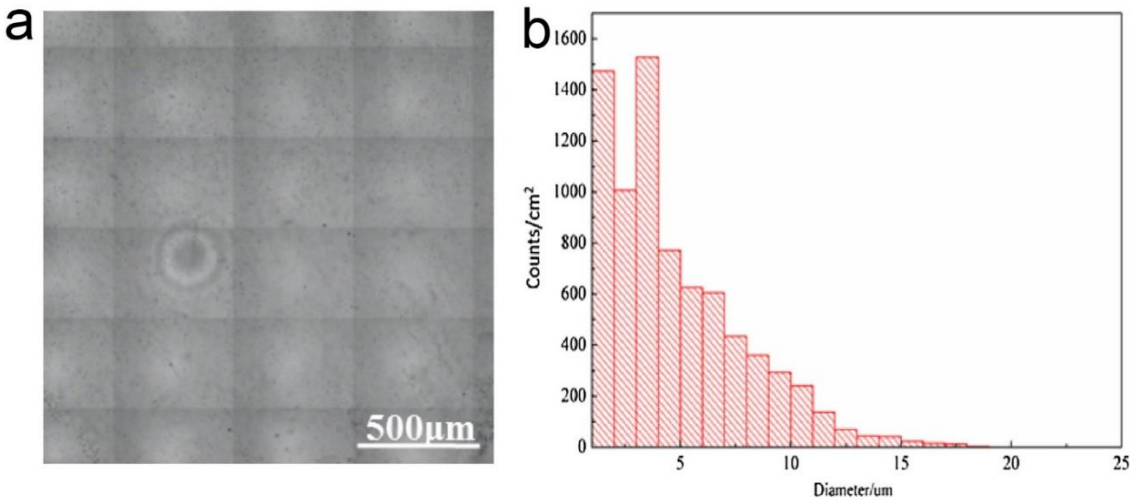

Figure 3: (a) The infrared transmittance images of the ZnTe single crystal; (b) The size distribution diagram of Te inclusions in the ZnTe single crystal.

A rather high transmission, around 60% is obtained in the infrared spectrum over the wavenumber range from 500 to 4000 cm^{-1}, as shown in Figure 4 (a). Referring to the mechanisms for IR absorption reported by Li et al. [145], the relatively high IR transmission is consistent with a low concentration of lattice defects, such as dislocations and micro precipitates, this is due to the generation of bubbles during the growth of ZnTe crystal. At the range of high wave numbers, the IR transmittance is mainly influenced by the lattice absorption and is closely related to the dislocation density. The existence of Te inclusions will induce dislocations in the ZnTe crystal [146], which lead to enhance lattice absorption. The formation of the induced dislocation is not only related to the number of Te inclusions, but also the size of them. It is confirmed that there is almost no large size Te inclusions in the crystal, otherwise they will cause the transmission curve decline in the long wave band [147]. The transmittance spectrum of ZnTe over the wavelength range from 200 nm to 2600 nm is shown in Figure 4 (b). The smooth transmission curve in the wide spectra range reflects the high quality of the crystals. The absorption edge is about 543.7 nm.

The insert data in Figure 4 (b) shows the allowed transition by plotting $(\alpha h\upsilon)^2$ vs. $h\upsilon$ for calculating the optical band gap of the ZnTe single crystal. Extrapolating the straight line to X-axis($h\upsilon$) gives a direct optical band gap of 2.23 eV. This value did not show large deviation from the reported band gap of ZnTe (Eg = 2.26 eV) [148].

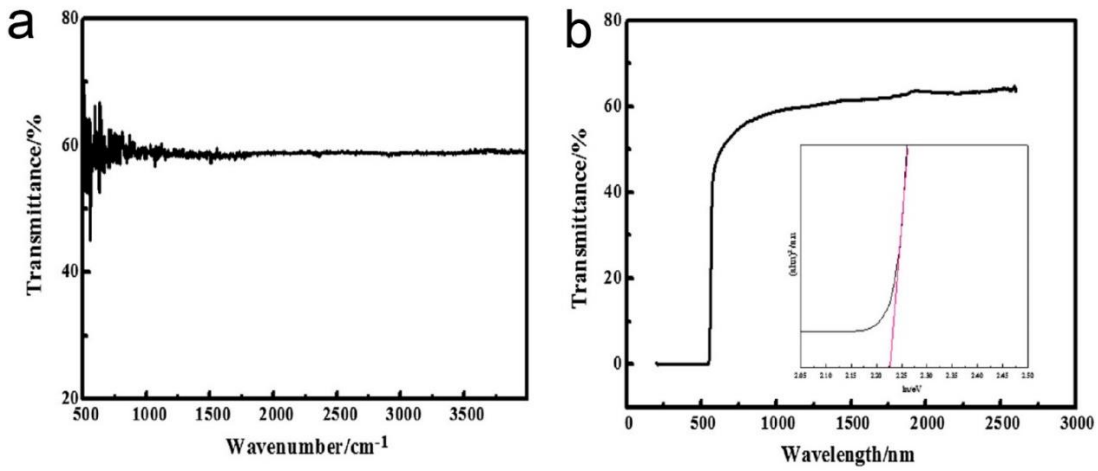

Figure 4: Transmission spectra of as-grown ZnTe crystal: (a) Infrared transmission spectrum; (b) Ultraviolet-visible-near infrared spectrum of ZnTe, inset is the plot of $(\alpha h\upsilon)^2$ vs. $h\upsilon$.

THz emitter and detector were fabricated with self-grown ZnTe crystal and evaluated by using the THz-TDS system (Figure 5 (a)). The time-domain waveforms are shown in Figure 5 (b) and (c). Figure 5 (d) and (e) show the spectra obtained from the temporal waveforms by using the Fast-Fourier-Transform (FFT) method. Figure 5 (d) shows the frequency of the peak, which is approximately 1.22 THz and the frequency of the spectra response is about 3 THz. The dip in the emission spectrum near 1.7 THz can be attributed to an absorption peak of ZnTe. In addition, the pulse width (FWHM) of the temporal waveform is about 0.34 ps for the THz pulse with the ZnTe electro-optic effect detection (Figure 5 (c)). As shown in Figure 5 (e), the frequency for the peak is about 0.69 THz, and spectrum response is more than 3 THz with the half bank width of 1.15 THz. Plus, the strongest signal appears at 0.69 THz, which agrees with the phase matching condition for electro-optical ZnTe crystal. It could be concluded that the ZnTe single crystals grown by temperature gradient solvent method have successfully emitted and detected the THz signal.

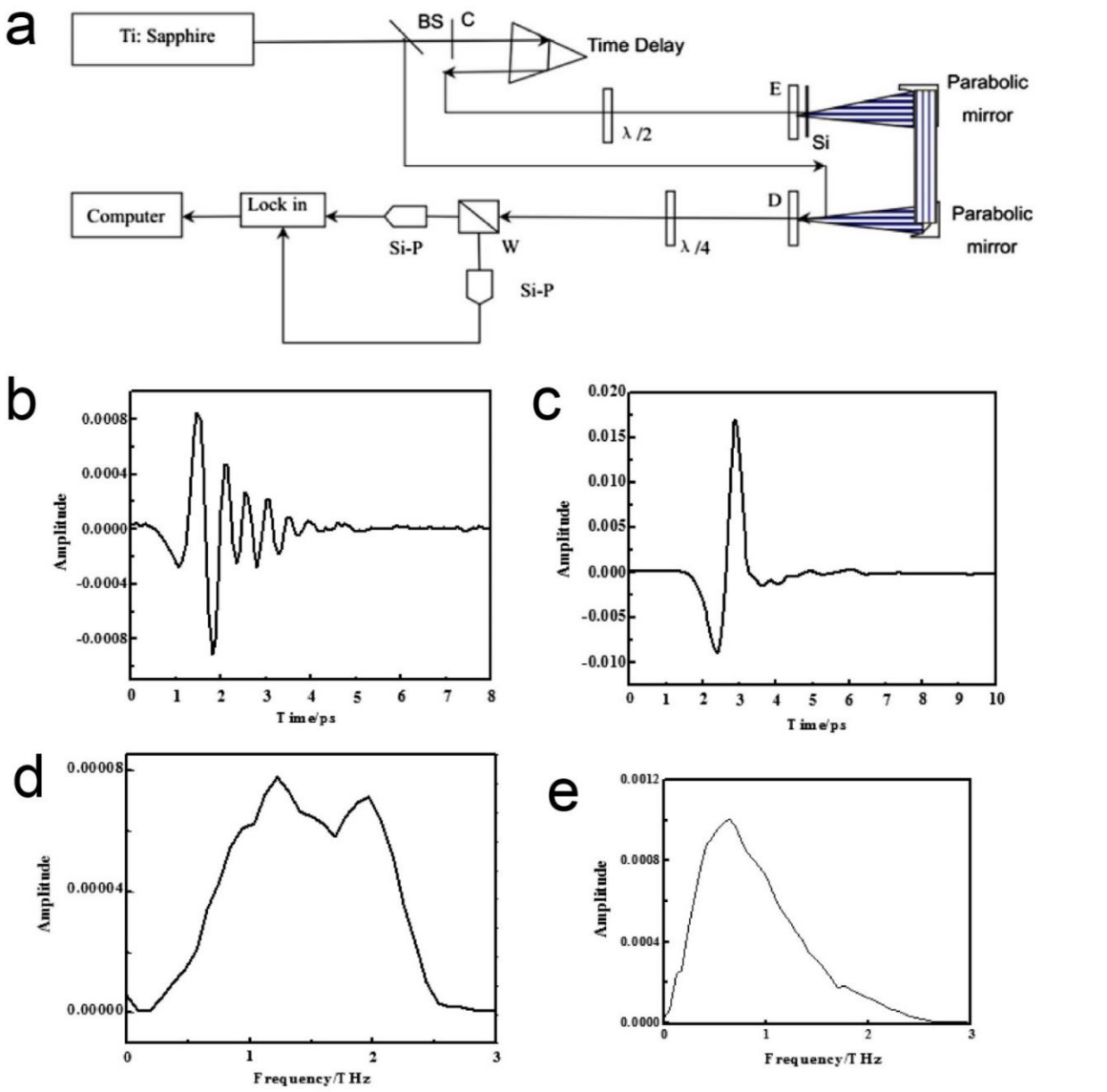

Figure 5: THz emission and detection. (a) Schematic diagram of THz-TDS, the normalized time domain THz waveforms via, (b) optical rectification emission; (c) Electro-optic effect detection; (d) The corresponding frequency domain THz waveforms of emission and (e) a detection spectrum.

Conclusions

A modified temperature gradient solvent method was success-fully applied to fabricate the large-diameter (Φ60 mm × 80 mm) ZnTe crystal with high quality and low etch pit density (EPD). The optical band gap of the as-grown ZnTe single crystal was calculated to be 2.23 eV, and IR transmittance was about 60% over the wavenumber range from 500 to 4000 cm^{-1}. The good performance from the THz-TDS results presents that the ZnTe crystal is suitable for the fabrication of emitter and detector for THz waves.

References

[1] OECD I. Energy and Air Pollution: World Energy Outlook Special Report 2016.

[2] Edwards P P, Kuznetsov V L, David W I and Brandon N P. Hydrogen and fuel cells: towards a sustainable energy future. Energy policy, 36 (12), 4356-4362, 2008.

[3] Carrette L, Friedrich K and Stimming U. Fuel cells–fundamentals and applications. Fuel cells, 1 (1), 5-39, 2001.

[4] Schlapbach L. Technology: Hydrogen-fuelled vehicles. Nature, 460 (7257), 809, 2009.

[5] Toyoshima R and Kondoh H. In-situ observations of catalytic surface reactions with soft x-rays under working conditions. Journal of Physics: Condensed Matter, 27 (8), 083003, 2015.

[6] Holton O T and Stevenson J W. The role of platinum in proton exchange membrane fuel cells. Platinum Metals Review, 57 (4), 259-271, 2013.

[7] Tang Y, Yang Z and Dai X. A theoretical simulation on the catalytic oxidation of CO on Pt/graphene. Physical Chemistry Chemical Physics, 14 (48), 16566-16572, 2012.

[8] Seriani N and Mittendorfer F. Platinum-group and noble metals under oxidizing conditions. Journal of Physics: Condensed Matter, 20 (18), 184023, 2008.

[9] Gandhi H, Graham G and McCabe R W. Automotive exhaust catalysis. Journal of catalysis, 216 (1-2), 433-442, 2003.

[10] Hendriksen B and Frenken J. CO oxidation on Pt (110): scanning tunneling microscopy inside a high-pressure flow reactor. Physical review letters, 89 (4), 046101, 2002.

[11] Kattel S, Yan B, Chen J G and Liu P. CO2 hydrogenation on Pt, Pt/SiO2 and Pt/TiO2: Importance of synergy between Pt and oxide support. Journal of catalysis, 343, 115-126, 2016.

[12] Lopes P P, Freitas K S and Ticianelli E A. CO tolerance of PEMFC anodes: mechanisms and electrode designs. Electrocatalysis, 1 (4), 200-212, 2010.

[13] Cheng X, Shi Z, Glass N, Zhang L, Zhang J, Song D, Liu Z-S, Wang H and Shen J. A review of PEM hydrogen fuel cell contamination: Impacts, mechanisms, and mitigation. Journal of Power Sources, 165 (2), 739-756, 2007.

[14] Blyholder G. Molecular orbital view of chemisorbed carbon monoxide. The Journal of Physical Chemistry, 68 (10), 2772-2777, 1964.

[15] Kang Y, Ye X, Chen J, Qi L, Diaz R E, Doan-Nguyen V, Xing G, Kagan C R, Li J and Gorte R J. Engineering catalytic contacts and thermal stability: gold/iron oxide binary

nanocrystal superlattices for CO oxidation. Journal of the American Chemical Society, 135 (4), 1499-1505, 2013.

[16] Naitabdi A, Fagiewicz R, Boucly A, Olivieri G, Bournel F, Tissot H, Xu Y, Benbalagh R, Silly M G and Sirotti F. Oxidation of small supported platinum-based nanoparticles under near-ambient pressure exposure to oxygen. Topics in Catalysis, 59 (5-7), 550-563, 2016.

[17] Rodriguez J A, Liu P, Graciani J, Senanayake S D, Grinter D C, Stacchiola D, Hrbek J and Fernández-Sanz J. Inverse oxide/metal catalysts in fundamental studies and practical applications: a perspective of recent developments. The journal of physical chemistry letters, 7 (13), 2627-2639, 2016.

[18] Naitabdi A, Boucly A, Rochet F, Fagiewicz R, Olivieri G, Bournel F, Benbalagh R, Sirotti F and Gallet J-J. CO oxidation activity of Pt, Zn and ZnPt nanocatalysts: a comparative study by in situ near-ambient pressure X-ray photoelectron spectroscopy. Nanoscale, 10 (14), 6566-6580, 2018.

[19] Martynova Y, Liu B-H, McBriarty M, Groot I, Bedzyk M, Shaikhutdinov S and Freund H-J. CO oxidation over ZnO films on Pt (1 1 1) at near-atmospheric pressures. Journal of catalysis, 301, 227-232, 2013.

[20] Yi L, Wei W, Zhao C, Yang C, Tian L, Liu J and Wang X. Electrochemical oxidation of sodium borohydride on carbon supported Pt-Zn nanoparticle bimetallic catalyst and its implications to direct borohydride-hydrogen peroxide fuel cell. Electrochimica Acta, 158, 209-218, 2015.

[21] Kang Y J, Chun S-J, Lee S-S, Kim B-Y, Kim J H, Chung H, Lee S-Y and Kim W. All-solid-state flexible supercapacitors fabricated with bacterial nanocellulose papers, carbon nanotubes, and triblock-copolymer ion gels. ACS nano, 6 (7), 6400-6406, 2012.

[22] Shao M, Chang Q, Dodelet J-P and Chenitz R. Recent advances in electrocatalysts for oxygen reduction reaction. Chemical reviews, 116 (6), 3594-3657, 2016.

[23] Rodríguez J A and Hrbek J. Inverse oxide/metal catalysts: A versatile approach for activity tests and mechanistic studies. Surface Science, 604 (3-4), 241-244, 2010.

[24] Ertl G, Knözinger H and Weitkamp J. Handbook of heterogeneous catalysis. 1997.

[25] Fernandez-Garcia M, Martinez-Arias A, Hanson J and Rodriguez J. Nanostructured oxides in chemistry: characterization and properties. Chemical reviews, 104 (9), 4063-4104, 2004.

[26] Shaikhutdinov S and Freund H-J. Ultrathin oxide films on metal supports: structure-reactivity relations. Annual review of physical chemistry, 63, 619-633, 2012.

[27] Janotti A and Van de Walle C G. Fundamentals of zinc oxide as a semiconductor. Reports on progress in physics, 72 (12), 126501, 2009.

[28] Özgür Ü, Alivov Y I, Liu C, Teke A, Reshchikov M, Doğan S, Avrutin V, Cho S-J and Morkoç H. A comprehensive review of ZnO materials and devices. Journal of applied physics, 98 (4), 11, 2005.

[29] Wöll C. The chemistry and physics of zinc oxide surfaces. Progress in Surface Science, 82 (2-3), 55-120, 2007.

[30] Dulub O, Boatner L A and Diebold U. STM study of the geometric and electronic structure of ZnO (0 0 0 1)-Zn,(0 0 0 $\bar{1}$)-O,(1 0 $\bar{1}$ 0), and (1 1 $\bar{2}$ 0) surfaces. Surface Science, 519 (3), 201-217, 2002.

[31] Liu B-H, Preparation and Structure of Ultra-Thin Zinc Oxide Films on Pt (111), Ag (111) and Cu (111), in, 2015,

[32] Tang C, Spencer M J and Barnard A S. Activity of ZnO polar surfaces: an insight from surface energies. Physical Chemistry Chemical Physics, 16 (40), 22139-22144, 2014.

[33] Dulub O, Diebold U and Kresse G. Novel stabilization mechanism on polar surfaces: ZnO (0001)-Zn. Physical review letters, 90 (1), 016102, 2003.

[34] Weirum G, Barcaro G, Fortunelli A, Weber F, Schennach R, Surnev S and Netzer F. Growth and surface structure of zinc oxide layers on a Pd (111) surface. The Journal of Physical Chemistry C, 114 (36), 15432-15439, 2010.

[35] Nilius N. Properties of oxide thin films and their adsorption behavior studied by scanning tunneling microscopy and conductance spectroscopy. Surface Science Reports, 64 (12), 595-659, 2009.

[36] Kresse G, Dulub O and Diebold U. Competing stabilization mechanism for the polar ZnO (0001)-Zn surface. Physical Review B, 68 (24), 245409, 2003.

[37] Lauritsen J V, Porsgaard S, Rasmussen M K, Jensen M C, Bechstein R, Meinander K, Clausen B S, Helveg S, Wahl R and Kresse G. Stabilization principles for polar surfaces of ZnO. ACS nano, 5 (7), 5987-5994, 2011.

[38] Brauer G, Anwand W, Grambole D, Grenzer J, Skorupa W, Čížek J, Kuriplach J, Procházka I, Ling C and So C. Identification of Zn-vacancy–hydrogen complexes in ZnO single crystals: A challenge to positron annihilation spectroscopy. Physical Review B, 79 (11), 115212, 2009.

[39] Meyer B and Marx D. Density-functional study of the structure and stability of ZnO surfaces. Physical Review B, 67 (3), 035403, 2003.

[40] Claeyssens F, Freeman C L, Allan N L, Sun Y, Ashfold M N and Harding J H. Growth of ZnO thin films—experiment and theory. Journal of Materials Chemistry, 15 (1), 139-148, 2005.

[41] Freeman C L, Claeyssens F, Allan N L and Harding J H. Graphitic nanofilms as precursors to wurtzite films: theory. Physical review letters, 96 (6), 066102, 2006.

[42] Tusche C, Meyerheim H and Kirschner J. Observation of depolarized ZnO (0001) monolayers: formation of unreconstructed planar sheets. Physical review letters, 99 (2), 026102, 2007.

[43] Deng X, Yao K, Sun K, Li W-X, Lee J and Matranga C. Growth of single-and bilayer ZnO on Au (111) and interaction with copper. The Journal of Physical Chemistry C, 117 (21), 11211-11218, 2013.

[44] Lee J, Sorescu D C and Deng X. Tunable lattice constant and band gap of single-and few-layer ZnO. The journal of physical chemistry letters, 7 (7), 1335-1340, 2016.

[45] Liu B-H, McBriarty M E, Bedzyk M J, Shaikhutdinov S and Freund H-J. Structural transformations of zinc oxide layers on Pt (111). The Journal of Physical Chemistry C, 118 (49), 28725-28729, 2014.

[46] Fu Q, Li W-X, Yao Y, Liu H, Su H-Y, Ma D, Gu X-K, Chen L, Wang Z and Zhang H. Interface-confined ferrous centers for catalytic oxidation. science, 328 (5982), 1141-1144, 2010.

[47] Mu R, Fu Q, Xu H, Zhang H, Huang Y, Jiang Z, Zhang S, Tan D and Bao X. Synergetic effect of surface and subsurface Ni species at Pt− Ni bimetallic catalysts for CO oxidation. Journal of the American Chemical Society, 133 (6), 1978-1986, 2011.

[48] Sun D, Gu X-K, Ouyang R, Su H-Y, Fu Q, Bao X and Li W-X. Theoretical study of the role of a metal–cation ensemble at the oxide–metal boundary on CO oxidation. The Journal of Physical Chemistry C, 116 (13), 7491-7498, 2012.

[49] Knudsen J, Andersen J N and Schnadt J. A versatile instrument for ambient pressure x-ray photoelectron spectroscopy: The Lund cell approach. Surface Science, 646, 160-169, 2016.

[50] Gao F, Wang Y, Cai Y and Goodman D. CO oxidation on Pt-group metals from ultrahigh vacuum to near atmospheric pressures. 2. Palladium and platinum. The Journal of Physical Chemistry C, 113 (1), 174-181, 2008.

[51] Campbell C, Ertl G, Kuipers H and Segner J. A molecular beam study of the catalytic oxidation of CO on a Pt (111) surface. The Journal of Chemical Physics, 73 (11), 5862-5873, 1980.

[52] Binnig G, Rohrer H, Gerber C and Weibel E. Surface studies by scanning tunneling microscopy. Physical review letters, 49 (1), 57, 1982.

[53] Binnig G and Rohrer H. Scanning tunneling microscopy. Surface Science, 126 (1-3), 236-244, 1983.

[54] Binnig G, Rohrer H, Gerber C and Weibel E. Tunneling through a controllable vacuum gap. Applied Physics Letters, 40 (2), 178-180, 1982.

[55] Bardeen J. Tunnelling from a many-particle point of view. Physical review letters, 6 (2), 57, 1961.

[56] Tersoff J and Hamann D. Theory and application for the scanning tunneling microscope. Physical review letters, 50 (25), 1998, 1983.

[57] Tersoff J and Hamann D. Theory of the scanning tunneling microscope. Physical Review B, 31 (2), 805, 1985.

[58] Yu Z, Wang C M, Du Y, Thevuthasan S and Lyubinetsky I. Reproducible tip fabrication and cleaning for UHV STM. Ultramicroscopy, 108 (9), 873-877, 2008.

[59] Nam A, Teren A, Lusby T and Melmed A. Benign making of sharp tips for STM and FIM: Pt, Ir, Au, Pd, and Rh. Journal of Vacuum Science & Technology B: Microelectronics and Nanometer Structures Processing, Measurement, and Phenomena, 13 (4), 1556-1559, 1995.

[60] Ekvall I, Wahlström E, Claesson D, Olin H and Olsson E. Preparation and characterization of electrochemically etched W tips for STM. Measurement Science and Technology, 10 (1), 11, 1999.

[61] Davisson C and Germer L H. Diffraction of electrons by a crystal of nickel. Physical review, 30 (6), 705, 1927.

[62] Davisson C and Germer L H. The scattering of electrons by a single crystal of nickel. Nature, 119 (2998), 558, 1927.

[63] Wood E A. Vocabulary of surface crystallography. Journal of applied physics, 35 (4), 1306-1312, 1964.

[64] Siegbahn K. Electron spectroscopy for atoms, molecules, and condensed matter. Reviews of Modern Physics, 54 (3), 709, 1982.

[65] Boucly A, Catalytical reactions and environmental chemistry modifications as seen by synchrotron radiation NAP-XPS, in, Université Pierre et Marie Curie-Paris VI, 2017,

[66] Shavorskiy A, Karslioglu O, Zegkinoglou I and Bluhm H. Synchrotron-based ambient pressure X-ray photoelectron spectroscopy. Synchrotron Radiation News, 27 (2), 14-23, 2014.

[67] Arble C, Jia M and Newberg J T. Lab-based ambient pressure X-ray photoelectron spectroscopy from past to present. Surface Science Reports, 73 (2), 37-57, 2018.

[68] Tissot H, Gallet J-J, Bournel F, Olivieri G, Silly M G, Sirotti F, Boucly A and Rochet F. The electronic structure of saturated NaCl and NaI solutions in contact with a gold substrate. Topics in Catalysis, 59 (5-7), 605-620, 2016.

[69] Miller P E and Denton M B. The quadrupole mass filter: basic operating concepts. Journal of chemical education, 63 (7), 617, 1986.

[70] Kondoh H, Toyoshima R, Monya Y, Yoshida M, Mase K, Amemiya K and Mun B S. In situ analysis of catalytically active Pd surfaces for CO oxidation with near ambient pressure XPS. Catalysis Today, 260, 14-20, 2016.

[71] Schott V, Oberhofer H, Birkner A, Xu M, Wang Y, Muhler M, Reuter K and Wöll C. Chemical Activity of Thin Oxide Layers: Strong Interactions with the Support Yield a New Thin‐Film Phase of ZnO. Angewandte Chemie International Edition, 52 (45), 11925-11929, 2013.

[72] Deng X, Sorescu D C and Lee J. Enhanced adsorption of CO 2 at steps of ultrathin ZnO: the importance of Zn–O geometry and coordination. Physical Chemistry Chemical Physics, 19 (7), 5296-5303, 2017.

[73] Pan Q, Liu B H, McBriarty M, Martynova Y, Groot I, Wang S, Bedzyk M, Shaikhutdinov S and Freund H-J. Reactivity of ultra-thin ZnO films supported by Ag (111) and Cu (111): a comparison to ZnO/Pt (111). Catalysis letters, 144 (4), 648-655, 2014.

[74] Chen H, Lin L, Li Y, Wang R, Gong Z, Cui Y, Li Y, Liu Y, Zhao X and Huang W. CO and H2 activation over g-ZnO layers and w-ZnO (0001). ACS Catalysis, 2018.

[75] Naitabdi A, Ono L and Roldan Cuenya B. Local investigation of the electronic properties of size-selected Au nanoparticles by scanning tunneling spectroscopy. Applied Physics Letters, 89 (4), 043101, 2006.

[76] Naitabdi A, Rochet F, Carniato S, Bournel F and Gallet J-J. Room temperature differential conductance measurements of triethylamine molecules adsorbed on Si (001). Physical Chemistry Chemical Physics, 18 (33), 23231-23237, 2016.

[77] Bikaljevic D, Rameshan R, Köpfle N, Götsch T, Mühlegger E, Schlögl R, Penner S, Memmel N and Klötzer B. Structural and kinetic aspects of CO oxidation on ZnOx-modified Cu surfaces. Applied Catalysis A: General, 2019.

[78] Pan Q, Liu B H, McBriarty M, Martynova Y, Groot I, Wang S, Bedzyk M J, Shaikhutdinov S and Freund H-J. Reactivity of ultra-thin ZnO films supported by Ag (111) and Cu (111): a comparison to ZnO/Pt (111). Catalysis letters, 144 (4), 648-655, 2014.

[79] Suchorski Y, Wrobel R, Becker S and Weiss H. CO oxidation on a CeO x/Pt (111) inverse model catalyst surface: catalytic promotion and tuning of kinetic phase diagrams. The Journal of Physical Chemistry C, 112 (50), 20012-20017, 2008.

[80] Schoiswohl J, Sock M, Chen Q, Thornton G, Kresse G, Ramsey M, Surnev S and Netzer F. Metal supported oxide nanostructures: model systems for advanced catalysis. Topics in Catalysis, 46 (1-2), 137-149, 2007.

[81] Salmeron M and Schlögl R. Ambient pressure photoelectron spectroscopy: A new tool for surface science and nanotechnology. Surface Science Reports, 63 (4), 169-199, 2008.

[82] Perry R H G. Perry's chemical engineers' handbook, edited by Robert H. Perry, Don W. Green, James O. Maloney. 1984.

[83] Schwartz S, Schmidt L and Fisher G B. Carbon monoxide+ oxygen reaction on rhodium (III): steady-state rates and adsorbate coverages. The Journal of Physical Chemistry, 90 (23), 6194-6200, 1986.

[84] Matera S, Blomberg S, Hoffmann M, Zetterberg J, Gustafson J, Lundgren E and Reuter K. Evidence for the active phase of heterogeneous catalysts through in situ reaction product imaging and multiscale modeling. ACS Catalysis, 5 (8), 4514-4518, 2015.

[85] Blomberg S, Zetterberg J, Gustafson J, Zhou J, Brackmann C and Lundgren E. Comparison of AP-XPS and PLIF measurements during CO oxidation over Pd single crystals. Topics in Catalysis, 59 (5-7), 478-486, 2016.

[86] Zhou J, Blomberg S, Gustafson J, Lundgren E and Zetterberg J. Visualization of gas distribution in a model AP-XPS reactor by PLIF: CO oxidation over a Pd (100) catalyst. Catalysts, 7 (1), 29, 2017.

[87] Björneholm O, Nilsson A, Tillborg H, Bennich P, Sandell A, Hernnäs B, Puglia C and Mårtensson N. Overlayer structure from adsorbate and substrate core level binding energy shifts: CO, CCH3 and O on Pt (111). Surface Science, 315 (1-2), L983-L989, 1994.

[88] Toyoshima R, Yoshida M, Monya Y, Suzuki K, Amemiya K, Mase K, Mun B S and Kondoh H. A high-pressure-induced dense CO overlayer on a Pt (111) surface: A chemical analysis using in situ near ambient pressure XPS. Physical Chemistry Chemical Physics, 16 (43), 23564-23567, 2014.

[89] Yu Y, Koh Y E, Lim H, Jeong B, Isegawa K, Kim D, Ueda K, Kondoh H, Mase K and Crumlin E J. Chemical states of surface oxygen during CO oxidation on Pt (1 1 0) surface revealed by ambient pressure XPS. Journal of Physics: Condensed Matter, 29 (46), 464001, 2017.

[90] Poelsema B, Palmer R L and Comsa G. Helium scattering and work function investigation of co adsorption on Pt (111) and vicinal surfaces. Surface Science, 123 (1), 152-164, 1982.

[91] Schnadt J, Knudsen J, Andersen J N, Siegbahn H, Pietzsch A, Hennies F, Johansson N, Mårtensson N, Öhrwall G and Bahr S. The new ambient-pressure X-ray photoelectron spectroscopy instrument at MAX-lab. Journal of synchrotron radiation, 19 (5), 701-704, 2012.

[92] Axnanda S, Scheele M, Crumlin E, Mao B, Chang R, Rani S, Faiz M, Wang S, Alivisatos A P and Liu Z. Direct work function measurement by gas phase photoelectron spectroscopy and its application on PbS nanoparticles. Nano letters, 13 (12), 6176-6182, 2013.

[93] van Spronsen M A, Frenken J W and Groot I M. Surface science under reaction conditions: CO oxidation on Pt and Pd model catalysts. Chemical Society Reviews, 46 (14), 4347-4374, 2017.

[94] Dupin J-C, Gonbeau D, Vinatier P and Levasseur A. Systematic XPS studies of metal oxides, hydroxides and peroxides. Physical Chemistry Chemical Physics, 2 (6), 1319-1324, 2000.

[95] Liu B-H, Boscoboinik J A, Cui Y, Shaikhutdinov S and Freund H-J. Stabilization of ultrathin zinc oxide films on metals: Reconstruction versus hydroxylation. The Journal of Physical Chemistry C, 119 (14), 7842-7847, 2015.

[96] Au C, Hirsch W and Hirschwald W. Adsorption and interaction of carbon dioxide, formic acid and hydrogen/carbon dioxide mixtures on (1010) zinc oxide surfaces studied by photoelectron spectroscopy (XPS and UPS). Surface Science, 199 (3), 507-517, 1988.

[97] Senanayake S D, Stacchiola D, Liu P, Mullins C B, Hrbek J and Rodriguez J A. Interaction of CO with OH on Au (111): HCOO, CO3, and HOCO as key intermediates in the water-gas shift reaction. The Journal of Physical Chemistry C, 113 (45), 19536-19544, 2009.

[98] Lindsay R, Michelangeli E, Daniels B G, Ashworth T V, Limb A J, Thornton G, Gutiérrez-Sosa A, Baraldi A, Larciprete R and Lizzit S. Impact of defects on the surface chemistry of ZnO (000$\bar{1}$)− O. Journal of the American Chemical Society, 124 (24), 7117-7122, 2002.

[99] Grabow L C, Gokhale A A, Evans S T, Dumesic J A and Mavrikakis M. Mechanism of the water gas shift reaction on Pt: First principles, experiments, and microkinetic modeling. The Journal of Physical Chemistry C, 112 (12), 4608-4617, 2008.

[100] Shido T and Iwasawa Y. Reactant-promoted reaction mechanism for water-gas shift reaction on ZnO, as the genesis of surface catalysis. Journal of catalysis, 129 (2), 343-355, 1991.

[101] Kiss J, Frenzel J, Nair N N, Meyer B and Marx D. Methanol synthesis on ZnO (000math). III. Free energy landscapes, reaction pathways, and mechanistic insights. 2012.

[102] Kiss J, Frenzel J, Meyer B and Marx D. Methanol synthesis on ZnO (000 1¯). II. Structure, energetics, and vibrational signature of reaction intermediates. The Journal of Chemical Physics, 139 (4), 044705, 2013.

[103] Mahapatra M, Gutiérrez R A, Kang J, Rui N, Hamlyn R, Liu Z, Orozco I, Ramírez P J, Senanayake S D and Rodriguez J A. The behavior of inverse oxide/metal catalysts: CO oxidation and water-gas shift reactions over ZnO/Cu (111) surfaces. Surface Science, 681, 116-121, 2019.

[104] Zhang J and Medlin J W. Catalyst design using an inverse strategy: From mechanistic studies on inverted model catalysts to applications of oxide-coated metal nanoparticles. Surface Science Reports, 2018.

[105] Zhao G, Yang F, Chen Z, Liu Q, Ji Y, Zhang Y, Niu Z, Mao J, Bao X and Hu P. Metal/oxide interfacial effects on the selective oxidation of primary alcohols. Nature communications, 8, 14039, 2017.

[106] Xu L, Ma Y, Zhang Y, Jiang Z and Huang W. Direct evidence for the interfacial oxidation of CO with hydroxyls catalyzed by Pt/oxide nanocatalysts. Journal of the American Chemical Society, 131 (45), 16366-16367, 2009.

[107] Kattel S, Ramírez P J, Chen J G, Rodriguez J A and Liu P. Active sites for CO2 hydrogenation to methanol on Cu/ZnO catalysts. science, 355 (6331), 1296-1299, 2017.

[108] Natesakhawat S, Lekse J W, Baltrus J P, Ohodnicki Jr P R, Howard B H, Deng X and Matranga C. Active sites and structure–activity relationships of copper-based catalysts for carbon dioxide hydrogenation to methanol. ACS Catalysis, 2 (8), 1667-1676, 2012.

[109] Bu Y, Weststrate C, Niemantsverdriet J and Fredriksson H O. Role of ZnO and CeO x in Cu-Based Model Catalysts in Activation of H2O and CO2 Dynamics Studied by in Situ Ultraviolet–Visible and X-ray Photoelectron Spectroscopy. ACS Catalysis, 6 (12), 7994-8003, 2016.

[110] Fujitani T, Nakamura I, Uchijima T and Nakamura J. The kinetics and mechanism of methanol synthesis by hydrogenation of CO2 over a Zn-deposited Cu (111) surface. Surface Science, 383 (2-3), 285-298, 1997.

[111] Palomino R M, Ramirez P J, Liu Z, Hamlyn R, Waluyo I, Mahapatra M, Orozco I, Hunt A, Simonovis J P and Senanayake S D. Hydrogenation of CO2 on ZnO/Cu (100) and ZnO/Cu (111) Catalysts: Role of Copper Structure and Metal–Oxide Interface in Methanol Synthesis. The Journal of Physical Chemistry B, 122 (2), 794-800, 2017.

[112] Yang Y, Evans J, Rodriguez J A, White M G and Liu P. Fundamental studies of methanol synthesis from CO 2 hydrogenation on Cu (111), Cu clusters, and Cu/ZnO (0001 [combining macron]). Physical Chemistry Chemical Physics, 12 (33), 9909-9917, 2010.

[113] Bakhtiari F, Golmohammady S, Yousefi M and Ghafary B. Terahertz radiation generation and shape control by interaction of array Gaussian laser beams with plasma. Physics of Plasmas, 23 (12), 123105, 2016.

[114] Hematizadeh A, Jazayeri S and Ghafary B. Generation of terahertz radiation by beating of two laser beams in collisional magnetized plasma. Laser and Particle Beams, 34 (4), 569-575, 2016.

[115] Rustagi A and Stanton C. Terahertz radiation from accelerating charge carriers in graphene under ultrafast photoexcitation. Physical Review B, 94 (19), 195207, 2016.

[116] Yadav D, Tombet S B, Watanabe T, Arnold S, Ryzhii V and Otsuji T. Terahertz wave generation and detection in double-graphene layered van der Waals heterostructures. 2D Materials, 3 (4), 045009, 2016.

[117] Jansen E D, Thomas R J, Wilmink G J and Ibey B L, Optical Interactions with Tissue and Cells XXV; and Terahertz for Biomedical Applications, in: Proc. of SPIE Vol, 2014, pp. 894101-894101

[118] Peter B S, Yngvesson S, Siqueira P, Kelly P, Khan A, Glick S and Karellas A. Development and testing of a single frequency terahertz imaging system for breast cancer detection. IEEE Transactions on Terahertz Science and Technology, 3 (4), 374-386, 2013.

[119] Vrba J, Oppl L, Vrbová B, Vrba D, Havelka D, Červinková K, Vojáčková L, Merunka I and Fišer O, Microwaves in medical diagnostics and treatment, in: 2014 24th International Conference Radioelektronika, IEEE, 2014, pp. 1-6

[120] Heinz E, May T, Born D, Zieger G, Anders S, Zakosarenko V, Meyer H-G and Schäffel C. Passive 350 GHz video imaging systems for security applications. Journal of Infrared, Millimeter, and Terahertz Waves, 36 (10), 879-895, 2015.

[121] Robin T, Bouye C and Cochard J, Terahertz applications: trends and challenges, in: Terahertz, RF, Millimeter, and Submillimeter-Wave Technology and Applications VII, International Society for Optics and Photonics, 2014, pp. 898512

[122] Srivastava N, Mansimov E and Salakhudinov R, Unsupervised learning of video representations using lstms, in: International conference on machine learning, 2015, pp. 843-852

[123] Blanchard F, Razzari L, Bandulet H-C, Sharma G, Morandotti R, Kieffer J-C, Ozaki T, Reid M, Tiedje H and Haugen H. Generation of 1.5 μJ single-cycle terahertz pulses by

optical rectification from a large aperture ZnTe crystal. Optics Express, 15 (20), 13212-13220, 2007.

[124] Fülöp J, Polónyi G, Monoszlai B, Andriukaitis G, Balciunas T, Pugzlys A, Arthur G, Baltuska A and Hebling J. Highly efficient scalable monolithic semiconductor terahertz pulse source. Optica, 3 (10), 1075-1078, 2016.

[125] Polónyi G, Monoszlai B, Gäumann G, Rohwer E J, Andriukaitis G, Balciunas T, Pugzlys A, Baltuska A, Feurer T and Hebling J. High-energy terahertz pulses from semiconductors pumped beyond the three-photon absorption edge. Optics Express, 24 (21), 23872-23882, 2016.

[126] Nagai M, Tanaka K, Ohtake H, Bessho T, Sugiura T, Hirosumi T and Yoshida M. Generation and detection of terahertz radiation by electro-optical process in GaAs using 1.56 μ m fiber laser pulses. Applied Physics Letters, 85 (18), 3974-3976, 2004.

[127] Pradarutti B, Matthäus G, Riehemann S, Notni G, Limpert J, Nolte S and Tünnermann A. Electro-optical sampling of ultrashort THz pulses by fs-laser pulses at 530 nm with BaTiO 3. Journal of applied physics, 102 (9), 093105, 2007.

[128] Wang Y, Ni H, Zhan W, Yuan J and Wang R. Electro-optical detection of THz radiation in Fe implanted LiNbO3. Optical Materials, 35 (3), 596-599, 2013.

[129] Youn D-H, Lee S-H, Ryu H-C, Jung S-Y, Kang S-B, Kwack M-H, Kim S, Choi S-K, Baek M-C and Kang K-Y. Effects of post-growth annealing on the structure and electro-optical properties of low-temperature grown GaAs. Journal of applied physics, 103 (12), 123528, 2008.

[130] Lu C, Zhang S, Jia T, Qiu J and Sun Z. Manipulation of terahertz pulse generation in ZnTe crystal by shaping femtosecond laser pulses with a square phase modulation. Optics Communications, 310, 90-93, 2014.

[131] Ollmann Z, Fülöp J A, Hebling J and Almási G. Design of a high-energy terahertz pulse source based on ZnTe contact grating. Optics Communications, 315, 159-163, 2014.

[132] Red'kin R A, Bereznaya S A, Korotchenko Z V and Sarkisov S Y. A comparison of terahertz electro-optic sampling in ZnTe, ZnSe, GaP and GaSe1-xSx crystals. 2015 International Siberian Conference on Control and Communications (Sibcon), 2015.

[133] Vidal S, Degert J, Tondusson M, Oberlé J and Freysz E. Impact of dispersion, free carriers, and two-photon absorption on the generation of intense terahertz pulses in ZnTe crystals. Applied Physics Letters, 98 (19), 191103, 2011.

[134] Zhang X-C and Xu J. Introduction to THz wave photonics. Springer, 2010

[135] Patel K, Solanki G, Gandhi J and Patel S. GROWTH AND CHARACTERIZATION OF ZnTe CRYSTALS GROWN BY PHYSICAL VAPOR TRANSPORT TECHNIQUE. Chalcogenide Letters, 6 (9), 2009.

[136] Sankar N, Ramachandran K and Sanjeeviraja C. Growth and characterization of ZnSe and phosphorus-doped ZnSe single crystals. Journal of crystal growth, 235 (1-4), 195-200, 2002.

[137] Su C-H, Sha Y-G, Volz M, Carpenter P and Lehoczky S. Vapor growth and characterization of ZnSeTe solid solutions. Journal of crystal growth, 216 (1-4), 104-112, 2000.

[138] Trigubó A, Di Stefano M, Gilabert U, Martínez A, D'Elía R, Cánepa H, Heredia E and Aguirre M. TEM, chemical etching and FTIR characterization of ZnTe grown by physical vapor transport. Crystal Research and Technology, 45 (8), 817-824, 2010.

[139] Triboulet R, Van K P and Didier G. "Cold travelling heater method", a novel technique of synthesis, purification and growth of CdTe and ZnTe. Journal of crystal growth, 101 (1-4), 216-220, 1990.

[140] Yang R, Jie W and Liu H. Growth of ZnTe single crystals from Te solution by vertical Bridgman method with ACRT. Journal of crystal growth, 400, 27-33, 2014.

[141] Asahi T and Sato K. Growth of large diameter ZnTe single crystals by the double crucible liquid encapsulated pulling method. physica status solidi (c), 11 (7‐8), 1167-1173, 2014.

[142] Asahi T, Yabe T and Sato K. Growth of large-diameter ZnTe single crystals by liquid-encapsulated melt growth methods. Journal of electronic materials, 33 (6), 651-653, 2004.

[143] Seki Y, Sato K and Oda O. Solution growth of ZnTe single crystals by the vertical Bridgman method using a hetero-seeding technique. Journal of crystal growth, 171 (1-2), 32-38, 1997.

[144] Kinoshita K, Arai Y, Inatomi Y, Tsukada T, Miyata H, Tanaka R, Abe K, Sumioka S, Kubo M and Baba S. SiGe Crystal Growth by the Traveling Liquidus-Zone Method aboard the International Space Station. Int. J. Microgravity Sci. Appl, 33 (2), 330213, 2016.

[145] Yu P and Jie W. Optical property analysis of high-resistivity CZT: In single crystals before and after annealing. Optical Materials, 36 (7), 1213-1218, 2014.

[146] Xu Y, He Y, Wang T, Guo R, Jie W, Sellin P J and Veale M. Investigation of Te inclusion induced glides and the corresponding dislocations in CdZnTe crystal. CrystEngComm, 14 (2), 417-420, 2012.

[147] Lordi V. Point defects in Cd (Zn) Te and TlBr: Theory. Journal of crystal growth, 379, 84-92, 2013.

[148] Sato K and Adachi S. Optical properties of ZnTe. Journal of applied physics, 73 (2), 926-931, 1993.